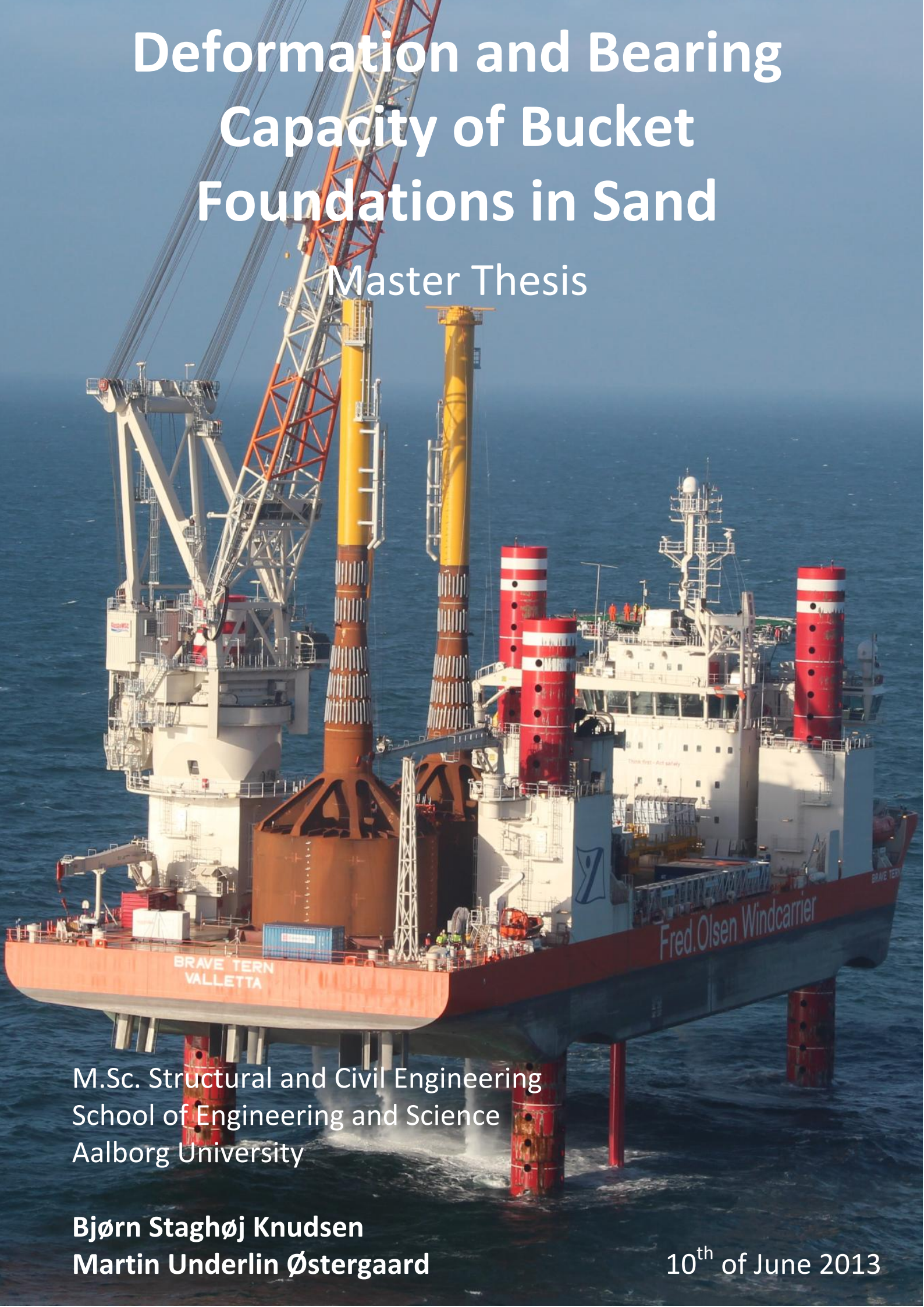


# Deformation and Bearing Capacity of Bucket Foundations in Sand

Master Thesis



M.Sc. Structural and Civil Engineering  
School of Engineering and Science  
Aalborg University

Bjørn Staghøj Knudsen  
Martin Underlin Østergaard

10<sup>th</sup> of June 2013



## Master Thesis

**Title:**

Deformation and Bearing Capacity of Bucket Foundations in Sand

**Written by:**

Bjørn Staghøj Knudsen  
Martin Underlin Østergaard

M.Sc. Structural and Civil Engineering  
School of Engineering and Science  
Aalborg University

**Supervisors:**

Professor Lars Bo Ibsen  
Associate Professor Johan Clausen

**Project Period:** 2012.09.01 - 2013.06.10 (Long Thesis)

**Completed:** 10<sup>th</sup> of June 2013

**Copies printed:** 5

**Number of pages:** 140

**Number of Appendices:** 10

---

Bjørn Staghøj Knudsen

---

Martin Underlin Østergaard

*The content of the report is freely available, but publication (with source reference) is only allowed with agreement by the authors.*

*The frontpage picture is from the test installation of two bucket foundations at Dogger Bank, 2013.*



## Regulation

This report is the Master Thesis for the M.Sc. in Structural and Civil Engineering at the School of Engineering and Science at Aalborg University. The thesis is a long thesis of 45 ECTS, and has been executed in the period from 1st of september 2012 to 10th of june 2013.

The project has involved laboratory work at the Geotechnical Laboratory at Aalborg University. In the connection with the laboratory work, the group would like to thank the technical staff, especially Jan Laursen, for valuable help regarding the set up. The tests have been executed in cooperation with Ph.D. fellow Søren Kjær Nielsen, whose help and guidance is appreciated.

## Reading instructions

References during the main report are collected in a bibliography in the back of the report. In the main report, the references are listed by the *Harvard Method* so a reference in the text appears as [Last name, Year] when used passively and as Last name [Year] when used actively in the text. If the reference contains more than two author, the reference is specified by the first last name and then 'et al.'. In the bibliography, books are specified by author, title, edition and possibly publisher. Websites are specified by author, title and the date when the website is downloaded.

References during the articles are collected in the same matter as the main report, however references used in the articles are only listed in the end of the relevant article.

Figures and tables are numbered according to the chapter in which they occur. Therefore, the first figure in chapter 7 has number 7.1, the second figure has number 7.2 and so on. Describing text for figures is placed beneath the figure, while describing text for the tables is placed above the given table. The figures and tables are made by the project group itself if the reference is not specified. Equations are specified by a number in a bracket and they are numbered like the figures and the tables. Therefore, the first equation in chapter 7 has number (7.1), the second equation has number (7.2) etc.



# Summary

---

The market for offshore wind turbines has been growing rapidly in the last decade, with over 1.2 GW of new effect installed in 2012 worldwide. There are many advantages to installing wind turbines offshore as opposed to onshore, however the total cost of offshore turbines per installed effect is still larger than onshore. Still the advantages regarding wind climate, visual impact, planning issues and noise are so important, that offshore development is being done on a large scale in especially Europe. Popularly said, most people like wind turbines if they obey the *not-in-my-backyard-concept*.

Due to the political demand for offshore wind farm development, great effort is put into trying to reduce the overall cost of the wind production in the whole lifetime. This has resulted in many suggestions to constructions, installation, operation, maintenance and decommissioning that can reduce the total expenses. One of the largest overall expenses is the foundation of the wind turbines, since the offshore environment causes a complex combination of loads from wind, wave, ice and operation.

The bucket foundation is a new foundation concept developed during the last decade at Aalborg University that is meant to greatly reduce the cost of the foundation during the whole lifetime. The bucket foundation is a cylindrical steel caisson, open in the bottom and closed at the top with a skirt length to diameter ratio between 0.5 and 1.0. The foundation is installed by applying suction inside the caisson, and can thus be installed using no heavy equipment. When installed, the foundation is a hybrid between a monopile and a gravitational foundation, utilizing both the weight of the soil in the caisson and the soil pressure on the outside of the skirt.

As the suction bucket concept is new, great effort is put into validation of the design process, with the goal of getting it approved by independent risk evaluation and classification organizations such as *Det Norske Veritas*. This master thesis is a part of the research work done involving the bucket foundation, and is in some parts a further development of work done previously at Aalborg University. The overall theme of this project is thus the bucket foundation concept.

An analytical tool used to determine the ultimate capacity of a cylindrical pile foundation is the  $p - y$  curves, which were developed using experiments done on very slender cylindrical piles with a length to diameter ratio of 34.4. These  $p - y$  curves have been used for monopile foundations as well, with a length to diameter ratio around 5, however this application is problematic, due to the large difference in slenderness, causing the behaviour of the foundation to be inconsistent with the original  $p - y$  experiments. The inconsistency is even greater with the bucket foundation, and can therefore not be applied.

The first part of this thesis uses 18 numerical finite element models of the bucket foundation in saturated sand in the drained condition with varying soil strength and geometry to calculate the soil response for a horizontal displacement needed to develop a new  $p - y$  formulation, which is valid for the bucket foundation. From the 18 models it has been possible to calibrate a generalized mathematical model, which allows for easy calculation of the soil response for a drained sand with a given angle of friction and geometry under a given horizontal displacement. The mathematical model is a first draft, and further work should be done to better validate and calibrate the model.

In the research work in geotechnics, experimental model testing is often used. To validate the experimental results it is often attempted to recreate the test results via

numerical modeling. With scaled models the stress level in the soil is however scaled accordingly as well. This is problematic, since the behaviour of the soil is not linear at small stress levels as predicted by the Mohr-Coulomb failure criterion. This causes the failure load obtained in a scaled experiment to be larger than predicted by the numerical modeling. This is naturally also a big challenge in relation to the research done with the bucket foundation.

The solution to this problem could be to use a material model that takes the stress-dependent behaviour of the soil into account. This is achieved by implementing a stress-dependent strength material model in PLAXIS 3D, which is a widely used commercial finite element code. After calibrating the material model to Aalborg University Sand No. 1, the material model exhibited correct behaviour and is able to predict results from triaxial at low confining pressures. When comparing the results from the material model to actual bucket foundation test results, it is obvious that the finite element model needs more work, although compared to the widely used Mohr-Coulomb model, the material model predicts a larger failure moment, just as expected.

One of the disputes of the bucket foundation design is the behaviour of the foundation when subjected to impulsive loads. These loads can occur offshore under a number of scenarios such as breaking waves, freak waves or emergency stops of the turbine. The approach today is to find the ultimate capacity in drained and undrained condition and then take the lowest value. For a dense sand, often encountered offshore, the drained capacity will in most cases be lower than the undrained. Previous research at Aalborg University has shown that the approach is very conservative, when dealing with impulsive loads, as the behaviour of the foundation for a high loading rate is close to fully undrained. As a forced displacement of a high velocity is applied, a significant pore pressure build up takes place inside and around the caisson, which greatly increases the capacity of the foundation.

The previous tests investigating the behaviour with different loading rates have been executed with equipment capable of applying a forced displacement at 10 mm/s with a range of 40 mm. Since then new equipment has been installed, making it possible to displace the bucket foundation with velocities up to 500 mm/s over a range of 500 mm. The third part of this thesis involves the first four successful tests with this new equipment. Great work has gone into installing and setting up the new equipment, which has led to a lot of good experience to be used in the further research.

5 The results from the four tests with 150 mm of forced displacement at rates from 0.1 mm/s to 100 mm/s showed the same trend as found in previous test. A strength increase from the slowest to the fastest test of more than 20 times was observed, while the build up of pore pressure reached values close to the cavitation limit of the setup at -290 kPa. The pore pressure distribution, which is a picture of the failure mechanism, showed negative pressure development at all measuring points, with the largest change inside the caisson.

# Summary in Danish (Sammendrag)

---

Markedet for offshore vindmøller har været i stor vækst det seneste årti med over 1.2 GW ny-installeret effekt i 2012 på verdensplan. At anvende havbaserede vindmøller giver mange fordele i forhold til landbaserede, dog er de totale omkostninger i levetiden for havvindmøller noget større pr. installeret effekt end tilsvarende møller på land. Fordelene ved offshore vindmøller, såsom højere basisvindhastighed, færre nabogener og lettere planlægning er dog så store, at udvikling af offshore vindmølleparker sker i meget høj grad i Europa. Populært sagt er de fleste mennesker positivt stillet overfor vindmøller, så længe de ikke står i deres egen baghave.

Den politiske efterspørgsel for offshore udvikling af vindmølleparker har medført en stor indsats for at formindske omkostningerne ved energiproduktion vindmøllernes fulde levetid. Udviklingen har medført mange nye koncepter til fremstilling, installation, drift, vedligeholdelse og nedtagning efter endt levetid, som kan reducere den totale pris. En af de største udgifter for offshore vindmøller er fundamentet, da klimaet offshore giver meget store laster fra vind, bølger, is og selve driften.

Bøttefundamentet er et nyt funderingskoncept, som er udviklet over det seneste årti på Aalborg Universitet, og som har til formål at nedbringe omkostningerne ved fundering gennem hele levetiden. Bøttefundamentet er en cylindrisk stålbeholder, der er åben i bunden og lukket i toppen og som har et længde-diameter forhold på omkring 0.5-1.0. Fundamentet installeres ved at påføre et undertryk inde i bøtten, mens den står på havbunden, hvorved fundamentet kan installeres uden brug af stort maskineri. Det installerede bøttefundament opfører sig som en hybrid mellem en monopæl og et gravitationsfundament, med udnyttelse af både vægten af den indkapslede jord og jordtrykkene på ydersiden af skørtet.

Eftersom konceptet med bøttefundamentet er nyt, bliver der brugt meget energi på at få valideret designproceduren med det overordnede mål at få den godkendt af uafhængige risiko- og klassificeringsvirksomheder såsom *Det Norske Veritas*. Dette afgangsprøveprojekt er en del af forskningsarbejdet med bøttefundamentet, og er på nogle punkter en videreførelse af tidligere udført forskning på området. Det overordnede tema for projektet er dermed bøttefundamentet som funderingskoncept.

$p - y$  kurver er et analytisk værktøj til at bestemme bæreevnen af en cylindrisk pæl i brudgrænsetilstanden, som blev udviklet ud fra eksperimenter med pæle med et slankhedsforhold på 34.4. Kurverne har været anvendt til monopæle, som har et slankhedsforhold på omkring 5. Dog er denne anvendelse problematisk, da dette er meget langt fra den oprindelige forsøgsgeometri, hvilket betyder at brudmekanismen for fundamentet er noget anderledes end de meget slanke pæle. Problematikken er endnu større for bøttefundamentet, hvorfor de originale  $p - y$  kurver ikke kan anvendes.

Den første del af projektet anvender 18 numeriske finite element modeller af bøttefundamentet i vandmættet sand i drænet tilstand med varierende jordparametre og geometri til at udregne jordens respons ved en horisontal flytning til at udvikle en ny  $p - y$  formulering, som er gyldig for bøttefundamentet. Ud fra de 18 modeller er det lykkedes at kalibrere en matematisk model, som gør det muligt at udregne jordens respons med en given friktionsvinkel, geometri og horisontal flytning. Den matematiske model er et første udkast og bør derfor finpudses og valideres med flere numeriske modeller med flere variationer over inputparametrene.

Indenfor det geotekniske forskningsområde bruges eksperimentelle modeller i høj grad.

For at validere modeltests forsøges det ofte at genskabe resultaterne vha. numerisk modellering. Ved brug af skalamodeller opnås meget lavere spændingsniveauer i jorden, hvilket er problematisk da jordens opførsel ikke skalerer lineært med spændingerne, som forudsagt af Mohr-Coulomb brudkriteriet. Dette betyder, at brudlasten ved et skalaforsøg ofte er meget forskellig fra den brudlast, der findes i numeriske modeller. Denne udfordring er naturligvis også tilstedeværende i forsøgsarbejdet med bøttefundamentet. Løsningen til dette problem kan være at benytte en materialemodel, der tager højde for jords spændingsafhængige opførsel. Dette kan opnås ved at implementere en materialemodel med spændingsafhængig styrke i PLAXIS 3D, som er en meget udbredt kommerciel finite element kode. Efter at have kalibreret materialemodellen til Aalborg Universitet Sand nr. 1, udviser materialemodellen korrekte egenskaber, og den er i stand til at forudsige resultater fra triaksial forsøg ved lavt kammertryk. Når materialemodellen sammenlignes med faktiske resultater fra skalerede bøtteforsøg, er det tydeligt, at finite element modellen skal forbedres, selvom materialemodellen sammenlignet med den traditionelle Mohr-Coulomb model giver et større brudmoment, ganske som forventet. Et af diskussionspunkterne omkring designmetoden af bøttefundamentet er responsen overfor impulsive laster. Denne lasttype kan opstå under en række forskellige scenarier såsom brydende bølger, freak waves eller nødstop af vindmøllen under brug. Fremgangsmåden i dag er at bestemme brudkapaciteten i sand for både drænet og udrænet tilstand, og så vælge den laveste af de to kapaciteter. For en tæt pakket sand, som oftest findes på offshore sandbanker, vil den drænedede kapacitet i de fleste tilfælde være lavere end den udrænedede. Tidligere forskning med bøttefundamentet har vist at denne tilgang er meget konservativ, når det omhandler impulsive laster, da responsen for høj lasthastighed har vist sig at være meget tæt på fuldstændigt udrænet. Ved en tvunget flytning påført med en høj hastighed har det vist sig, at der sker en signifikant opbygning af poretryk indeni og omkring bøttefundamentet, hvilket giver en stor forøgelse af bæreevnen af fundamentet.

De tidligere udførte forsøg med bøttefundamentet har været lavet med udstyr, der har kunnet påføre en flytning med en hastighed på maksimalt 10 mm/s med en slaglængde på 40 mm. Siden da er nyt udstyr blevet installeret, hvilket gør det muligt at påføre flytninger på op til 500 mm med en hastighed på 500 mm/s. Den tredje del af dette projekt indeholder resultaterne fra de første fire succesfulde forsøg med det nye udstyr. En stor arbejdsindsats har været lagt i at installere og tilpasse det nye udstyr, hvilket har givet mange brugbare erfaringer til det videre arbejde med forsøgsopstillingen.

Resultaterne fra de fire forsøg med 150 mm flytning påført med hastigheder fra 0.1 mm/s til 100 mm/s har udvist samme tendenser som de tidligere udførte forsøg. En forøgelse i brudkapaciteten på over 20 gange fandt sted fra den langsomste til den hurtigste test, mens poretryksopbygningen i den hurtigste test nåede værdier tæt på kavitationsgrænsen i tryktanken på ca. -290 kPa. Poretryksfordelingen, som giver et billede af brudmekanismen, viste negative udviklinger ved alle målepunkter med peakværdier fundet indeni bøttefundamentet.

# Table of Contents

---

Summary	vii
Summary in Danish (Sammendrag)	ix
<b>I Main Content</b>	<b>1</b>
<b>1 Introduction</b>	<b>3</b>
1.1 The Aim of the Thesis . . . . .	4
1.2 Structure of the Report . . . . .	6
<b>Article 1 - Determination of p-y Curves for Bucket Foundations in Sand Using Finite Element Modeling</b>	<b>6</b>
<b>Article 2 - Implementation of a Stress-dependent Strength Material Model in PLAXIS 3D</b>	<b>23</b>
<b>Article 3 - Small-scale Testing of Bucket Foundations in Sand</b>	<b>37</b>
<b>2 Conclusion</b>	<b>55</b>
<b>References</b>	<b>57</b>
<b>II Appendices</b>	<b>59</b>
<b>A Convergence and Test of Physical Domain in PLAXIS 3D</b>	<b>61</b>
<b>B Additional p-y Results</b>	<b>69</b>
<b>C Mathematical Formulation of the New p-y Curves</b>	<b>87</b>
<b>D Hardening Soil Small Strain material model</b>	<b>93</b>
<b>E Implementation of a UDSM in PLAXIS</b>	<b>101</b>
<b>F Source Code for UDSM</b>	<b>111</b>
<b>G Laboratory Details</b>	<b>117</b>
<b>H Step-wise Description of Laboratory Work</b>	<b>127</b>
<b>I Correction of Displacements</b>	<b>135</b>
<b>J Additional Laboratory Results</b>	<b>139</b>



## **Part I**

# **Main Content**



# 1 Introduction

---

The production from and demand for renewable energy sources has rapidly increased during the last few decades. Wind energy from wind turbines has been a large part of this development. As the number of installed wind turbines has increased, the trend has gone from primarily land based turbines to a large number of turbines being erected offshore. This is especially the case in Europe, where 90% of all new offshore capacity in 2012 was installed, cf. Global Wind Energy Council [2012]. Offshore wind turbines are however still only a small fraction of the total number of newly erected turbines as only 1293 MW of the total installed effect of 44711 MW installed in 2012 was offshore turbines.

As the demand for installed wind effect increases, the average size of the wind turbines increase as well. The average installed wind turbine offshore is approximately 4.0 MW, with the Siemens 3.6 MW turbine, as seen in figure 1.1, being the most used model. The larger wind turbines causes the stress on the whole structure and especially the foundations to be greater and greater, making it an important area of research.



*Figure 1.1.* The Siemens 3.6 MW wind turbine used at Horns Rev 2 in Denmark. [DONG Energy, 2009]

Installing wind turbines offshore has many obvious advantages, such as higher mean wind velocity, fewer noise problems under operation and less visual impact. For many countries the environmental impact on the surroundings of a wind turbine park has made offshore wind energy the preferred choice as the space onshore is scarce. There are however some challenges as well and these are mainly related to a more harsh climate

causing the construction cost to be significantly higher. One of the large costs involved is the foundation of the turbine, which has therefore been subject to a lot of effort trying to reduce the overall expenses. The suction bucket foundation is one of the proposed concepts meant to decrease both the production, installation and decommission cost of the foundation.



*Figure 1.2.* Installed bucket foundation at Frederikshavn Havn. [Larsen, 2008]

The suction bucket differs from the name wise similar suction caisson used together with jacket structures for oil platforms, as the suction caisson are often used in groups of four, creating a static system that ensure only vertical loads. The suction bucket concept is with only one large caisson, and will therefore be subjected to both vertical, horizontal and moment loading. The concept is still being developed, however it has been proven to work at a number of test installations. One of these is the 3 MW Vestas turbine installed at Frederikshavn Havn in 2002, cf. figure 1.2. The bucket foundation has the capability of being installed at everything from near shore to 40 meters depth, making it feasible for 80-90 % of all offshore parks planned in Europe. It has the potential to decrease the total used steel weight with up to 50 %, making the production a lot cheaper as the steel cost is a big part of the total cost. The installation of the bucket foundation is easier, and does not require large equipment as the foundation is installed by applying suction inside the caisson, which drives the foundation into the seabed. Furthermore the foundation can be decommissioned by reversing the installation procedure allowing for reuse of the steel. [Ibsen et al., 2008]

The main challenges in the further development of the bucket foundation is to validate the design process and convince the certification agencies of the properties of the foundation. This master thesis is a contribution to this work.

## **1.1 The Aim of the Thesis**

This thesis consists of three scientific papers of three different subjects regarding the research of the bucket foundations. The three subjects will be explained in the following.

### **1.1.1 Development of $p - y$ Curves for the Bucket Foundation**

The technology used to build offshore structures originates in the oil industry, where platforms have been used since the early 1900s. The expertise gathered from the oil industry has been extrapolated to the offshore wind sector, since this was the best knowledge available. An example of this is the  $p - y$  formulations that are used for embedded offshore piles. The  $p - y$  curves is an expression of the relationship between soil reaction and displacement of cylindrical piles. Today, as recommended in Det Norske Veritas [2007], the  $p - y$  curves can be used to determine the lateral ultimate limit state capacity. The development of the  $p - y$  relationships were done using very slender cylindrical piles with a length to diameter ratio of approximate 34. The bucket foundation typically has a length to diameter ratio between 0.5-1.0 and is thus expected to behave significantly different than a slender pile [Brødbæk et al., 2009]. The first article in this thesis aims at developing a new  $p - y$  relationship for the bucket foundation using numerical finite element calculation in PLAXIS 3D with an advanced material model for the soil. The investigations are done with sand in the drained condition, but development to other soil types and drainage conditions should be further examined.

### **1.1.2 Implementation of a User Defined Soil Model in PLAXIS 3D**

Within geotechnical research, a lot of scaled model tests are used, since full scale testing is very expensive and complicated to carry out. In order to validate the experimental work, numerical models can be used to recreate the results through finite element modeling. This is however often not possible, as the commercially implemented soil models are designed and developed for full scale models with a certain stress level in the soil. This is a problem, since sand has shown to exhibit higher strengths at low stress levels, which are present in the scaled models, cf. Krabbenhøft et al. [2011]. The strength increase which is unaccounted for in the typical soil models such as the Mohr-Coulomb and the Hardening Soil models causes the capacity of the scaled models in the numerical calculations to be greatly underestimated.

The second article is an implementation of a user defined soil model, which can take into account the relative strength increase at low stress levels by using a curved version of the Mohr-Coulomb failure criterion. The parameters of the failure criterion are calibrated using a number of triaxial tests done at back pressure levels from 5 kPa to 800 kPa. The soil model is implemented in PLAXIS 3D through the FORTRAN code language, and is then tested against existing test results with the scaled bucket foundation.

### **1.1.3 Small-scale Tests of a Bucket Foundation Subjected to Transient Loading**

In the certification of the bucket foundation, one of the points of discussion has been the capacity during transient loading of varying loading rate. During the loading of the foundation in a dense saturated sand a pore pressure build up will occur if it cannot dissipate fast enough. The distribution and magnitude of the pore pressure build up is a question of discussion, and has been a subject of research during the last couple of years at Aalborg University, cf. Sjelmo et al. [2012] and Foglia et al. [2013]. It has been shown that the capacity of the foundation is highly dependent of the loading rate,

but until now the test setup has not been able to handle sufficiently large deformations, velocities and forces.

A new test setup has been installed since the last tests were executed, and the last part of this thesis covers the very first test done with this setup. In the tests a scaled bucket foundation with a 500 mm diameter and 250 mm skirt length is subjected to loading rates from 0.1 mm/s to 100 mm/s with a range of 150 mm. The last article in the thesis deals with the new test setup, the execution of the tests and the results from the first four successful tests.

## **1.2 Structure of the Report**

The main textual content of the report is the three articles that directly follows this introductory chapter,

1. Determination of p-y Curves for Bucket Foundations in Sand Using Finite Element Modeling
2. Implementation of a Stress-dependent Strength Material Model in PLAXIS 3D
3. Small-scale Testing of Bucket Foundations in Sand

After the articles the main conclusion of the project follows. In the end a number of appendices are appended, where additional explanations, results and derivations are shown.

# Determination of p-y Curves for Bucket Foundations in Sand Using Finite Element Modeling

Bjørn Staghøj Knudsen  
Martin Underlin Østergaard  
Lars Bo Ibsen  
Johan Clausen





Aalborg University  
Department of Civil Engineering

**DCE Technical Memorandum No. 31**

# **Determination of p-y Curves for Bucket Foundations in Sand Using Finite Element Modeling**

by

Bjørn Staghøj Knudsen  
Martin Underlin Østergaard  
Lars Bo Ibsen  
Johan Clausen

June 2013

© Aalborg University

## Scientific Publications at the Department of Civil Engineering

**Technical Reports** are published for timely dissemination of research results and scientific work carried out at the Department of Civil Engineering (DCE) at Aalborg University. This medium allows publication of more detailed explanations and results than typically allowed in scientific journals.

**Technical Memoranda** are produced to enable the preliminary dissemination of scientific work by the personnel of the DCE where such release is deemed to be appropriate. Documents of this kind may be incomplete or temporary versions of papers—or part of continuing work. This should be kept in mind when references are given to publications of this kind.

**Contract Reports** are produced to report scientific work carried out under contract. Publications of this kind contain confidential matter and are reserved for the sponsors and the DCE. Therefore, Contract Reports are generally not available for public circulation.

**Lecture Notes** contain material produced by the lecturers at the DCE for educational purposes. This may be scientific notes, lecture books, example problems or manuals for laboratory work, or computer programs developed at the DCE.

**Theses** are monographs or collections of papers published to report the scientific work carried out at the DCE to obtain a degree as either PhD or Doctor of Technology. The thesis is publicly available after the defence of the degree.

**Latest News** is published to enable rapid communication of information about scientific work carried out at the DCE. This includes the status of research projects, developments in the laboratories, information about collaborative work and recent research results.

Published 2013 by  
Aalborg University  
Department of Civil Engineering  
Sohngaardsholmsvej 57,  
DK-9000 Aalborg, Denmark

Printed in Aalborg at Aalborg University

ISSN 1901-7278  
DCE Technical Memorandum No. 31

# Determination of $p$ - $y$ Curves for Bucket Foundations in Sand Using Finite Element Modeling

Bjørn S. Knudsen<sup>1</sup> Martin U. Østergaard<sup>1</sup> Lars Bo Ibsen<sup>2</sup> Johan Clausen<sup>3</sup>

*Department of Civil Engineering, Aalborg University*

## Abstract

Cylindrical offshore wind turbine foundations, such as bucket foundations and monopiles, have up till now been designed using analytical methods based on experiments done with piles much more slender than the ones used in today's industry. Compared to the widely used monopile foundation, the suction bucket has a much smaller ratio between length and diameter, and the suction buckets will thus act more as a rigid object during rotation in the soil. To improve the design of suction buckets through analytical methods, the soil pressure needs to be calculated more precisely since currently available  $p - y$  curves, linking displacement and soil pressure, are based on more slender cylindrical structures. Using finite element methods, the  $p - y$  curves for suction buckets will be determined as a function of the internal angle of friction of the soil, the diameter and the skirt length of the suction buckets, which can in turn be applied in determination of soil pressures for analytical design methods of suction bucket foundations.

## 1 Introduction

The aim of this study is to determine the soil pressure response  $p$  in drained sand as a function of a displacement  $y$  for a set of bucket foundations with different diameter  $D$  and skirt length  $L$  embedded in soils of varying strength determined by the internal angle of friction  $\varphi$ . The  $p - y$  curves are found by using finite element modeling in PLAXIS 3D. PLAXIS 3D is used mainly within the fields of geotechnics since it has several advanced soil material models incorporated, e.g. the Hardening Soil Small Strain model that will be used in this investigation. The method used to obtain the soil response  $p$  and the displacement  $y$  is explained in the following.

1. A prescribed uniform horizontal displacement is applied to all parts of the bucket foundation. The soil reaction pressure  $p$  builds during this step, and  $p$  is extracted from PLAXIS 3D.
2. The horizontal displacement is removed from the bucket foundation so that only irreversible (i.e. plastic) deformations remain. This plastic deformation  $y$  is extracted from PLAXIS 3D.
3. This procedure is repeated for an increasing lateral displacement.
4. To increase usability of the results outside the finite element method,  $p$  and  $y$  are normalized to elimi-

nate variation in depth and a function is fitted to allow for a fast computation of the soil reaction pressure  $p$  for varying bucket diameter, skirt length and soil strength (through the internal angle of friction  $\varphi$ ).

## 2 Theory

Traditionally, soil response has been treated as a 2D-problem, described thoroughly for plane strain problems, e.g. sheet pile walls. With the introduction of monopiles as a solution to offshore foundation of e.g. wind turbines, the soil response of such cylindrical structures has increased the demands for knowledge within the field of 3D soil interaction. For a bucket foundation however, the existing knowledge regarding  $p - y$  response curves for slender structures in 3D cannot be employed since buckets behave nearly rigid, cf. figure 1. Thus, the geometry has to be taken into account. The traditional 2D-theory provides a good offset for the understanding of displacement and soil response. Figure 2 shows how the active and passive earth pressure develop.

It can be seen that to mobilise the full passive soil pressure requires a larger displacement than to mobilise the full active pressure. The illustrated principle is valid for 2D but the same principle applies for 3D. To examine the 3D-effect, the soil pressure found in the numerical calculation will be compared to the 2D-soil pressure found by Rankine's soil pressure theory. By doing so, any added soil pressure obtained for a given displacement in a given soil compared to the 2D-case will be caused by this 3D-effect. Since the Rankine pressure is easily calculated, the results in the following

<sup>1</sup>M.Sc. Student, Department of Civil Engineering, Aalborg University, Denmark

<sup>2</sup>Professor, Department of Civil Engineering, Aalborg University, Denmark

<sup>3</sup>Associate Professor, Department of Civil Engineering, Aalborg University, Denmark

will mainly focus on determining the factor that the 3D-soil pressure is larger than the corresponding 2D-soil pressure.

### 3 Material Model

The applied material model in the finite element code is the Hardening Soil Small Strain material model (HSsmall). HSsmall includes the stress-dependent behaviour of the Hardening Soil Material Model (HS) where the current stress state is taken into account when calculating the stiffness, but HSsmall has a more realistic behaviour towards small strains. The HSsmall model is more demanding calculationwise, however the extra calculation time is well spend, as the results are closer to real-life behaviour. Additional stiffness at very small strains has long been known to occur in the field of soil dynamics, but has only recently been implemented in static calculations (Ovesen et al., 2009). By not using the HSsmall model there is a significant risk of overestimating the deformations in the soil and thus underestimating the stresses. Since the objective of this article is to find a link between the displacement  $y$  and the resultant soil pressure  $p$ , the HSsmall model is highly relevant. As the name implies the HSsmall model incorporates hardening in the soil, causing the stiffness parameters to change as a function of the current stress state. This is done by using a power law to describe the development of the moduli of elasticities and the shear moduli. The power laws for the different stiffness moduli follow the same form, e.g. the development of  $E_{50}$  is given by,

$$E_{50} = E_{50}^{ref} \left( \frac{\sigma_3 + c \cot(\varphi)}{\sigma_{ref} + c \cot(\varphi)} \right)^m. \quad (1)$$

The model incorporates a multi-surface yield criterion with isotropic hardening. The shape of the yield criterion is similar to that of the Mohr-Coulomb hexagonal cone, however the surface is bound by a cap in the direction of the hydrostatic stress axis. A sketch of the yield

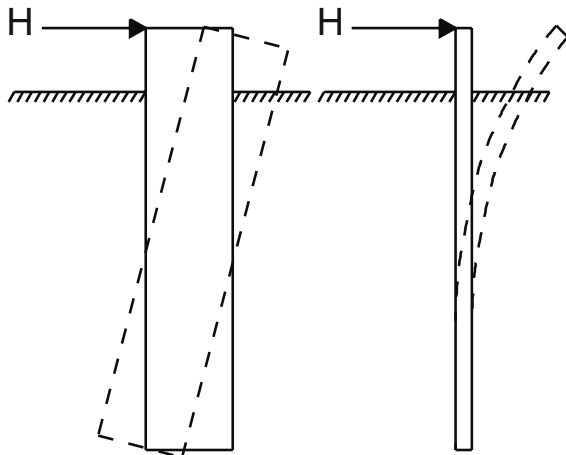


Figure 1: The difference between the behaviour of slender and non-slender piles when subjected to horizontal load. The non-slender pile rotates as a rigid body. (Brødbæk et al., 2009)

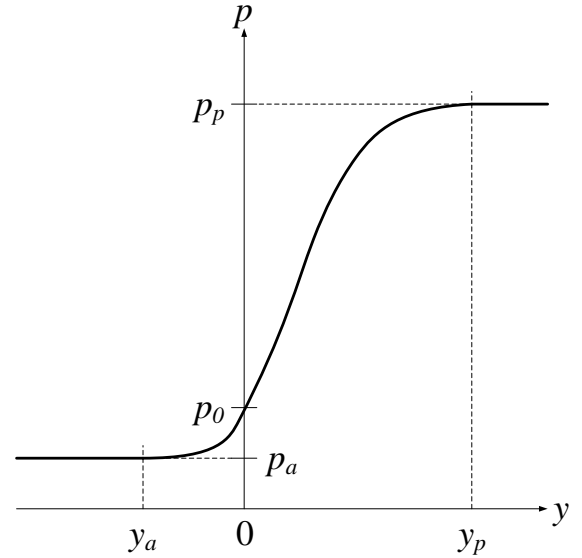


Figure 2: The relation between the displacement away from the soil  $\delta_a$  and the active pressure  $p_a$  and the displacement towards the soil  $\delta_p$  and the passive soil pressure  $p_p$ . The soil pressure at rest is  $p_0$ . (Ovesen et al., 2009)

surface in the principal stress space is shown in figure 3. Compression is positive, tension is negative.

### 4 Determination of Soil Strength and Stiffness Parameters

The internal angle of friction  $\varphi$  is commonly used as a design parameter for sands since it is used in Mohr-Coulomb yield criterion and also resembles a physical property of the material. Therefore,  $\varphi$  is also the main parameter in this study, and all other strength and stiffness parameters of the sand are linked to  $\varphi$ . The used relations in the following are taken from Det Norske Veritas (1992), Jensen et al. (2009) and Brinkgreve et al.

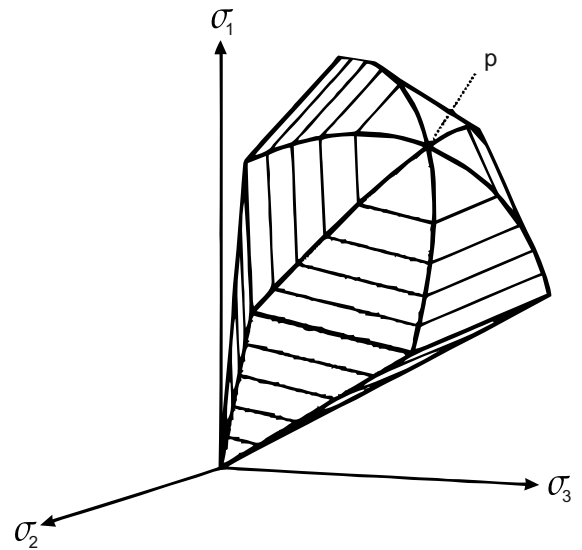


Figure 3: The yield surface of the HSsmall model. (Brinkgreve et al., 2012)

(2012) and the sand is assumed to be of the type *Fredrikshavn Sand* which characteristics are typical for an offshore sand. The relative density  $I_D$  is an important parameter since it indicates how much the soil is compacted. The terms 'loose', 'medium' or 'dense' referring to the degree of compaction, is often used in empirical formulas in geotechnical engineering.  $I_D$  is linked to  $\varphi$  through,

$$\varphi = \varphi'_{\text{crit}} + 3^\circ I_R - 3^\circ I_D - \Delta\varphi_1, \quad (2)$$

where the critical internal of friction  $\varphi'_{\text{crit}} = 33^\circ$ ,  $\Delta\varphi_1 = 2^\circ$  for 5-10 % content of silt and  $I_R$  is calculated from,

$$I_R = I_D \left( Q_{\text{min}} - \ln \frac{p'}{1 \text{ kPa}} \right), \quad (3)$$

where the representative mean normal stress is  $p' = 100$  kPa and  $Q_{\text{min}} = 10$  for quartz sand.  $I_R$  and  $Q_{\text{min}}$  are both dependent on mineralogy of the grain material. Poissons ratio  $\nu$  is linked to  $\varphi$  through,

$$\nu = \frac{1 - \sin \varphi}{2 - \sin \varphi}. \quad (4)$$

The elastic modulus  $E_{50}$  is determined from,

$$E_{50} = \frac{1 - \nu - 2\nu^2}{1 - \nu} E_{\text{oed}}, \quad (5)$$

with  $E_{\text{oed}}$  found by,

$$E_{\text{oed}} = m \sqrt{\sigma' \sigma_a}, \quad (6)$$

where  $m$  as a function of  $I_D$  is shown in figure 4. The values here are used commonly for Norwegian inorganic sands, which are assumed similar to Frederikshavn Sand. In equation (6), the atmospheric pressure is  $\sigma_a = 100$  kPa and the reference pressure  $\sigma' = 100$  kPa. This is used along with figure 4 to compute  $E_{\text{oed}}$ . For computing the unloading and reloading response, the unloading/reloading elastic modulus  $E_{\text{ur}}$  is calculated from,

$$E_{\text{ur}} = 3E_{50}. \quad (7)$$

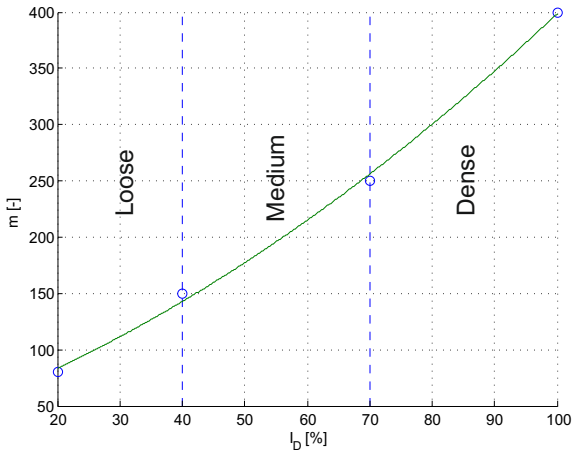


Figure 4: Approximation of  $m$  as a function of  $I_D$ . (Det Norske Veritas, 1992)

Table 1: Strength and stiffness parameters for sand used in the numerical model.

$\varphi$	[ $^\circ$ ]	30	35	40
$\psi$	[ $^\circ$ ]	0	5	10
$Q_{\text{min}}$	[-]	10.00	10.00	10.00
$\Delta\varphi_1$	[ $^\circ$ ]	2.00	2.00	2.00
$I_D$	[%]	15.17	53.09	91.02
$\nu$	[-]	0.33	0.30	0.26
$E_{50}$	[MPa]	4.92	14.06	28.54
$E_{\text{oed}}$	[MPa]	7.39	18.87	35.15
$E_{\text{ur}}$	[MPa]	14.77	42.17	85.62
$e$	[-]	0.99	0.83	0.68
$G_0$	[MPa]	65.23	82.30	103.49
$\gamma_{0.7}$	[mm/m]	0.22	0.18	0.14
$K_0$	[-]	0.50	0.43	0.36
$c'$	[kPa]	0.10	0.10	0.10

In HSsmall extra parameters compared to HS need to be determined to model the stress dependency of the shear stiffness and the shear modulus dependency of the strain. The initial shear modulus  $G_0$  is determined from equation (8) and the reference shear strain from equation (9).

$$G_0 = \frac{33(2.97 - e)^2}{1 + e}, \quad (8)$$

$$\gamma_{0.7} = \frac{2c'(1 + \cos(2\varphi')) - \sigma'_1(1 + K_0)\sin(2\varphi')}{9G_0}, \quad (9)$$

where the effective cohesion  $c' = 0.1$  kPa and the coefficient for soil pressure at rest  $K_0 = 1 - \sin(\varphi)$ . The effective cohesion in the soil is set to 0.1 kPa to ensure numerical stability as recommended in Brinkgreve et al. (2012).  $e_{\text{min}} = 0.64$  and  $e_{\text{max}} = 1.05$  are used for the Frederikshavn Sand to determine  $e$  through,

$$I_D = \frac{e_{\text{max}} - e}{e_{\text{max}} - e_{\text{min}}}. \quad (10)$$

Table 1 contains the material parameters used in the numerical modeling in PLAXIS 3D.

## 5 Modeling in PLAXIS 3D

The finite element tool used to compute  $p - y$  curves for the bucket foundation is PLAXIS 3D. The bucket is built using different geometries to determine the influence of the diameter  $D$  and the skirt length  $L$  on the  $p - y$  response. The third changeable parameter is the internal angle of friction  $\varphi$ . Table 2 shows the models that are tested in PLAXIS 3D. The bucket itself is constructed of steel plate elements. The steel material is chosen thicker than steel ordinarily used for bucket foundations to increase the bending stiffness and to avoid any deformation in the steel structure itself. This is done since the main interest of this investigation is the soil response. To further avoid any bending in the bucket steel structure,

the displacement is applied to all parts of the bucket producing a lateral displacement of the entire bucket instead of the more realistic rotational behaviour. This does not influence the results, since only the lateral soil response is of interest.

### 5.1 Boundaries, Convergence and Meshing

The boundaries of the model domain are chosen so that the failure mechanism has enough room to develop fully without being influenced by the edges of the model. The size of the model domain is seen in figure 6. Along the bottom of the skirt, stress concentrations will arise due to the abrupt change in geometry. To even this concentration out and reduce the effect of it, an extended interface is introduced as recommended in Brinkgreve et al. (2012). The interface is extended both vertically and horizontally. The length of the extension is  $L_{ext} = 0.2D$  based on Vaitkunaite (2012). To ensure the results close to the bucket, where the strain and stress gradients are

Table 2: Overview of the tested models.

Model no.	$D$ [m]	$L$ [m]	$\varphi$ [°]
1	10	5	30
2	10	5	35
3	10	5	40
4	10	10	30
5	10	10	35
6	10	10	40
7	15	7.5	30
8	15	7.5	35
9	15	7.5	40
10	15	15	30
11	15	15	35
12	15	15	40
13	20	10	30
14	20	10	35
15	20	10	40
16	20	20	30
17	20	20	35
18	20	20	40

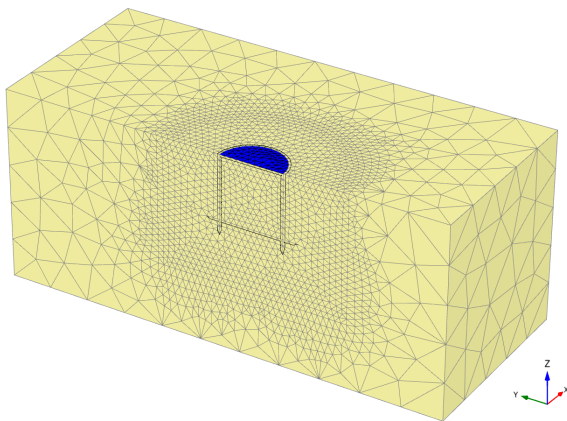


Figure 5: An example of the mesh of the FE model.

Table 3: Phases in the models.

Phase	Name	Action(s)
0	Initial	$K_0$ -procedure, soil activated
1	Installation	Plates, interfaces activated
2	Nil-step	Equilibrium reestablished
3,5,7...	Load	Displacement activated
4,6,8...	Unload	Displacement deactivated

large, are modeled with a sufficient accuracy, the mesh is refined in a volume close to the bucket itself. The size of this refined volume is shown in figure 6. The meshing facility in PLAXIS 3D allows for a relative meshing size to be chosen. Firstly the overall mesh density is selected, after which a linear mesh refinement factor is applied to the volume containing the bucket. A convergence analysis has been carried out, to ensure a sufficient mesh quality. An example of the mesh can be seen in figure 5.

### 5.2 Phases in the Calculation

The model has five basic phases. The first two being the initial phase (phase 0) and installation phase (phase 1). In the nil-step phase, equilibrium is reestablished after the installation of the bucket and all deformations are reset because only the displacement from phase 3 and onwards is of interest. Phase 3 is a loading phase where the prescribed displacement is applied to all parts of the structure. Phase 4 is an unloading phase where the prescribed displacement is removed. Because of the elastoplastic behaviour of the soil, the elastic deformations from phase 3 will be rolled back and only the plastic part of the deformation will remain. This pattern, plastic loading followed by elastic unloading, is continued for an increasingly large deformation until the soil body collapses or the maximum applied displacement has been reached.

### 5.3 Integration of Stresses

In order to determine the soil reaction pressure, the stresses on the bucket skirt are examined. From PLAXIS 3D it is possible to extract stresses in the soil, the plate elements of the bucket and the interface between soil and bucket. From Hansen et al. (2012) the method with extraction of stresses from the interface provided more reliable results and this method will be used in the following. In short, the method uses the normal  $\sigma'_N$  stress and the shear stresses  $\tau_1$  and  $\tau_2$  from the interfaces to compute a total soil pressure on the surface of the structure bucket foundation skirt as,

$$F_y = \int_A (\sigma'_N \sin \theta + \tau_1 \cos \theta) dA. \quad (11)$$

The shear stress  $\tau_1$  acts along the circumference and  $\tau_2$  acts vertically along the skirt of the bucket. For determining the soil reaction pressure  $p$ ,  $\tau_2$  is disregarded. The pressures acting on the bucket skirt during the horizontal displacement are shown in figure 7.

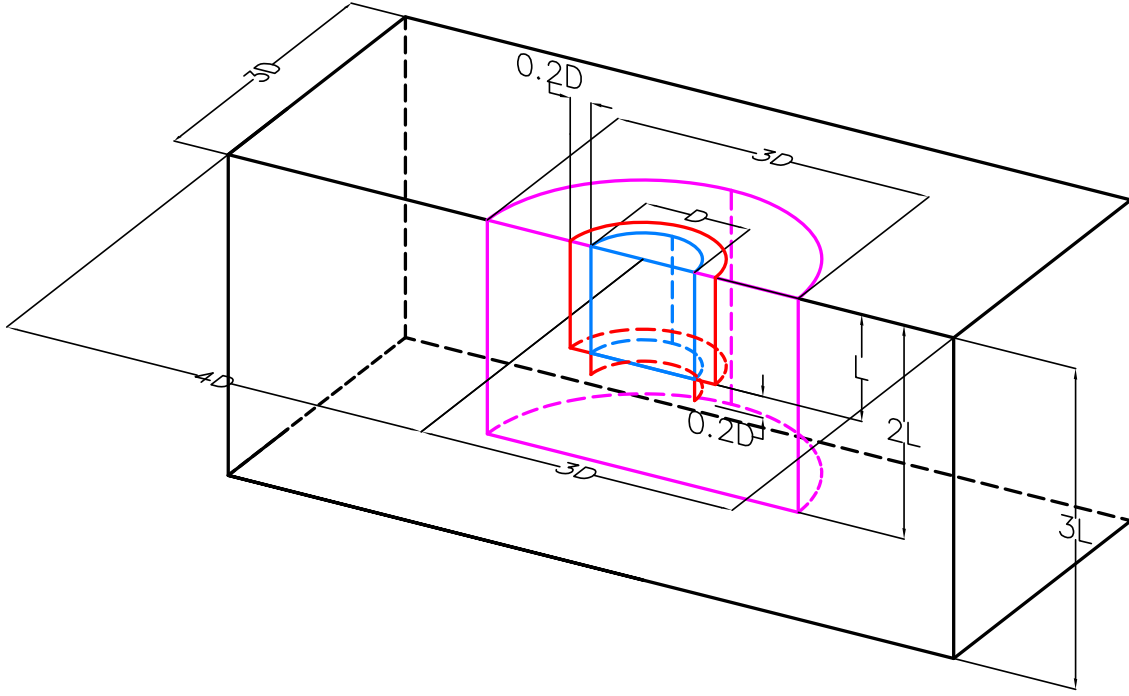


Figure 6: Size of model domain shown with black lines. The bucket itself is shown with blue lines, the volume with refined mesh is shown with pink lines and the extended interfaces are shown with red lines.

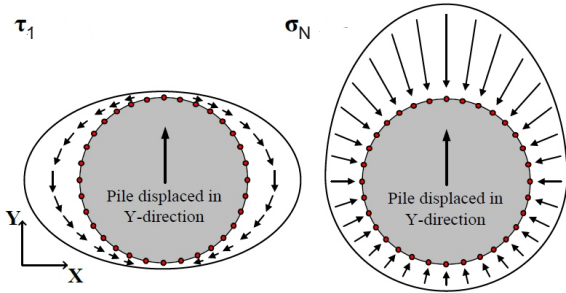


Figure 7: Principal sketch of the normal stress  $\sigma_N$  and the shear stress  $\tau_1$  when the bucket foundation is displaced horizontally (de Place, 2012).

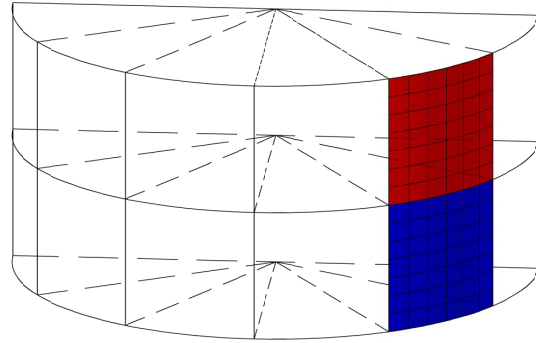


Figure 8: Areas for integration of surface stresses.

The bucket is divided into layers with the depth and each layer is divided into slices as seen in figure 8 where two areas, the blue and the red, have been highlighted as an example. In each of these areas, the average stress is found which is multiplied by the specific area to get the force acting on the specific area. The resulting soil reaction  $p$  for a given layer is then found as the sum of the average forces of all areas in this layer divided by the height of the layer.

## 6 Results

The results from the models shown in table 2 will be visualized through the following procedure.

1. Raw results from the model are plotted in a  $p-y$  diagram.

2. The soil pressure  $p$  is normalized by the Rankine pressure  $p_R$ . The displacement  $y$  is normalized by the bucket diameter  $D$ .
3. The results are trimmed so edge effects in the skirt top and bottom are removed.
4. A tanh-function is fitted to the data.

### 6.1 Plotting of $p-y$ Curves

The  $p-y$  data extracted from model 9 is plotted in figure 9. There is a  $p-y$  curve for each of the depth layers. The  $z$ -value in the legend is taken as the depth of the middle of each layer. The pressure increases with depth as expected. To better visualize the results, the depth parameter  $z$  is sought to be eliminated through normalization.

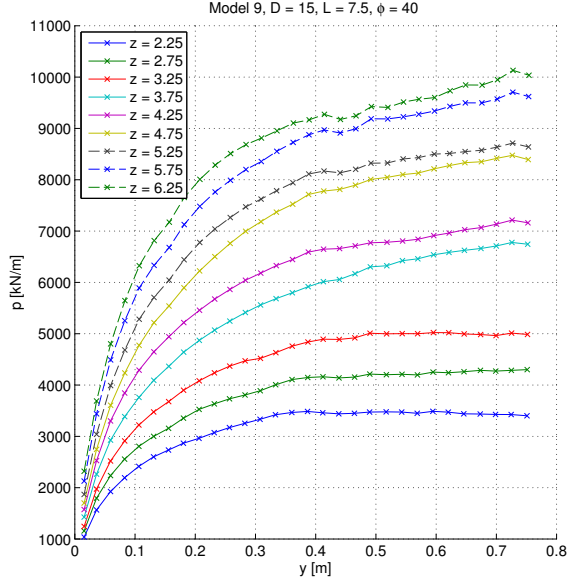


Figure 9: Step 1 - Raw results from the model are plotted in a  $p - y$  diagram. This data have already been trimmed, cf. section 6.3.

## 6.2 Normalization of Soil Pressure

To eliminate the depth dependency of the  $p - y$  curves, the soil pressure  $p$  is normalized by the Rankine pressure  $p_R$  which is a linear function of the depth  $z$ . The displacement  $y$  is normalized by the bucket diameter  $D$ . The Rankine pressure is calculated as,

$$\begin{aligned} p_R &= \gamma' z D (K_\gamma^p - K_\gamma^a) \\ &= \gamma' z D \left( \frac{1 + \sin(\varphi)}{1 - \sin(\varphi)} - \frac{1 - \sin(\varphi)}{1 + \sin(\varphi)} \right), \end{aligned} \quad (12)$$

where  $\gamma'$  is the specific soil weight,  $z$  is the depth and  $\varphi$  is the internal angle of friction of the soil. By normalizing the pressure  $p$  by the Rankine pressure that is a linear function of the depth  $z$ , the  $p - y$  curves for each depth layer will turn into one curve, if the pressure  $p$  is also a linear function of  $z$ .

## 6.3 Trimming and Fitting of Data

It is evident from investigating the data, that the normalization by the Rankine pressure is not suitable in the top and the bottom of the bucket. These variations are considered to be edge effects and are disregarded. After the data has been trimmed, the results are fitted with a function of the type,

$$\begin{aligned} \frac{p}{p_R} &= \beta_1 \tanh\left(\beta_2 \frac{y}{D}\right) \\ &+ \beta_3 \tanh\left(\beta_4 \frac{y}{D}\right) + \frac{K_0}{K_\gamma^p - K_\gamma^a}, \end{aligned} \quad (13)$$

where  $\beta_2$  and  $\beta_4$  are shape coefficients of the fitting function that controls the climb rate of the function in the initial part and towards the ultimate soil pressure. From

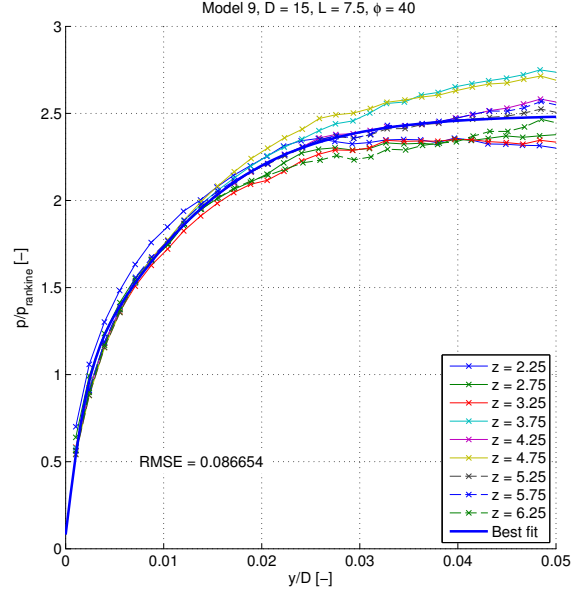


Figure 10: Step 3 and 4 - The results are trimmed so edge effects in the skirt top and bottom are removed. The best fit is shown.

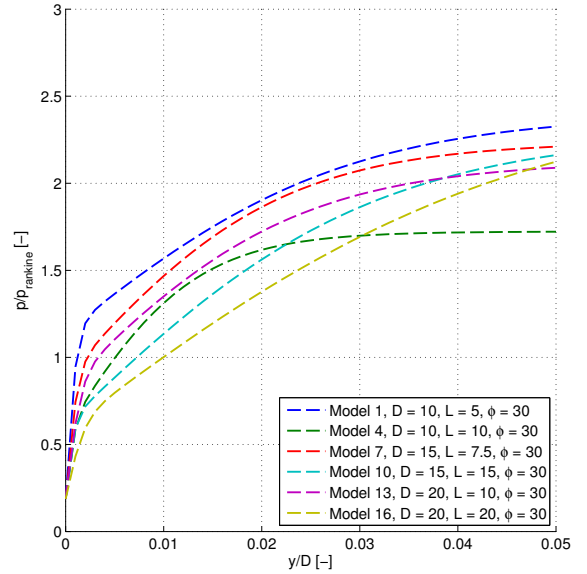


Figure 11: Best fit for models with  $\varphi = 30^\circ$ .

equation (13) it is evident that,

$$\frac{p}{p_R} \rightarrow \beta_1 + \beta_3 + \frac{K_0}{K_\gamma^p - K_\gamma^a} \text{ for } \frac{y}{D} \rightarrow \infty, \quad (14)$$

meaning that  $\beta_1$  and  $\beta_3$  control the maximum relative soil pressure. The fitting function consists of three terms, the first two enabling the fitting function to fit both the initial and end slope, while the third term involving  $K_0$  takes into account the soil pressure at rest at  $y = 0$ . The trimmed data with the fitted function is shown in figure 10. This procedure is done for all 18 models, and the fitted functions are gathered - one diagram for  $\varphi = 30^\circ$ ,  $\varphi = 35^\circ$  and  $\varphi = 40^\circ$ . These results are shown in figures 11, 12 and 13. From this initial study of the  $p - y$  curves and the best fit, it seems like models with  $L/D = 0.5$  have

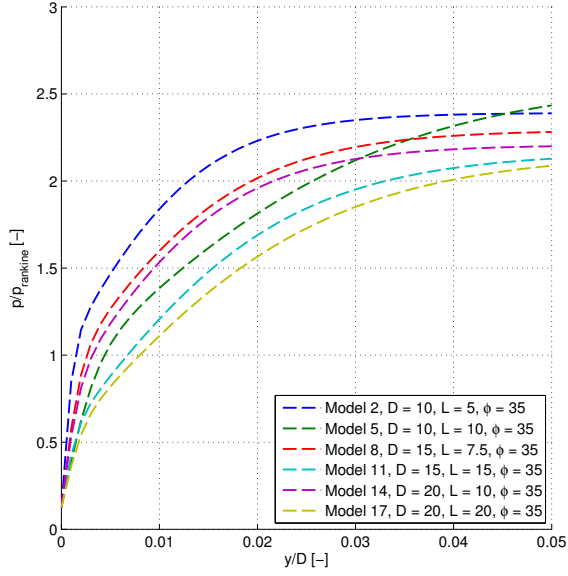


Figure 12: Best fit for models with  $\varphi = 35^\circ$ .

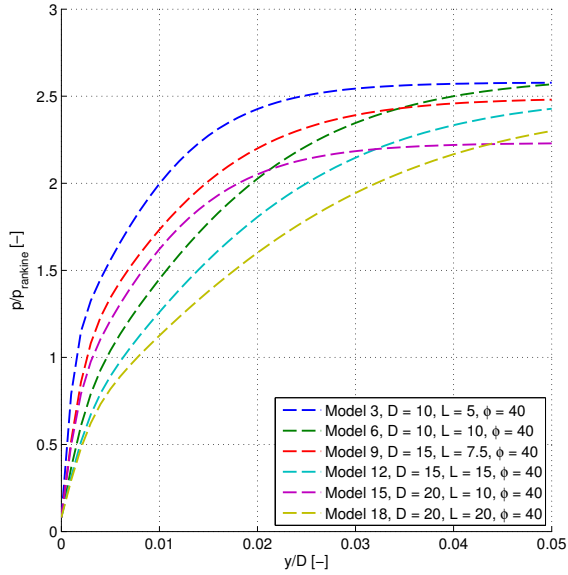


Figure 13: Best fit for models with  $\varphi = 40^\circ$ .

a bigger initial stiffness than models with  $L/D = 1$ . This is evident for all values of  $\varphi$ . Figures 11, 12 and 13 show the best fit, meaning that the parameters  $\beta_1$ ,  $\beta_2$ ,  $\beta_3$  and  $\beta_4$  are free to attain an arbitrary value. In the following, these parameters are sought to be described as a function of the three basic parameters,  $D$ ,  $L$  and  $\varphi$ .

## 7 Mathematical Model

In order to put the results from the numerical examination into real-life application, a mathematical model, that can be used to evaluate the soil response of an arbitrary bucket geometry and soil strength, is sought. The method for obtaining this mathematical expression is to examine the dependency of the parameters  $\beta_1$  to  $\beta_4$  of the geometrical parameters  $D$  and  $L$  and the soil strength

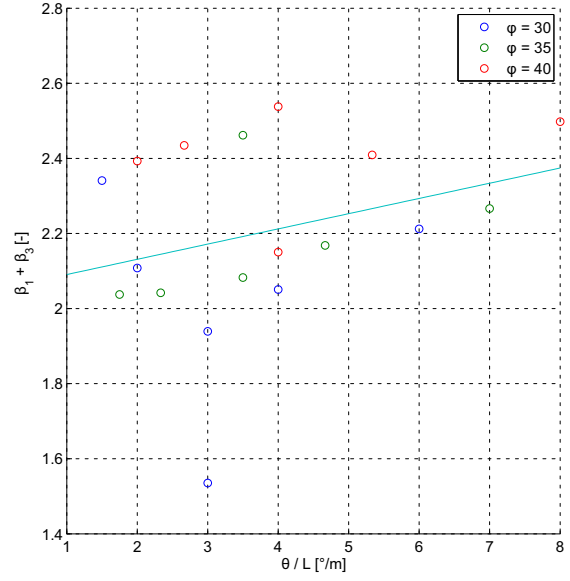


Figure 14: Examination of  $\beta_1 + \beta_3$  as a function of  $\frac{\varphi}{L}$ .

Table 4: Coefficients in the fit of  $\beta_1$  and  $\beta_3$ .

$a_1$ [ $\frac{m}{\circ}$ ]	$a_2$ [-]	$b_1$ [ $\frac{m}{\circ}$ ]	$b_2$ [-]
0.041	2.050	0.107	0.560

parameter  $\varphi$ . Ultimately, the goal is to express the earth pressure through  $D$ ,  $L$  and  $\varphi$ .

### 7.1 Investigation of $\beta_1$ and $\beta_3$

The parameters  $\beta_1$  and  $\beta_3$  are investigated as a pair, since they both contribute to the limit value for  $y/D$  going towards infinity as described in section 6.3. The investigation of  $\beta_1$  and  $\beta_3$  is done by plotting the sum  $\beta_1 + \beta_3$  and the product  $\beta_1 \beta_3$  against the basic parameters  $D$ ,  $L$  and  $\varphi$  to discover any trend in the data. To get the actual values for  $\beta_1$  and  $\beta_3$ , two equations with two unknowns have to be solved. In this particular case, it is seen that the sum and product could be described as linear functions of the types,

$$\beta_1 + \beta_3 = a_1 \frac{\varphi}{L} + a_2, \quad (15)$$

$$\beta_1 \beta_3 = b_1 \frac{\varphi}{L} + b_2. \quad (16)$$

Figures 14 and 15 show the data and the best linear fit.

The coefficient for the two linear functions are seen in table 4.

### 7.2 Investigation of $\beta_2$ and $\beta_4$

Subsequently to examining the linear fit of  $\beta_1$  and  $\beta_3$ , these two parameters are locked in the non-linear fitting. This means that the non-linear fit is done again, this time only for  $\beta_2$  and  $\beta_4$ . The slope parameters  $\beta_2$  and  $\beta_4$  are

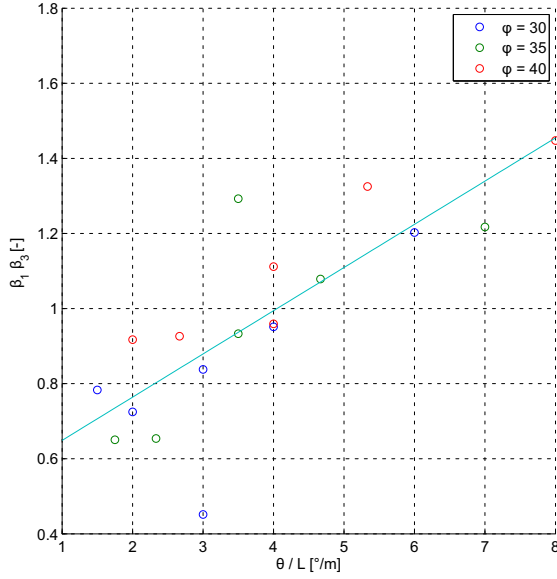


Figure 15: Examination of  $\beta_1 \beta_3$  as a function of  $\frac{\varphi}{L}$ .

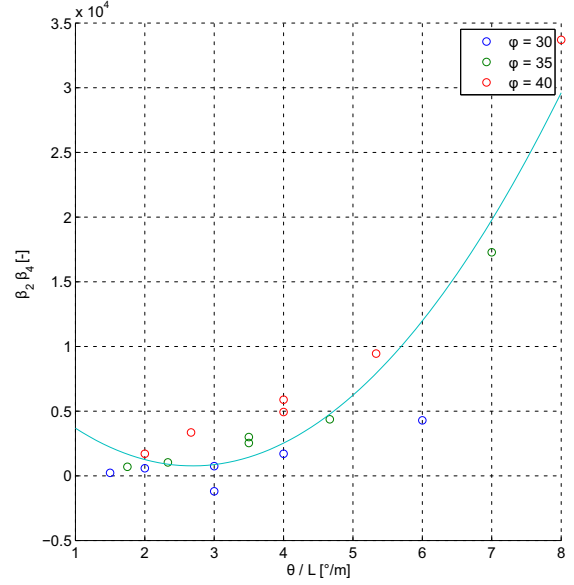


Figure 17: Examination of  $\beta_2 \beta_4$  as a function of  $\frac{\varphi}{L}$ .

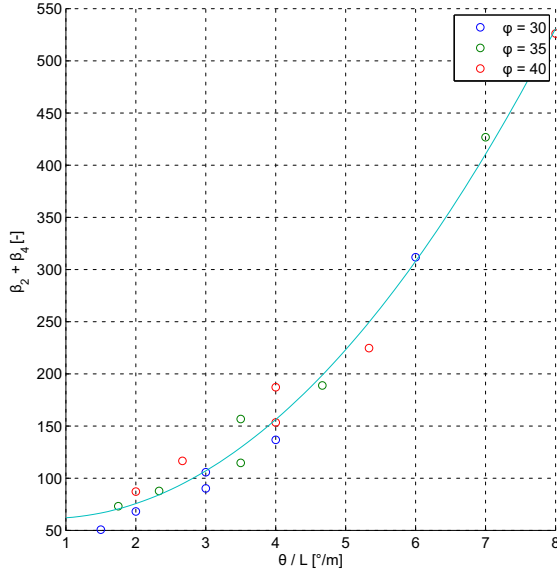


Figure 16: Examination of  $\beta_2 + \beta_4$  as a function of  $\frac{\varphi}{L}$ .

examined using the same procedure as for  $\beta_1$  and  $\beta_3$ , using the sum and the product. From the examination, it is found that the best fit for  $\beta_2$  and  $\beta_4$  are found to be a polynomial fit in the form,

$$\beta_2 + \beta_4 = c_1 \left(\frac{\varphi}{L}\right)^2 + c_2 \left(\frac{\varphi}{L}\right) + c_3, \quad (17)$$

$$\beta_2 \beta_4 = d_1 \left(\frac{\varphi}{L}\right)^2 + d_2 \left(\frac{\varphi}{L}\right) + d_3, \quad (18)$$

Again, the coefficients of the fit are found. They can be seen in table 5. The actual plot of the data and the best quadratic fit can be seen in figures 16 and 17.

Table 5: Coefficients in the fit of  $\beta_2$  and  $\beta_4$ .

$c_1$	$c_2$	$c_3$	$d_1$	$d_2$	$d_3$
$\left[\left(\frac{m}{\circ}\right)^2\right]$	$\left[\frac{m}{\circ}\right]$	$[-]$	$\left[\left(\frac{m}{\circ}\right)^2\right]$	$\left[\frac{m}{\circ}\right]$	$[-]$
8.900	-13.12	66.24	936.5	-4579	5989

### 7.3 Assessment of Mathematical Model

After developing the mathematical model it is compared to the best fit done by non-linear curve fitting. Figure 18 shows the two functions and the original data. It shows relatively good coherence between the best fit and the mathematical model. The quality of the fit based on the mathematical model of course varies, but in general the quality is good. The worst results are gained from the models with  $\varphi = 30^\circ$ . Obviously, greater effort could be put into the development of this mathematical model - especially regarding the connection between the basic parameters,  $D$ ,  $L$  and  $\varphi$ , and the fitting parameters,  $\beta_1$ ,  $\beta_2$ ,  $\beta_3$  and  $\beta_4$ . In this case, the fitting parameters were examined as a function of  $D$ ,  $L$ ,  $\varphi$ ,  $\varphi/D$  and  $\varphi/L$ , and as shown, the coherence was best in the case of  $\varphi/L$ . No significant trend based on the bucket diameter  $D$  was found. This matter should be examined further. Ultimately, the mathematical model is rather simple even though it uses ten fitted parameters as input. A more precise model could possibly be developed, but it would without any doubt involve substantially more complex expressions. The user should assess whether this formulation is adequate for use in the specific case.

## 8 Conclusion

From the numerical analysis of the lateral displacement of the bucket foundation and the corresponding soil response in the drained condition, a general expression

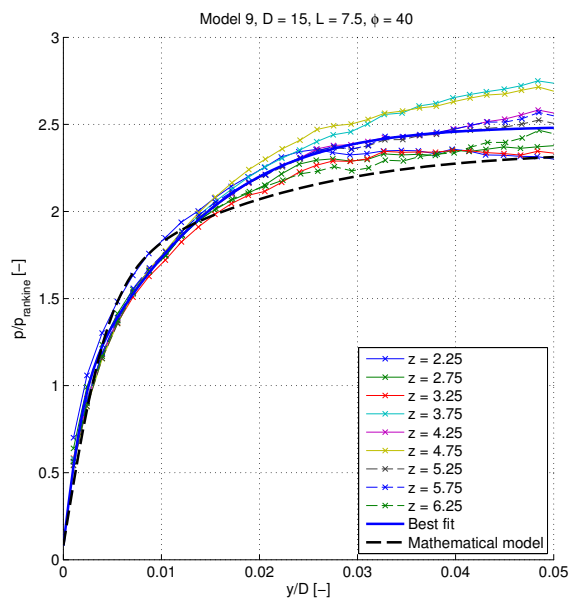


Figure 18: Comparison between best fit with free parameters and the mathematical model.

for obtaining the soil pressure is given for an arbitrary bucket diameter, bucket skirt length and internal angle of friction of the surrounding soil. This enables fast computation of the soil pressure to be used in analytical design models. When designing numerous bucket foundations for e.g. an offshore wind turbine park, it is important that the stabilising pressures on the skirt sides can be calculated readily but still accurately enough to provide a safe but still efficient design.

## 9 Further Work

In the formulation of the mathematical model, ten empirical parameters were necessary. Further calibration of these parameters by doing more models with varying geometry and strength parameters is a straight-forward expansion of the investigations and could help increase the validity of the formulation. The numerical tests done in this project have all been drained tests for a typical offshore sand. A natural way to expand the work and obtain further results, would be to perform the same tests in the undrained condition. In nature, the behaviour of the bucket foundation will be much influenced by the build up and dissipation of pore pressure in and around the bucket skirts. However, in nature neither completely drained or undrained conditions can be assumed - this depends solely on the nature of the loading. A more probable scenario is that the actual behaviour is somewhere in between completely drained and undrained - namely partially drained. The partially drained state will be examined in a scaled experiment in the pressure tank at Aalborg University in the Spring 2013. This project will try to clarify the behaviour of the bucket foundation when subjected to loading with varying velocity.

## References

- Brinkgreve, Engin, and Swolfs, 2012.** R.B.J. Brinkgreve, E. Engin, and W.M. Swolfs. *Manual for PLAXIS 3D 2012*, 2012.
- Brødbæk, Møller, Sørensen, and Augustesen, 2009.** K.T. Brødbæk, M. Møller, S.P.H. Sørensen, and A.H. Augustesen. *Review of p-y relationships in cohesionless soil*. 2009.
- Place, 2012.** Jesper Brade de Place. *Assessment of p-y curves for monopile foundations*, 2012.
- Det Norske Veritas, 1992.** Det Norske Veritas. *Foundations: Classification Notes no. 30.4*, 1992.
- Hansen, Rasmussen, and Wolf, 2012.** Mette Hansen, Kristian Lange Rasmussen, and Torben Kirk Wolf. *Assessment of p-y Curves from Numerical Methods for a Non-Slender Monopile in Cohesionless Soil*. 2012.
- Jensen, Mohr, Mortensen, Hansen, Hansen, Sørensen, Bager, Laustsen, Plum, Svensson, Søndergaard, Adelhøj, Munch-Andersen, Cornelius, Hansen, Goltermann, Steinfeld, Sørensen, and Borchersen, 2009.** Bjarne Chr. Jensen, Gunnar Mohr, Bo Mortensen, Lars Pilegaard Hansen, Svend Ole Hansen, Finn Olaf Precht Sørensen, Dirch H. Bager, Henning Laustsen, Carsten Munk Plum, Eilif Svensson, Ejnar Søndergaard, Johan Adelhøj, Jørgen Munch-Andersen, Thomas Cornelius, Lars Zenke Hansen, Per Goltermann, Jørgen S. Steinfeld, Carsten S. Sørensen, and Egil Borchersen. *Teknisk Staabi*. Nyt Teknisk Forlag, 20. edition, 2009.
- Ovesen, Fuglsang, and Bagge, 2009.** Niels Krebs Ovesen, Leif Fuglsang, and Gunnar Bagge. *Lærebog i Geoteknik*. 978-87-502-0961-4. Polyteknisk Forlag, 2009.
- Vaitkunaite, 2012.** Evelina Vaitkunaite. *Guidelines for length of extended interfaces for bucket foundations*. 2012.



## **Recent publications in the DCE Technical Memorandum Series**

DCE Technical Memorandum no. 31, Determination of p-y Curves for Bucket Foundations in Sand Using Finite Element Modeling, Bjørn Staghøj Knudsen, Martin Underlin Østergaard, Lars Bo Ibsen and Johan Clausen, June 2013.

DCE Technical Memorandum no. 32, Implementation of a Stress-dependent Strength Material Model in PLAXIS 3D, Bjørn Staghøj Knudsen, Martin Underlin Østergaard and Johan Clausen, June 2013.

DCE Technical Memorandum no. 33, Small-scale Testing of Bucket Foundations in Sand, Bjørn Staghøj Knudsen, Martin Underlin Østergaard and Lars Bo Ibsen, June 2013.



# Implementation of a Stress-dependent Strength Material Model in PLAXIS 3D

Bjørn Staghøj Knudsen  
Martin Underlin Østergaard  
Johan Clausen





Aalborg University  
Department of Civil Engineering

**DCE Technical Memorandum No. 32**

# **Implementation of a Stress-dependent Strength Material Model in PLAXIS 3D**

by

Bjørn Staghøj Knudsen  
Martin Underlin Østergaard  
Johan Clausen

June 2013

© Aalborg University

## Scientific Publications at the Department of Civil Engineering

**Technical Reports** are published for timely dissemination of research results and scientific work carried out at the Department of Civil Engineering (DCE) at Aalborg University. This medium allows publication of more detailed explanations and results than typically allowed in scientific journals.

**Technical Memoranda** are produced to enable the preliminary dissemination of scientific work by the personnel of the DCE where such release is deemed to be appropriate. Documents of this kind may be incomplete or temporary versions of papers—or part of continuing work. This should be kept in mind when references are given to publications of this kind.

**Contract Reports** are produced to report scientific work carried out under contract. Publications of this kind contain confidential matter and are reserved for the sponsors and the DCE. Therefore, Contract Reports are generally not available for public circulation.

**Lecture Notes** contain material produced by the lecturers at the DCE for educational purposes. This may be scientific notes, lecture books, example problems or manuals for laboratory work, or computer programs developed at the DCE.

**Theses** are monographs or collections of papers published to report the scientific work carried out at the DCE to obtain a degree as either PhD or Doctor of Technology. The thesis is publicly available after the defence of the degree.

**Latest News** is published to enable rapid communication of information about scientific work carried out at the DCE. This includes the status of research projects, developments in the laboratories, information about collaborative work and recent research results.

Published 2013 by  
Aalborg University  
Department of Civil Engineering  
Sohngaardsholmsvej 57,  
DK-9000 Aalborg, Denmark

Printed in Aalborg at Aalborg University

ISSN 1901-7278  
DCE Technical Memorandum No. 32

# Implementation of a Stress-Dependent Strength Material Model in PLAXIS 3D

Bjørn S. Knudsen<sup>1</sup> Martin U. Østergaard<sup>1</sup> Johan Clausen<sup>2</sup>

*Department of Civil Engineering, Aalborg University*

## Abstract

To perform tests on bucket foundations, full-scale testing is rarely used since it is rather expensive. Instead small-scale testing is done to examine the static and dynamic behaviour of such structures. In the laboratory at Aalborg University, small-scale testing of offshore support structures can be performed in a pressure tank, where a pressure can be applied in order to simulate deep water situations. Since the test set-up is downscaled 15 to 30 times compared to real-life structures, stresses and strains will be downscaled too. For soils, normally a Mohr-Coulomb failure criterion is used, and in the region of small stresses, a non-linear behaviour is observed - unlike the linear behaviour normally assumed in Mohr-Coulomb. To better model this non-linearity, a stress-dependent model for the strength of the soil material is sought to be implemented in PLAXIS 3D through FORTRAN to improve the computational accuracy of small-scale tests.

## 1 Introduction

Small-scale testing in geotechnical engineering is very often used to simulate or clarify behaviour of support structures of various kind. Because of the scaling of these structures, it is often hard to make an accurate model - analytical or numerical - since the behaviour of the soil is very dependent on the stress state inside the soil volume. This fact has long been well known cf. Krabbenhøft et al. (2011), but traditional geotechnical models have not been able (or not needed) to take this into account when designing these structures. To ease the burden for geotechnical designers, tools such as PLAXIS 3D have been developed. Contained in PLAXIS 3D are the most commonly used material models - none of which have the ability to simulate small-scale experiments where low stresses increase the relative soil strength.

This article aims to successfully implement in PLAXIS 3D a user defined soil model (UDSM) that through stress-dependent strength in a better way reproduces real-life behaviour of soil. Firstly, a mathematical formulation is presented based on Krabbenhøft et al. (2011). After this, it is outlined how to implement this model into PLAXIS 3D using the PLAXIS 3D-interface and calculation engine. The application of the model is then tested firstly by fitting the parameters in the failure surface of the mathematical formulation to results gained from triaxial tests on Aalborg University Sand No. 1 (Ibsen and Bødker, 1994). Afterwards it is tested

through comparisons between the new formulation and the existing Mohr-Coulomb formulation within PLAXIS 3D and small-scale tests performed on bucket foundations.

## 2 Theory

The soil mechanics concerning the UDSM will be outlined in the following. The UDSM has the ability to calculate the strength based on the current stress state.

### 2.1 Failure Surface

The formulation of the failure surface is based on Krabbenhøft et al. (2011). Even though the implementation aims towards PLAXIS 3D, the default geotechnical formulation is used where tension is negative and compression is positive, which is contrary to the common finite element formulation. The failure surface  $f$  is formulated as,

$$f = k_0\sigma_3 - \sigma_1 + s_{c0} \left( 1 - \exp \left( -a \frac{\sigma_3}{s_{c0}} \right) \right) = 0, \quad (1)$$

where  $\sigma_1$  and  $\sigma_3$  are the largest and the smallest principal stresses respectively,  $k_0$  defines the slope of the asymptote,  $s_{c0}$  defines the intersection with the  $\sigma_1$ -axis and  $a$  defines the curvature. Equation (1) can then be reformulated into,

$$\sigma_1 = k_0\sigma_3 + s_{c0} \left( 1 - \exp \left( -a \frac{\sigma_3}{s_{c0}} \right) \right). \quad (2)$$

The formulation of the criterion goes towards an asymptote, when  $\sigma_3$  goes towards a very large positive value,

<sup>1</sup>M.Sc. Student, Department of Civil Engineering, Aalborg University, Denmark

<sup>2</sup>Associate Professor, Department of Civil Engineering, Aalborg University, Denmark

e.g. very high compression. Thus the formulation becomes,

$$\sigma_1 = k_0 \sigma_3 + s_{c0} \quad , \quad \sigma_3 \rightarrow \infty. \quad (3)$$

In geotechnics the soil strength is often described by the triaxial angle of friction, since this parameter resembles a physical characteristic and is a parameter in the Mohr-Coulomb failure formulation. To link the parameters described in this failure surface to the triaxial angle of friction, it is used that,

$$k = \frac{d\sigma_1}{d\sigma_3} = k_0 + a \exp\left(-a \frac{\sigma_3}{s_{c0}}\right) = \frac{1 + \sin \varphi}{1 - \sin \varphi}, \quad (4)$$

and thus, the triaxial angle of friction is linked to the parameters of the failure surface from equation (1).

## 2.2 Plastic Potential

The plastic potential  $g$  is, as opposed to the yield surface, governed by the internal angle of dilation  $\psi$ . In associated plasticity, where  $\psi = \varphi$ , this results in  $g = f$ . Assuming associated plasticity results in a much simpler theoretical solution, but in reality, associated plasticity does not resemble the behaviour of soils. In this particular case, the plastic potential is given as seen in equation (5) again assuming no cohesive behaviour,

$$g = m_0 \sigma_3 - \sigma_1 + s_{c0} \left(1 - \exp\left(-b \frac{\sigma_3}{s_{c0}}\right)\right) = 0. \quad (5)$$

From this, two new parameters are introduced,  $m_0$  and  $b$ . It is assumed that it is possible to compute the internal angle of dilation  $\psi$  from the relative density  $I_D$  and  $\sigma_3$  as,

$$\psi = 0.195 I_D + 14.9 (\sigma_3')^{-0.0976} - 9.95. \quad (6)$$

Similarly to equation (4),  $m$  can be described by the internal angle of dilation  $\psi$  as,

$$m = m_0 + b \exp\left(-b \frac{\sigma_3}{s_{c0}}\right) = \frac{1 + \sin \psi}{1 - \sin \psi}, \quad (7)$$

where the parameters  $m_0$  and  $b$  related to the dilative behaviour can be fitted to the data set calculated from equation (6). The value of  $s_{c0}$  needs to remain the same in both situations. (Ibsen et al., 2009)

## 2.3 Fitting of Failure Criterion

The criterion can be calibrated to be used with any material exhibiting Mohr-Coulomb-like behaviour. In this study the criterion is fitted to be used with Aalborg University Sand no. 1. In order to calibrate the parameters a series of triaxial tests are used, in which the backpressure is varied to give failure points at different stress levels. The data from these tests can be seen in table 1. Since the curvature of the criterion is dominant at low stress levels, a series of tests including very low back pressures are used. The tests are carried out at the

Table 1: Test data used for fit.

Test no.	$I_D$ [%]	$\sigma_3$ [kPa]	$q^{failure}$ [kPa]
9301_12	78	5	45
9301_11	81	10.1	64
9301_10	81	20.1	102
9301_04	81	39.9	189
9301_02	81	100.2	412
9301_03	80	160.7	632
9301_07	79	320.1	1218
9301_08	78	640.2	2251
9301_32	79	800.2	2714

Table 2: Parameters of the failure criterion.

$k_0$ [-]	$s_{c0}$ [kPa]	$a$ [-]	$m_0$ [-]	$b$ [-]
4.3584	75.1295	2.9954	1.5507	0.31118

Geotechnical Laboratory at Aalborg University and are available in the data report by Ibsen and Bødker (1994).

The calibration is done by fitting equation (2) to the failure points of each triaxial tests, represented by the coordinate set  $(\sigma_3^{failure}, \sigma_1^{failure})$ . The three remaining unknown constants of equation (2) are found by a non-linear least squares regression algorithm. The data points and the fitted expression are shown in figures 1 and 2. Similarly, the parameters associated to the plastic potential are fitted through a non-linear fit. This is done by assuming that  $m$  can be described in a manner similar to  $k$ , comparing equations (4) and (7). The parameters for Aalborg University Sand no. 1 at  $I_D \approx 80\%$  are listed in table 2. By using equation (4), the equivalent angle of friction can be plotted for the different stress levels, which is shown in figure 3 and by using equation (7) for the equivalent angle of dilation in figure 4. In figure 4 the data points for each of the tests are shown as well. The internal angle of dilation for these data points have been calculated using equation (6).

## 3 Implementation in PLAXIS 3D

To make use of the UDSM with stress-dependent strength along with the user interface and calculation engine in PLAXIS 3D, a certain procedure must be followed. The procedure will be outlined in the following.

Basically, PLAXIS 3D provides all necessary inputs for the UDSM, and it must be able to handle three objectives.

1. Initialization of needed state variables
2. Calculation of stresses using a constitutive model
3. Creation of elastic and effective stiffness matrices

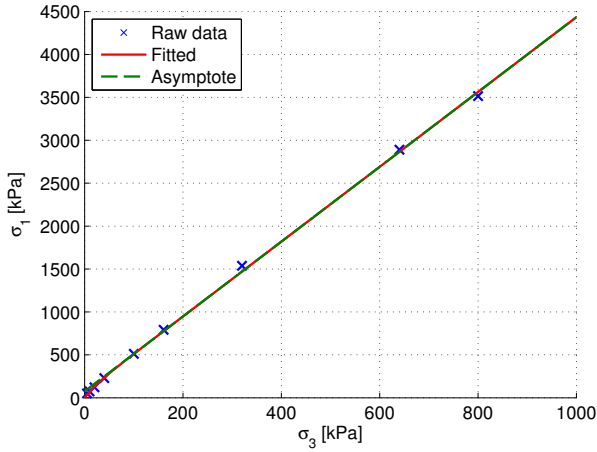


Figure 1: Fit of failure criterion to  $(\sigma_3, \sigma_1)$ -data.

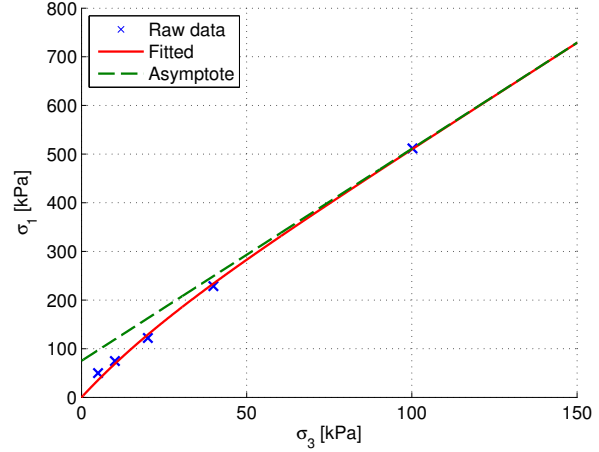


Figure 2: Zoom of figure 1. From this it is apparent that for small values of  $\sigma_3$ , the non-linear behaviour is important.

In this particular case, no state variables are used, however this could be e.g. the mean stress  $p'$ . The creation of the elastic stiffness matrix is done readily based on material parameter input done in the user interface in PLAXIS

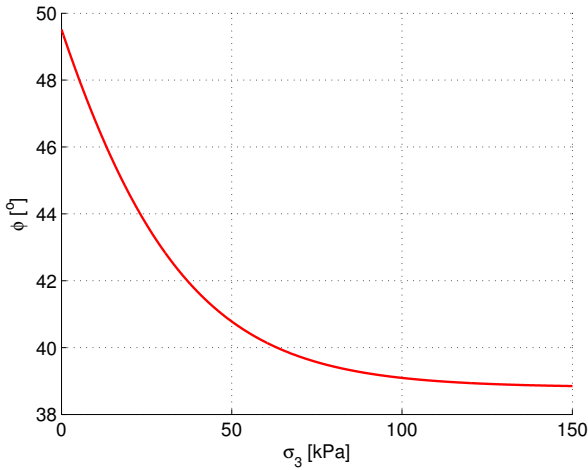


Figure 3: Internal angle of friction as a function of  $\sigma_1$ .

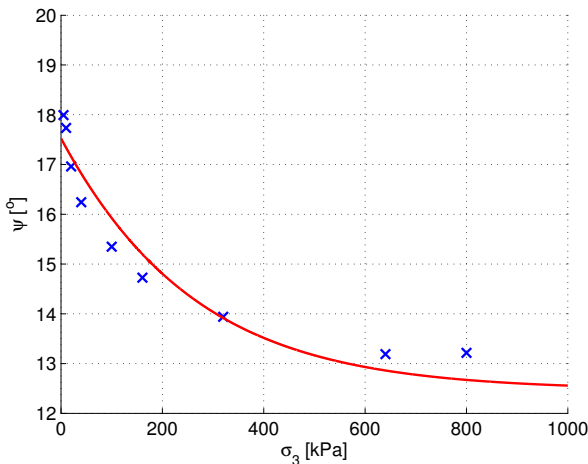


Figure 4: Internal angle of dilation as a function of  $\sigma_1$ .

3D. The creation of the effective stiffness matrix is performed by a stress return algorithm that calculates an allowable stress state for the soil, if the stress is outside the failure surface. The mechanics of these algorithms will not be of further subject in this paper.

## 4 Application of Material Model

In the following section, the application of the material model is tested. This is done in various ways as described below. The general method is to compare the actual test data with the results from various PLAXIS 3D models done with the linear Mohr-Coulomb model already implemented in PLAXIS 3D and the recently implemented non-linear Mohr-Coulomb model.

- The SoilTest-function in PLAXIS 3D is used to perform a triaxial test of the implemented material model with the fitted parameters on a soil volume, which is compared to triaxial tests that the material model parameters have been fitted against, and to SoilTest-results with the linear Mohr-Coulomb model.
- PLAXIS 3D is used to model a small-scale test of a bucket foundation and the results of this are compared to the actual test results. The PLAXIS 3D-model is done using both the traditional linear Mohr-Coulomb failure envelope and the non-linear Mohr-Coulomb failure envelope.

### 4.1 Comparison between SoilTest and Triaxial Tests.

In order to make use of the SoilTest-function in PLAXIS 3D that is able to perform triaxial tests, elastic parameters ( $E, \nu$ ) are needed apart from the fitted parameters defining the failure ( $k_0, s_{c0}, a, m_0, b$ ).

Since the implemented model is a linear elastic-perfectly plastic model with non-linear Mohr-Coulomb failure criterion, the elastic path will not be portrayed

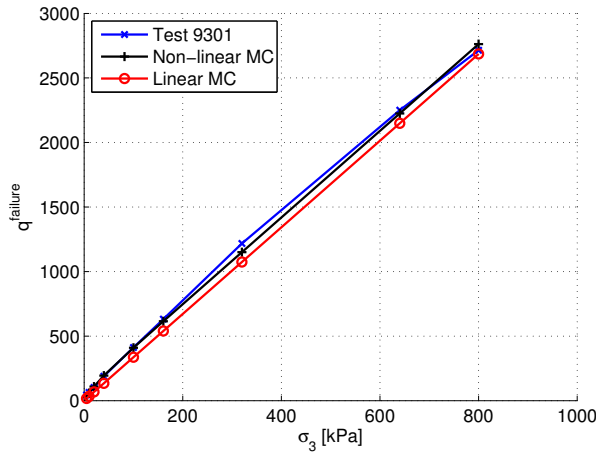


Figure 5: Plot of  $q_f$  for different  $\sigma_3$  for all three approaches to determine failure.

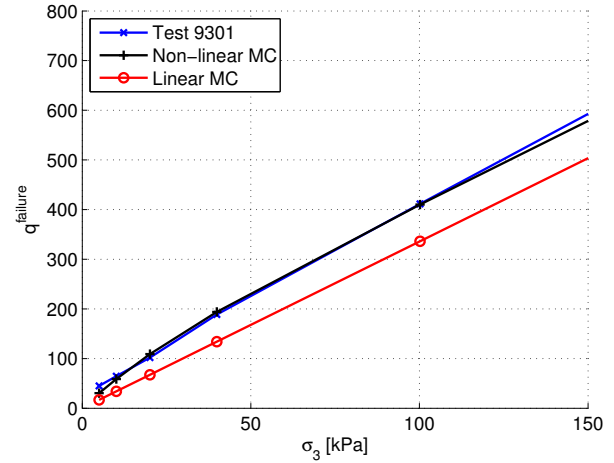


Figure 6: Zoom of figure 5. From this it is clear that the Linear MC underestimates the failure load, and that the Non-linear MC is almost similar to the test data.

properly in any case. That means in fact that only the stress at failure will be of interest.

The deviatoric stress at failure  $q^{failure}$  will be examined for five triaxial tests at different  $\sigma_3$ . The non-linear Mohr-Coulomb has five input parameters for the failure criterion and two elastic parameters. The linear Mohr-Coulomb has three input parameters - the effective cohesion  $c' = 0$  for non-cohesive materials, the internal angle of friction  $\phi$ , and the internal angle of dilation  $\psi$  - and two elastic parameters. Since only  $q^{failure}$  is of interest, the elastic parameters will not be mentioned any further. As the linear Mohr-Coulomb model only allows for constant values of  $\phi$  and  $\psi$ , the asymptotic value of these will be used, which is  $\phi_{asympt} = 38.8^\circ$  and  $\psi_{asympt} = 12.6^\circ$  according to the fitted expression, see also figures 3 and 4, respectively.

Figures 5 and 6 show the comparison of the different approaches to determine the deviatoric stress at which failure occurs. It is evident from the results that the linear Mohr-Coulomb underestimates  $q^{failure}$  in general. The same thing applies to some degree for the non-linear Mohr-Coulomb, especially for very low  $\sigma_3$ . This underestimation is caused by the fact that the fitted model underestimates  $\phi$ , cf. figure 2. For  $\sigma \geq 5$  kPa the non-linear Mohr-Coulomb shows to accurately estimate  $q^{failure}$ .

#### 4.2 Comparison between PLAXIS and Small-scale Test

In the previous section, it was shown that the non-linear Mohr-Coulomb provides a better estimate of the failure stress for a triaxial test at low backpressure than the traditional linear Mohr-Coulomb. In the following, an actual small-scale test done on a bucket foundation in the laboratory will be examined. The goal is to model the scaled bucket test in PLAXIS 3D using both the linear and the non-linear Mohr-Coulomb criterion

and compare the results of the failure moment to the small-scale test results.

The static small-scale test that will be examined is described in Larsen (2008a) and documented in detail in Larsen (2008b). The test setup consists of a sandbox in which the bucket foundation is installed. Through a loading frame, vertical load can be applied. The horizontal load is applied at a distance above the sand surface to exert the bucket foundation to a moment. The test setup is seen in figure 7. All tests described in Larsen (2008a) are performed on Aalborg University Sand No. 1. In each test performed, the relative density  $I_D$  is measured. Since the failure criterion for the non-linear Mohr-Coulomb model is calibrated against triaxial tests at a certain relative density, the sand used in the small-scale test must be of similar relative density compared to the triaxial tests.



Figure 7: Test setup for scaled bucket foundations. (Larsen, 2008a)

#### Bucket Test No. 0104.1701

The basis for this comparison is 'Bucket test no. 0104.1701' (Larsen, 2008b). Two similar tests have been

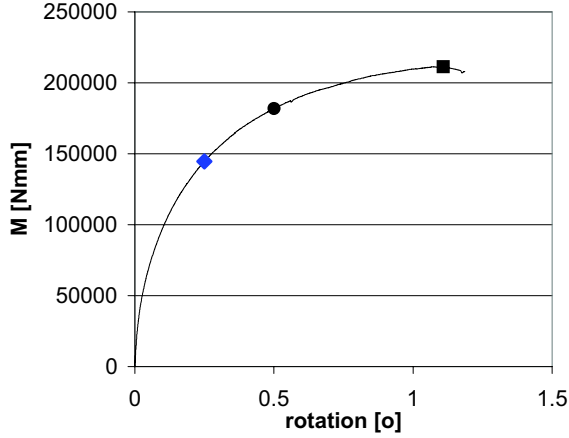


Figure 9: Moment-rotation curve for 'Bucket test no. 0104.1701'.

executed as well, 'Bucket test no. 0104.901' and 'Bucket test no. 0104.1901'. These tests were done for a bucket with diameter  $D = 300$  mm, skirt length  $L = 300$  mm and with no vertical load. The horizontal load was applied in a height of 2610 mm. The relative density in the specific test is  $I_D = 86\%$ . This in turn means that the parameters in the non-linear Mohr-Coulomb criterion have been calibrated against a looser soil. Force and displacement are tracked in the test, which makes it possible to compute moment and rotation at sand surface. Since non-linear elasticity is not implemented in neither of the two materials models, only failure moment is examined. A schematic display of the test setup is shown in figure 8. The setup is duplicated in the numerical model using both linear and non-linear Mohr-Coulomb failure criterion. Since it is not always obvious when a finite

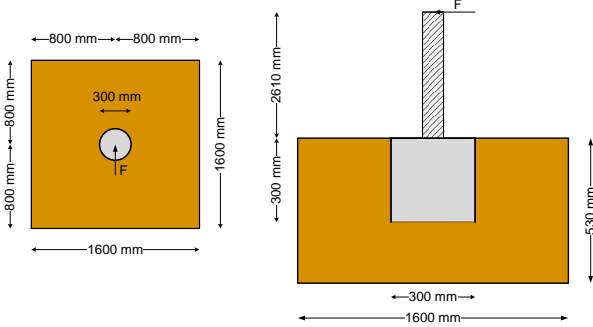


Figure 8: Test setup for 'Bucket test no. 0104.901'. (Larsen, 2008b)

element has failed, a point of failure normally needs to be chosen. In this case, the rotation of the bucket will be examined, and the failure moment will be chosen as the moment at a rotation of  $\theta_{\text{failure}} = 1.11^\circ$ , which is the rotation at failure in 'Bucket test no. 0104.1701'. Figures 9 and 10 show the actual moment-rotation for the test and the finite element models, respectively.

At a rotation of  $\theta_{\text{failure}} = 1.11^\circ$ , table 3 shows the moment at failure. It is evident that the failure moment for the test is higher than the linear Mohr-Coulomb model as expected, since the linear Mohr-Coulomb model does

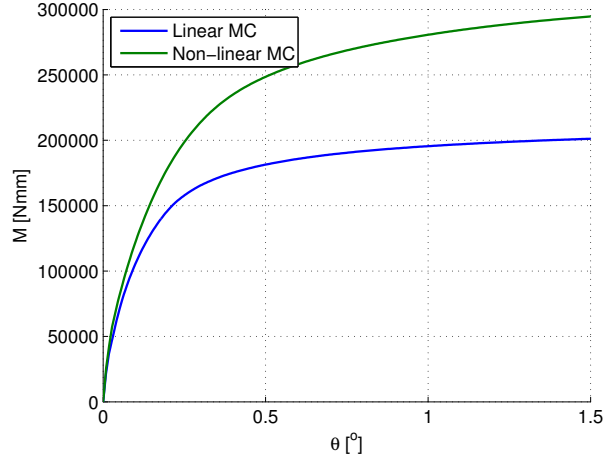


Figure 10: Moment-rotation curve for Linear MC and Non-linear MC.

Table 3: Comparison of failure moment at  $\theta_{\text{failure}} = 1.11^\circ$ .

Test 0104.1701	Linear MC	Non-linear MC
213773 Nmm	197063 Nmm	284612 Nmm

not take the strength increase for low stresses into account. The non-linear Mohr-Coulomb model does however take this into account, and it was expected that this model would come closer to test results, although still underestimating failure moment because the non-linear failure criterion was calibrated against a looser soil than the one used in 'Bucket test no. 0104.1701'. The reason this is not the case, could perhaps be that the failure moment in the test is too low because the sand was loosened from raising the water level from the bottom of the sand container after leveling the sand. It is evident from Larsen (2008a) that this was done for some tests, while in others the water level was raised from the top of the sand container. It is however not clear in which tests, which approach was used. It could be argued that the non-linear Mohr-Coulomb model has not failed for a rotation of  $1.11^\circ$ , since the  $M - \theta$  diagram at that point does not tend towards the asymptotic moment. Although the FE-results were not completely in line with the test results, the non-linear Mohr-Coulomb model still exhibits higher strength for low stresses present in small-scale setups like the one examined. This proves that the non-linear Mohr-Coulomb failure criterion behaves as expected. Regarding the comparison with the test results, more work should go into the modeling of the small-scale test in PLAXIS 3D.

## 5 Conclusion

The main goal of this study was to successfully implement a material model with stress-dependent strength in PLAXIS 3D. The stress-dependent strength was obtained through a non-linear Mohr-Coulomb failure criterion. This objective was achieved without encoun-

tering severe problems. From the implementation in PLAXIS 3D, the material model was tested in several ways, against existing test results and the linear Mohr-Coulomb failure criterion. These comparisons showed that the non-linear MC-model accurately depicted the deviatoric failure stress for a series of triaxial tests with varying backpressure. The model seemed to be less accurate for a static bucket foundation test performed in small-scale at Aalborg University (Larsen, 2008a), but the non-linear MC-model exhibited the correct behaviour compared to the linear MC-model. It was concluded that more effort should go into the built of the FE-model. Ultimately, the stress-dependent material model was implemented with success and ongoing work regarding the implementation of non-linear stiffness will result in a material well-suited for predicting the behaviour of small-scale tests.

## 6 Further Work

In recent years, computational methods such as the finite element method have moved to become an essential tool for every geotechnical engineer or scientist. The demand within the fields of offshore geotechnical research calls for the use of small-scale models or computer models, meaning that the demand for accurate soil models is increasing. For soils in general, the stress state within the soil volume is of great importance, which has been a well known fact for many years. In this study, the goal has been to implement a soil material model that takes the stress-dependent strength of non-cohesive soils into account into PLAXIS 3D. PLAXIS 3D has since it was published been widely used within the field of geotechnical engineering. PLAXIS 3D has been developed and improved during the years, adding more soil material models, but not a single model able to take the stress-dependent strength into account has been added.

Through a non-linear Mohr-Coulomb relationship, the stress-dependent strength is taken into account in a linear elastic-perfectly plastic soil model. The implementation has proven to be successful, and after calibration of the failure criterion of the model, the comparison with the test results showed that more work needs to be put into the FE-model of the small-scale test. The non-linear MC-model did however behave just as expected and the comparison to the triaxial test results supports this. To further improve the soil material model, non-linear elasticity needs to be implemented. This should enable the material model to take stress-dependent stiffness into account. This will enable a better representation of the path towards failure, since the currently implemented model only predicts failure. Another addition of the soil model is hardening and softening.

In this study, the material parameters have been

calibrated towards nine triaxial tests for a certain sand, Aalborg University Sand No. 1. Further studies should include the calibration of the failure parameters towards more different types of sand. Since no general description of the material parameters have been developed, a general description could aim to take the relative density, the maximum or minimum void ratio, or the average grain size into account, so material model parameters could be determined in ways other than calibration towards triaxial tests.

## References

- Ibsen and Bødker, 1994.** Lars Bo Ibsen and Lars Bødker. *Data Report 9301: Baskarp Sand No 15*, 1994.
- Ibsen, Hanson, Hjort, and Thaarup, 2009.** Lars Bo Ibsen, M. Hanson, T. Hjort, and M. Thaarup. *MC-Parameter Calibration for Baskarp Sand No. 15*. 2009.
- Krabbenhøft, Clausen, and Damkilde, 2011.** Sven Krabbenhøft, Johan Clausen, and Lars Damkilde. *The Bearing Capacity of Circular Footings in Sand: Comparison between Model Tests and Numerical Simulations Based on a Nonlinear Mohr Failure Envelope*. *Advances in Civil Engineering*, Volume 2012, Article ID 947276, 10 pages, doi:10.1155/2012/947276, 2011.
- Larsen, 2008a.** Kim André Larsen. *Static Behaviour of Bucket Foundations, vol. 1*, 2008.
- Larsen, 2008b.** Kim André Larsen. *Static Behaviour of Bucket Foundations, vol. 2*, 2008.



## **Recent publications in the DCE Technical Memorandum Series**

DCE Technical Memorandum no. 31, Determination of p-y Curves for Bucket Foundations in Sand Using Finite Element Modeling, Bjørn Staghøj Knudsen, Martin Underlin Østergaard, Lars Bo Ibsen and Johan Clausen, June 2013.

DCE Technical Memorandum no. 32, Implementation of a Stress-dependent Strength Material Model in PLAXIS 3D, Bjørn Staghøj Knudsen, Martin Underlin Østergaard and Johan Clausen, June 2013.

DCE Technical Memorandum no. 33, Small-scale Testing of Bucket Foundations in Sand, Bjørn Staghøj Knudsen, Martin Underlin Østergaard and Lars Bo Ibsen, June 2013.



# Small-scale Testing of Bucket Foundations in Sand

Bjørn Staghøj Knudsen  
Martin Underlin Østergaard  
Lars Bo Ibsen





Aalborg University  
Department of Civil Engineering

**DCE Technical Memorandum No. 33**

# **Small-scale Testing of Bucket Foundations in Sand**

by

Bjørn Staghøj Knudsen  
Martin Underlin Østergaard  
Lars Bo Ibsen

June 2013

© Aalborg University

## Scientific Publications at the Department of Civil Engineering

**Technical Reports** are published for timely dissemination of research results and scientific work carried out at the Department of Civil Engineering (DCE) at Aalborg University. This medium allows publication of more detailed explanations and results than typically allowed in scientific journals.

**Technical Memoranda** are produced to enable the preliminary dissemination of scientific work by the personnel of the DCE where such release is deemed to be appropriate. Documents of this kind may be incomplete or temporary versions of papers—or part of continuing work. This should be kept in mind when references are given to publications of this kind.

**Contract Reports** are produced to report scientific work carried out under contract. Publications of this kind contain confidential matter and are reserved for the sponsors and the DCE. Therefore, Contract Reports are generally not available for public circulation.

**Lecture Notes** contain material produced by the lecturers at the DCE for educational purposes. This may be scientific notes, lecture books, example problems or manuals for laboratory work, or computer programs developed at the DCE.

**Theses** are monographs or collections of papers published to report the scientific work carried out at the DCE to obtain a degree as either PhD or Doctor of Technology. The thesis is publicly available after the defence of the degree.

**Latest News** is published to enable rapid communication of information about scientific work carried out at the DCE. This includes the status of research projects, developments in the laboratories, information about collaborative work and recent research results.

Published 2013 by  
Aalborg University  
Department of Civil Engineering  
Sohngaardsholmsvej 57,  
DK-9000 Aalborg, Denmark

Printed in Aalborg at Aalborg University

ISSN 1901-7278  
DCE Technical Memorandum No. 33

# Small-scale Testing of Bucket Foundations in Sand

Bjørn Staghøj Knudsen<sup>1</sup> Martin Underlin Østergaard<sup>1</sup> Lars Bo Ibsen<sup>2</sup>

*Department of Civil Engineering, Aalborg University*

## Abstract

For offshore foundation structures, the loads are of varying nature both in magnitude and duration. For the bucket foundation the dissipation of the pore pressure is highly relevant since it greatly affects the strength of the structure. The build up of pore pressures with varying loading rate is therefore a highly relevant research subject. In computational models, e.g. FE-models, normally either a drained or an undrained behaviour is assumed. In real life, the behaviour is partially drained, which calls for a time-dependent model. Especially, the tracking of pore pressures in and around the bucket skirt will provide valuable information of the quasi-static behaviour. For a number of small-scale tests performed in the laboratory at Aalborg University, a bucket foundation will be loaded with varying velocity to investigate the dissipation and general behaviour of bucket foundations used as offshore support structures for wind turbines.

## 1 Introduction

The suction bucket concept for offshore foundation of wind turbines, which is illustrated in figure 1, has been extensively researched for the last decade, among other places at the Geotechnics Department of Aalborg University (AAU). The design procedure and validation of the foundation dimensions have to be verified by risk assessment organizations such as *Det Norske Veritas*. In the current verified design method the ultimate capacity of the bucket foundation is calculated both in the drained and undrained condition whereafter the lowest capacity is chosen. In dense cohesionless soil the response in the drained case will often be significantly lower than the undrained, causing the capacity to be low. As the ultimate limit state loads on offshore structures are often of impulsive nature, i.e. a very large load over a small period of time, arising from emergency stop of the turbine, freak waves or breaking waves in general, this article aims to investigate the behaviour of the foundation as a function of the loading rate. The thesis is that for large loading rates, the drained condition is an underestimation of the capacity of the foundation, causing the design dimension to be overestimated.

The thesis has previously been investigated by conducting tests in the pressure tank at the Geotechnics Laboratory at AAU, cf. (Sjølmo et al., 2012) and (Foglia et al., 2013) among others. The thesis was in these tests validated, however the test setup was not able to conduct the test to a satisfactory degree, mainly due to a limited displacement range of 40 mm of the piston, cf. figure



Figure 1: An illustration of a wind turbine on a bucket foundation. (Universal Foundation A/S, 2013)

4. Since the before mentioned tests were conducted, the test setup has been thoroughly upgraded. The upgrade involves a new actuator, new bucket foundations with greater steel thickness and an addition of five extra pore pressure gauges. Furthermore new control hard- and software has been installed. With the new setup it is possible to exert much larger forces at greater velocities over a larger displacement range. In this article the results of the first four successful tests with the new setup will be analyzed and compared to the previously obtained results.

<sup>1</sup>M.Sc. Student, Department of Civil Engineering, Aalborg University, Denmark

<sup>2</sup>Professor, Department of Civil Engineering, Aalborg University, Denmark

## 2 Theory

The sand in the pressure tank is Aalborg University Sand no. 1, which is thoroughly documented from triaxial tests. The sand resembles sand types commonly encountered offshore. For the calculation of failure sand is defined as being in either a drained or undrained state, representing the two extremes of drainage behaviour. In the tests it is investigated what happens as a transition from fully drained conditions at low loading velocity to a potentially partial or fully undrained behaviour at high loading velocities occurs. A partially undrained behaviour can be experienced when a pore pressure build up is not able to dissipate, which makes the behaviour a function of the drainage conditions and the permeability of the soil.

### 2.1 Development of Pore Pressures

Sand under drained conditions can act both compressional with  $\Delta\varepsilon_v < 0$  and dilatational with  $\Delta\varepsilon_v > 0$  under loading. The change between the two states is called the characteristic state and is characterized by,

$$\frac{\delta\varepsilon_v}{\delta\varepsilon_1} = 0. \quad (1)$$

The point of the characteristic state for different density indices and stress combinations can be plotted in a  $p' - q$  diagram where they form a straight line. This line is called the characteristic line, cf. (Ibsen and Lade, 1997). Sand with stress states below the line thus exhibits compression and stress states above exhibits dilatation. The slope of the characteristic line is called the characteristic angle  $\phi_{cl}$ , and this angle has for Aalborg University Sand no. 1 been found to be independent of the density index, cf. Ibsen and Lade (1998). A schematic overview of the drained behaviour can be seen in figure 2. For the sand to behave fully drained the effective stress path (ESP) and the total stress path (TSP) have to be coincident, as seen in figure 2. This only takes place if the excessive pore pressure formed during volume change of the sand is able to dissipate, which in turn requires the loading rate to be low.

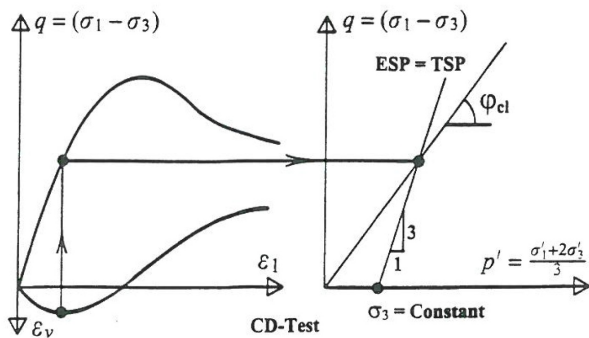


Figure 2: The characteristic state in drained sand. (Ibsen and Lade, 1997)

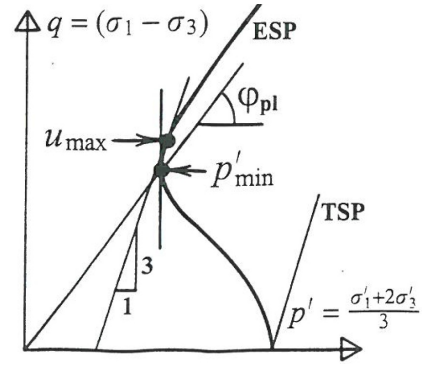


Figure 3: The phase transformation state in undrained sand. (Ibsen and Lade, 1997)

For sand in the undrained state a similar property is seen as the point at which the pore pressure development  $\Delta u$  changes from being positive to negative. This change is associated with compression and dilation of sand in drained behaviour. The state at which the transition takes place is called the phase transformation state, cf. (Ibsen and Lade, 1997). As with the drained case the phase transformation line is a straight line in a  $p' - q$  diagram, cf. figure 3. The phase transition point is defined as the point at which the ESP has a vertical tangent, since the point of maximum pore pressure  $u_{max}$  and minimum effective mean stress does not completely align, cf. figure 3. Once the pore pressure increment is negative the effective pressure state will increase, thus giving the soil extra strength. A sand with a highly dilatational behaviour will therefore have a higher strength. The negative pore pressure increment prevents the sand from dilating as long as the pore pressure is positive, once the pore pressure turns negative, the sand starts to dilate and is no longer fully undrained. As the pore pressure nears the point of cavitation the failure is controlled by the drained failure envelope.

Since the failure point of dense undrained sand occurs once the pore pressure reaches the cavitation limit, the value of the pore pressure in the initial state is important for the total strength. In the undrained state it is thus the total stress state  $p' + u_0$  that is relevant for the strength, and not the effective stress as for the drained case. The combination of  $u_0$  and  $p'$  is furthermore not relevant, only the sum. As a consequence for the sand in the pressure tank, the undrained ultimate capacity will be greatly increased due to the pressure applied, even though the effective stresses are not changed. (Nielsen et al., 2013)

Whether or not the sand will act drained or undrained is a function of the drainage conditions, the permeability of the sand and the loading rate. It has often been found that a high loading rate in saturated sand will cause a dramatic strength increment, sometimes denoted the *boot effect*, originating from trying to pull a boot out of mud. The investigation in this article will clarify if

this effect is present with the bucket foundation, which is expected. The development of pore pressure will furthermore be a function of the failure mechanism, a point where some uncertainties exist in the design methods.

## 2.2 Scaling Effects

In a model test consideration has to be taken, since the investigated phenomenon is a scaled down version of the real-life phenomenon. Using similarity laws along with continuum and fluid mechanics scaling parameters can be derived for the scaling of length, time, force, stress, velocity and time for both the sand and the pore water. The similarity laws state that both geometric, kinematic and dynamic similarity need to be obeyed, for the scaling to be correct. Often the dynamic similarity is the hardest to obtain, since it involves scaling of physical entities such as gravity and viscosity. (Larsen and Brorsen, 2009)

In the model of this article, the primary object is to investigate the influence of the loading velocity on the development of pore pressures and load bearing capacity under horizontal loading. The scaling of the sand and fluid is done without obeying the scaling laws, as e.g. the grain size in the sand is not scaled properly. The consequence of the wrong scaling is that the numerical values of the measured forces and pressures cannot be directly extrapolated from model to real size. This is however acceptable, since investigation of the nature of the phenomena is the goal of this article.

## 3 Test Setup

The quality of the test setup is the key to achieve reliable results from any experiment, scaled or not. The tests described in this document are all scaled experiments performed in the pressure tank at Aalborg University. The reason that the experiments are performed in a pressure tank is that it is possible to apply a pressure, simulating that the foundation is situated below water and allowing a larger decrease in pore pressure before cavitation takes place. In the pressure tank at Aalborg University, it is possible to apply a maximum of 1000 kPa of pressure. An overview of the setup in the pressure tank is seen in figure 4.

### 3.1 Test Setup Overview

The test setup consists of multiple components which will be outlined in the following.

#### *Actuator and Control System*

The force is delivered from a hydraulic actuator which is controlled through a test control unit coupled with a computer. The actuator can be either displacement or force controlled. The actuator can deliver 100 kN of

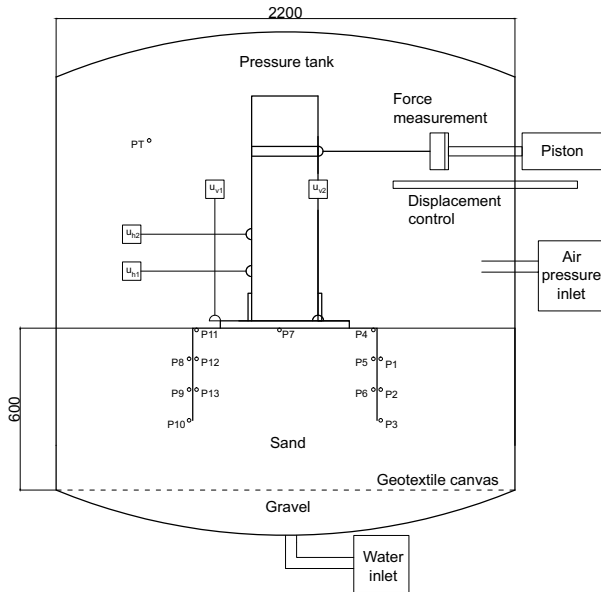


Figure 4: Overview of the pressure tank.

force, it has 500 mm of free range and a maximum velocity of at least 0.5 m/s. The movement of the actuator is controlled through a piece of computer software. In the software, it is possible to monitor movement of the actuator, force through a weight cell connected to the actuator and all the pressure transducers. The test control system also works as data acquisition software.

#### *Bucket, Tower and Wire*

The model bucket is made of stainless steel and has a diameter of 500 mm, a skirt length of 250 mm and a tower height of 610 mm, cf. figure 5. The tower is a galvanized RHS 180 × 100 mm steel profile reinforced at the bottom with two steel plates welded to the flanges. A round plate is mounted on the bottom of the tower to transfer the forces between the tower and the bucket lid via eight bolts. The model is a further development of a previous model, where the steel thickness of the skirt proved to be too small to withstand the development of earth pressures during the loading. In the new model the steel thickness is 10 mm in the lid and 5 mm in the skirt. Between the actuator and the piston a demountable steel wire is used to transfer the force. The whole setup is designed to be able to withstand a force of 100 kN at an eccentricity of 500 mm above the lid.

#### *Measurements*

13 pore pressures are measured on the bucket, cf. figure 5, to track the development during loading. Four displacement transducers are used to track the vertical, horizontal and rotational displacement. The displacement transducers are ASM wire transducers, which are carefully mounted before each test to ensure that the wire are respectively perfectly horizontal or vertical in the initial phase. The force applied via the piston is measured with a 100 kN force cell. The force cell is zeroed before

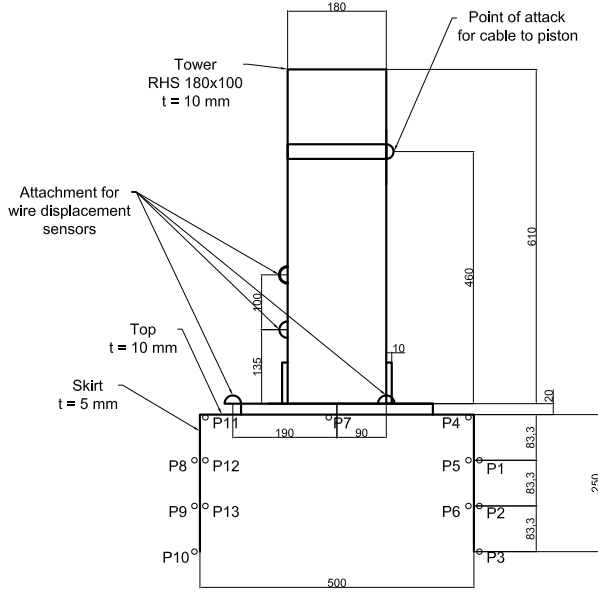


Figure 5: Sketch of the bucket.

each test is started, as it is affected by both the tightening of the wire and the pressure in the tank. This does to some degree cause the numerical value of the measured force to be wrong, but it is however comparable between the tests. The pressure in the tank is measured to ensure that the 200 kPa pressure is applied. The measurements are obtained using both the MOOG system and an older HBM Spider8 system, both are connected to a computer.

## 4 Preparation of Test Setup

Before each test is carried out a procedure for preparing the test setup is followed. The main purpose is to ensure that all the physical and geometrical parameters of the setup are identical in all the tests. The procedure has been investigated and documented in Fisker and Kromann (2004). The procedure is briefly explained in the following.

### 4.1 Preparation of Sand

The sand is prepared by following the points below,

1. Loosening of sand with water gradient
2. First vibration of sand
3. Second loosening of sand with water gradient
4. Second vibration of sand
5. Adjustment of water level in tank

The loosening of the sand is done by applying an upwards gradient of water, causing the effective stress in the sand to be reduced and thus loosening the grains from each other. The effective stress is calculated by,

$$\sigma' = (\gamma_m - \gamma_w \pm i \gamma_w) z, \quad (2)$$

where  $\gamma_m$  and  $\gamma_w$  are the unit weights of respectively sand and water,  $i$  is the gradient of water flow and  $z$  is the depth below the surface. As an upwards gradient of water flow is negative, the effective unit weight is reduced and the sand is loosened. A gradient of  $i = 0.9$  is applied, which is equivalent to a pressure height difference of 0.54 m. The gradient is applied for a period of 5 minutes, whereafter the water surface in the tank is 5-10 cm above the sand surface. The following vibration is carried out using a vibrator rod that is lowered slowly into the sand until it is approximately 5 cm above the geotextile cover and then pulled slowly out. The slow velocity and the water layer above the sand surface minimizes the risk of creating air pockets in the sand. Before the leveling of the sand the water can be drained to make it easier to do, afterwards the water level is adjusted to approximately 6 cm above the sand.

### 4.2 CPT Testing

Prior to the installation of the model-bucket in the pressure tank CPT-tests are carried out in the prepared sand. This is done to ensure homogeneity in the soil volume. The tests are done using a mini-CPT cone, which is driven into the sand with constant velocity using a hydraulic piston. The CPT cone is mounted on an steel girder that can rotate 360° in the tank and allows for radial adjustment making CPT testing possible everywhere in the tank. Five CPT tests are done prior to each test at respectively the middle and at 90° intervals around the tank at 40 cm from the centre.

The sand in the tank is the Aalborg University Sand no. 1. This sand has been used extensively in the research at the Geotechnics Laboratory at Aalborg University, and its properties are thus very well documented. Using a series of triaxial tests performed with varying backpressure and relative density, a set of formulas has been derived to determine soil parameters from the cone resistance in a mini-CPT test (Ibsen et al., 2009). The following parameters can be determined from the CPT testing,

- Relative density  $I_D$
- Angle of friction  $\phi$
- Angle of dilatancy  $\psi$
- Void ratio  $e$
- Unit weight of the soil  $\gamma$

The relative density is related to the cone resistance and the effective vertical in-situ stress through,

$$I_D = 5.14 \left( \frac{\sigma'_{v0}}{q_c^{0.75}} \right)^{-0.42}, \quad (3)$$

where  $\sigma'_{v0}$  is the effective vertical in-situ stress and  $q_c$  is the measured cone resistance.  $I_D$  is generally defined as,

$$I_D = \frac{e_{\max} - e}{e_{\max} - e_{\min}}, \quad (4)$$

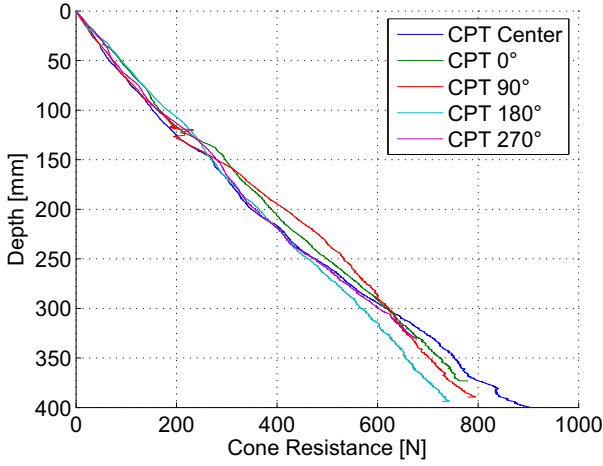


Figure 6: Cone resistance of five cone penetration tests.

with  $e_{\max}$ ,  $e_{\min}$  and  $e$  as the maximum, minimum and current void ratios respectively. The effective in-situ stress can be found from the effective unit weight  $\gamma'$  and the depth  $z$  with,

$$\sigma'_{v0} = \gamma' z, \quad (5)$$

using the effective unit weight of the soil from,

$$\gamma' = \frac{d_s - 1}{1 + e}, \quad (6)$$

where  $d_s$  is the characteristic density of the soil equal to 2.64 for Aalborg University Sand no. 1. With the equations (3) to (6) an iterative procedure can be used to find  $\gamma'$ ,  $I_D$  and  $e$ . Empirical formulas to determine the triaxial angle of friction and dilatation fitted from a series of triaxial tests are seen in equations (7) and (8),

$$\phi_{tr} = 0.152 I_D + 27.39 (\sigma'_{h0})^{-0.2807} + 23.21, \quad (7)$$

$$\psi_{tr} = 0.195 I_D + 14.86 (\sigma'_{h0})^{-0.09764} - 9.946, \quad (8)$$

where  $\sigma'_{h0} = \sigma'_{v0} (1 - \sin(\phi_{tr}))$ ,  $I_D$  is in percent and stresses are in kPa. With the presented set of formulas it is thus possible to achieve an estimate of specific soil parameters at each CPT location, which can be compared. Often the greatest difference will be present in the measure of relative density, where a difference between the CPTs of maximum 0.05 is accepted. If the difference is greater than 0.05 a third vibration procedure must be applied.

An example of the results of five CPT tests is shown in figure 6, where the cone resistance is plotted against the depth. During the preparation of the four tests presented in this article, some technical difficulties were encountered, meaning no usable CPT tests were done before test 2 and 3. Since the same preparation procedure has been used every time, and the results hereof have been good, the soil properties are assumed to be within the acceptable range. The results are thus treated similar for all tests.

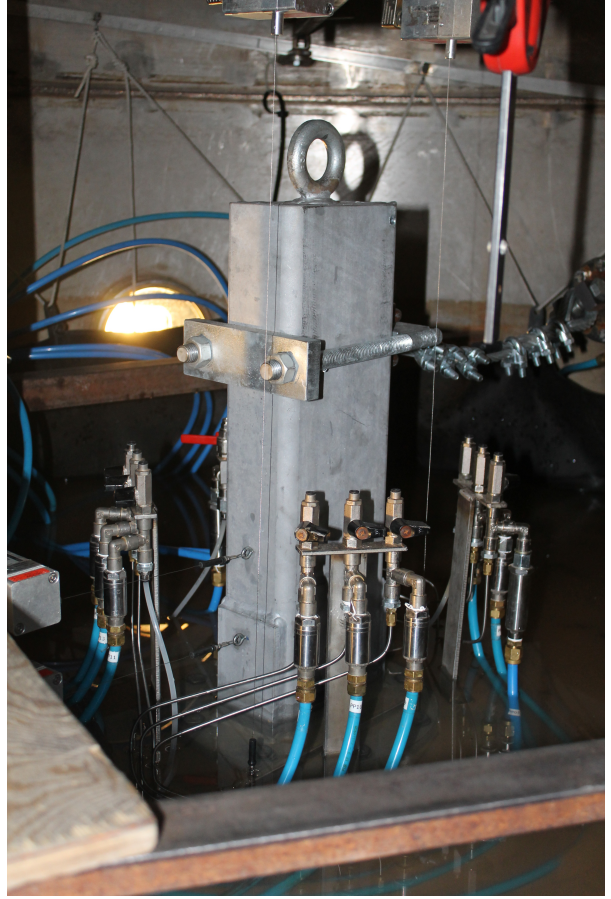


Figure 7: Picture of the bucket ready for testing.

#### 4.3 Installation of Bucket

When the sand is prepared and the CPT results are accepted, the bucket is installed in the centre of the tank using the hydraulic piston also used for the CPTs. The installation will cause disturbance in the sand volume, and is thus carried out step-wise to allow for dissipation of excess pore pressure to minimize the effects of the disturbance. As the speed of the installation piston is not changeable, the procedure is not optimal. It is however the same procedure for all tests, and should as such not have an influence on the validity of the results. Upon finishing the installation of the bucket all the measuring equipment is fitted and the horizontal hydraulic actuator is attached with a steel wire. The bucket equipped and ready for test can be seen in figure 7.

#### 4.4 Applying Pressure to the Tank

After the installation the tank is sealed off and the compressor is set to 200 kPa of pressure relative to the atmospheric pressure. The build up of pressure is monitored with the MOOG system until an equilibrium at approximately 200 kPa is found and is then left overnight for the pressure state in the entire sand volume to stabilize. The test setup is thus fully prepared for testing.

Table 1: Overview of loading velocity for the tests.

Test no.	1	2	3	4
Velocity [mm/s]	0.10	1.00	10.0	100

## 5 Overview of Tests

A total of four successful tests are used for the results in the article. All of the tests are carried out with a horizontal displacement of the actuator of 150 mm applied at varying velocities. Table 1 shows the different test velocities. In the previous tests in Sjelmo et al. (2012) it was investigated if a very low loading rate (0.01 mm/s) behaved as drained condition, which was the case. A test with this loading rate is therefore not redone.

## 6 Results

In the following selected results from the four tests are shown. A very large quantity of data is produced in the tests, and only relevant results for underlining the points made are shown. All the test data is however treated, and the trend shown in this article is a picture of the general trends. Earlier analyses of similar tests have been made in Sjelmo et al. (2012) and Foglia et al. (2013), and these results will be compared with the new tests.

### 6.1 Force and Displacement

The recorded displacements  $v_1$ ,  $v_2$  and  $h_1$  are all transformed to the resultant horizontal (H), vertical (V) and rotational ( $\theta$ ) displacements of the bucket with reference to the middle of the bucket lid. This reference point is used, as the actual rotation point of the bucket moves during loading and thus is not suitable. The procedure is iterative as the elongation of the wires in the transducers are influenced by all displacement components. In the iteration algorithm it is assumed that

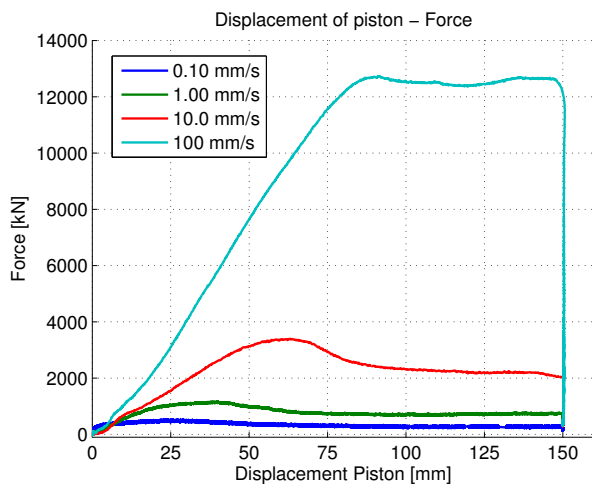


Figure 8: Force measurement as a function of the displacement of the piston.

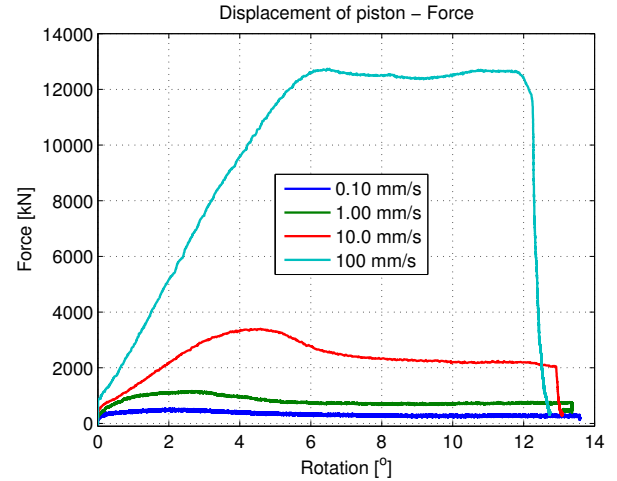


Figure 9: Force measurement as a function of the rotation of the bucket.

the displacements of the bucket can be divided into the three separate components that are mutually dependent on each other. The four monotonic loading tests differ only in loading velocity and consequently also duration. For all four tests the development of the force as a function of the actuator displacement and rotation of the bucket is shown in figures 8 and 9.

From the results it can be seen that as the displacement rate increases the measured necessary force to apply the displacement increases as well, which was expected. It is evident that the bearing capacity is highly rate dependent. In contrary to the previous tests done in Sjelmo et al. (2012), all the models have reached failure within the span of the displacement. While test 1, 2 and 3 reach an easily determinable peak, the fastest test 4 reaches a maximum force, which is then constant the rest of the loading phase. This indicates that the cavitation limit is reached at which no more capacity is available in the pore water. For all the tests the maximum force and the piston displacement and rotation of the bucket at the maximum points are shown in table 2. It is seen that the higher the displacement rate, the larger the rotation is before the maximum capacity is reached.

The vertical, horizontal and rotational displacement of the tests shown together with the force development is seen in figure 10. The difference between the resultant final horizontal displacement in the four tests is most pronounced, as it decreases with each increment in

Table 2: Maximum force, displacement of piston  $d_p$  and rotation  $\theta$  of the bucket.

Test	Max Force [N]	$d_p$ [mm]	$\theta$ [°]
0.10 mm/s	538.6	22.8	1.9
1.00 mm/s	1168.8	38.6	2.6
10.0 mm/s	3399.4	63.1	4.6
100 mm/s	12741.9	91.7	6.5

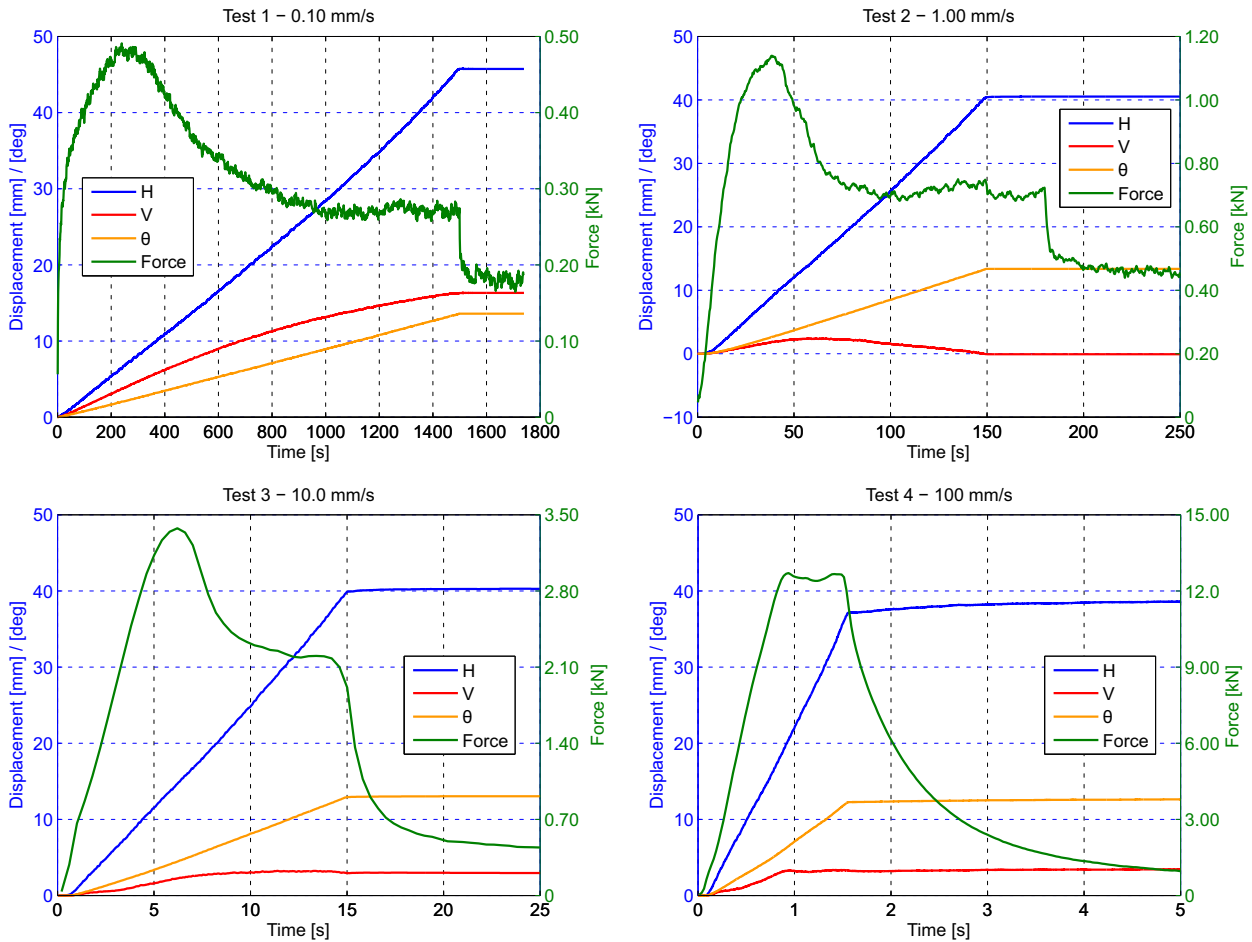


Figure 10: Displacement and force for all four tests. Test 2, 3 and 4 are zoomed in on the loading period.

the loading rate. The resultant vertical and rotational displacement also decrease with increasing loading rate, however the change here is not as large. In test 2 the vertical displacement first increases during the loading but then goes back to zero in the end of the loading. This effect is not clearly present in any of the other models, and can perhaps be a measurement error. Generally the displacements of the bucket decrease in magnitude as the loading rate increases. An explanation for this phenomenon is that the slower the loading rate, the easier it is for the pore water to dissipate, thus causing an increase in effective stresses which then cause a deformation in the soil. This effect is especially evident in test 1, as the vertical displacement here is very large compared to the other tests. The upwards vertical displacement is greatly influenced by the dissipation of negative pressure inside the bucket, i.e. pore water flowing from outside the bucket to the inside. With the low loading rate the change in pore pressure is almost balanced by the inflow of pore water.

## 6.2 Initial Stiffness

While it has been shown in the previous section that the lateral response of the bucket foundation is highly dependent on the loading rate when it comes to large dis-

placements and ultimate capacities, it has earlier been shown, e.g. in Foglia et al. (2013) that the initial stiffness is independent on the loading rate. This is of interest, since the vast majority of the environmental loading will be small loads where the initial stiffness is important. The initial stiffness is furthermore interesting in dynamic investigation, which is however outside the scope

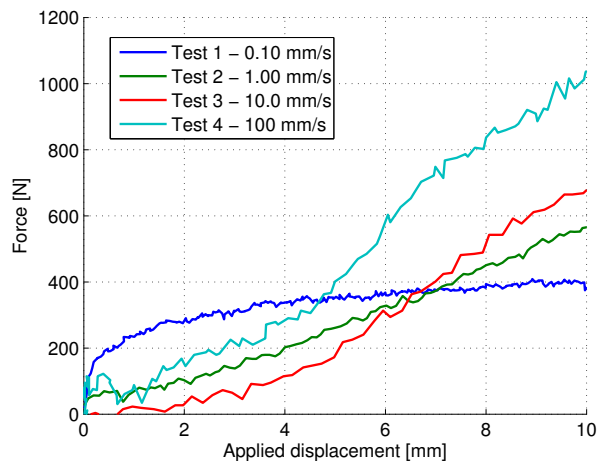


Figure 11: The force exerted in the first 10 mm of applied displacement.

of this article. The force exerted in the first 10 mm of applied displacement for all four tests is shown in figure 11. The response of test 1 is somewhat different than the other three tests, which is attributed to the very low loading rate. Tests 2-4 all show a very similar response for the first part of the applied displacement, with slopes of the force-displacement curve being similar. This is in good correlation with earlier findings, and the results from this article further verifies this phenomenon.

### 6.3 Pore Pressure Development

The pore pressure was recorded during all the tests in the locations shown in figure 5. As an example, the pore pressure development over time plotted together with the force development for test 3 is shown in figures 12 and 13. The pressure measurements are divided in the seven gauges inside of the bucket in figure 12 and the six gauges on the outside of the bucket in figure 13.

The build up of suction is as expected directly correlated with the applied force caused by the displacement. The build up is considerably larger inside the bucket, which is caused by flow-barrier effect from the impermeable skirt. A few of the pressure gauges show some irregularities in the results. This is namely P5 on the inside, which was expected to be somewhere between P4 and P6, and P7 which differ significantly from the two other gauges at the top P4 and P11. The irregularity in the results of P7 has been observed in all of the tests and could be caused by a slightly different method of instrumentation, as this gauge is placed directly under the mounting of the tower and therefore has a long and soft tube from the measuring point to the pressure transducer. Another, perhaps more likely, explanation is that the rotation point of the bucket is placed close to P7, causing the displacement of the bucket in this point to be smaller.

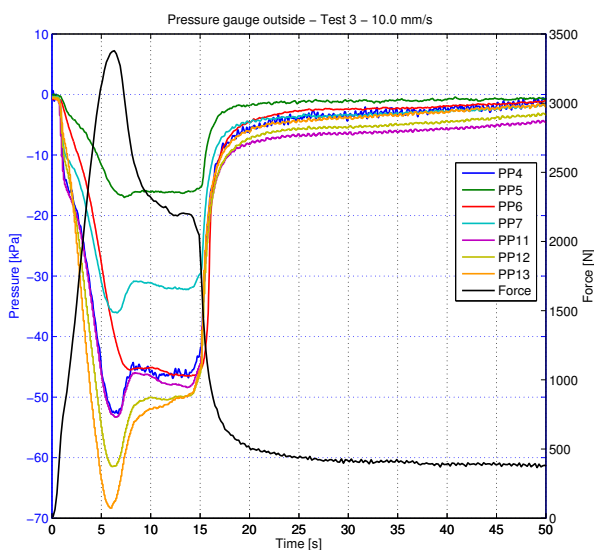


Figure 12: Pore pressure inside bucket during test 3.

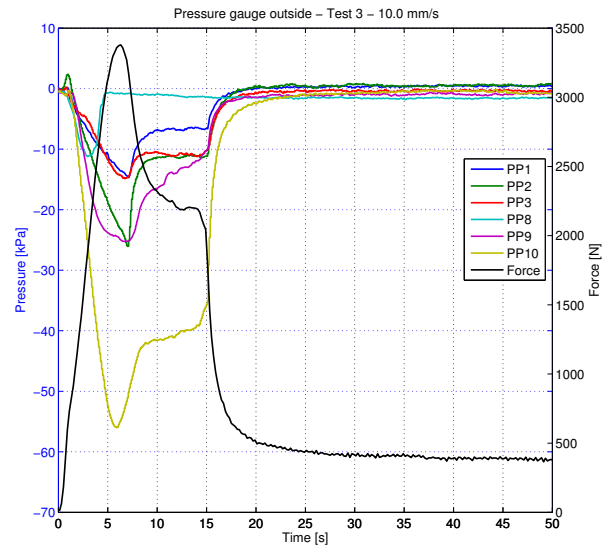


Figure 13: Pore pressure outside bucket during test 3.

The gauges away from the loading direction show the largest change in pressure, gauges P11, P12 and P13, however the top gauges P4 and P11 show very similar results, indicating a uniform pressure distribution on the lid if P7 is ignored. From the gauges on the outside, the trend is not as clear. The gauges closest to the surface P1 and P8 show the smallest pressure change, which is due to the very short drainage path.

From figure 10 it was shown that a significant strength increase takes place as the loading rate grows. This is an indication that while the drained condition might be suitable to calculate the capacity at low loading rates, it is not the case for a quite high loading rate. This is backed up by the results of test 3 examined in figure 12 and 13, which is not even the fastest loading rate.

The maximum pore pressure build up in all four tests is shown together in figures 14 to 16. The distribution on the lid, cf. figure 14 is similar in all four tests. The two side gauges P4 and P11 show almost the same maximum value, while P7 reaches only approximately 65 % of the maximum value in tests 2-4. As earlier pointed out, this could mean that the measurement is partly erroneous. In the execution of the tests problems with the P7 gauge occurred, especially due to difficulties with fully saturating the transducer and connecting tube. Another conclusion is that the pressure distribution is not constant on the lid. In the tests done in Sjelmo et al. (2012) this phenomenon was not clearly visible.

The pressures along the back skirt, i.e. away from the loading direction, are seen in figure 15. These results can be compared to the results in Sjelmo et al. (2012), as the test setup herein had pressure gauges in the same positions on the back skirt. The outside pressures show a pressure distribution that is increasing non-linearly with the depth, which is consistent with previous results.

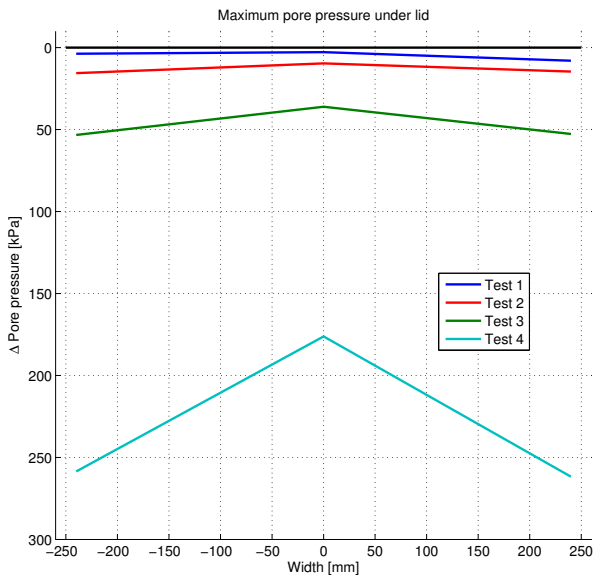


Figure 14: Force measurement as a function of the displacement of the piston.

The magnitude of the pressures significantly increases with the growth in loading rate as expected from the force measurements. The magnitude in the 100 mm/s test is 241.1 kPa at the bottom, which is below the cavitation limit. The fastest previous test was 10 mm/s, however this test did not show failure due to a very short loading distance, and the maximum pressures are thus not comparable.

The pressures on the inside of the back skirt are all larger than the corresponding pressures on the outside. Both the bottom point on the inside and outside are P10, as the pressure is recorded at the tip of the skirt. The pressure is slightly larger at P13 in all the tests,

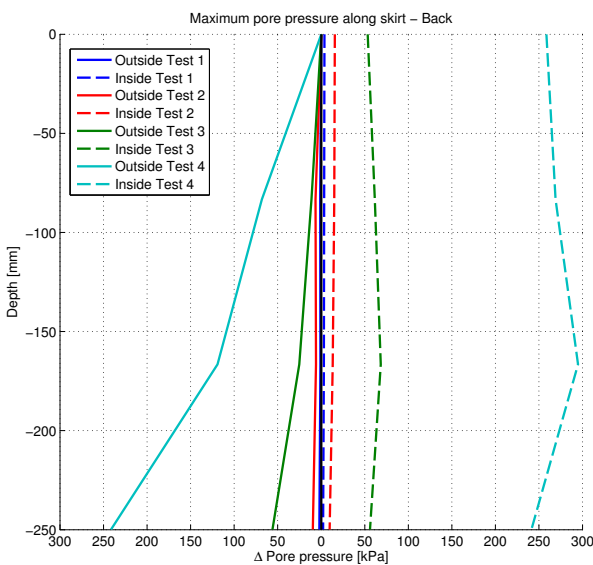


Figure 15: Force measurement as a function of the displacement of the piston.

however a discontinuity in the pressure at P12 as found in Foglia et al. (2013) is not present. The pressure at P13 is the maximum measured pressure, which is close to the cavitation limit of approximate -290 kPa.

The pressures on the front skirt of the bucket, cf. figure 16, during loading have not been investigated earlier, and can therefore not be compared with previous results. The pressure on the outside is increasing with depth from P1 to P2, while the pressure at P3 is significantly lower. This could be caused by the rotation of the bucket, indicating the location of the rotation point being close in depth to P3. The pressures inside the front skirt follow a different trend compared to the back skirt. Firstly the magnitude of the pressures are smaller, but also a discontinuity is present at P5 2/3 up the skirt, before the pressure increases to that of the lid. As proposed in Foglia et al. (2013), a discontinuity could be caused by the drainage pattern.

In figure 17 the absolute pressure difference for P13 is shown for all four tests, with the time normalized with respect to the loading time. P13 is chosen since it shows the maximum measurements for all tests and it has one of the most distinct developments. For test 1 the response is very low, and can thus be considered almost completely drained. For test 2 and 3 an increment in pore pressure is seen, which does however become constant after respectively 0.2 and 0.4 of the normalized time. These tests can therefore be classified as partially drained, as the pore pressure cannot be increased indefinitely.

Test 4 shows an increase in pressure that is almost linear up to a plateau of around 275 kPa after which the increase is slightly slower. This test is therefore classified as substantially undrained, if not completely.

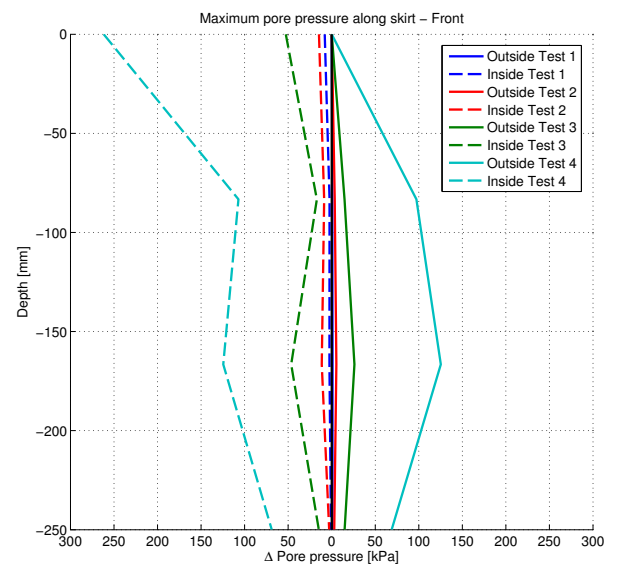


Figure 16: Force measurement as a function of the rotation of the bucket.

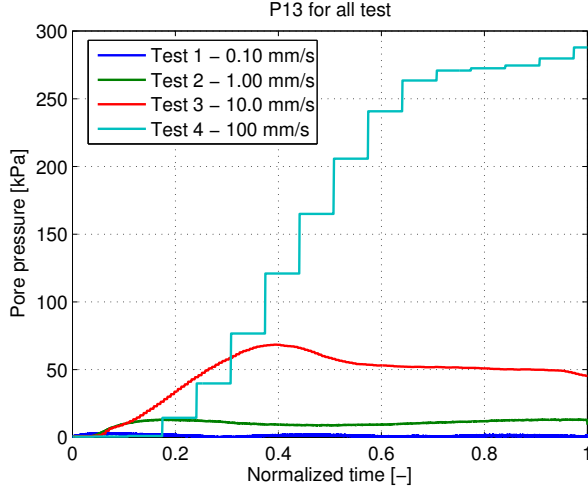


Figure 17: P4 for all tests with time normalized to loading time.

The absolute value of the pressure is below the cavitation limit, however the decrease in slope indicates that the limit is close. For high loading rates and relatively large displacements the response can according to these results be classified as significantly more resistant to applied load than what the drained condition predicts.

#### 6.4 Capacity as Function of Loading Rate

From the four different loading rates, it is investigated if the increase in ultimate capacity can be expressed with a mathematical expression. Firstly the failure load, cf. table 2, is normalized with the failure load of the slowest test, as it is assumed to be the drained capacity. A power function,

$$F_{\text{norm}} = a v_1^b, \quad (9)$$

where  $F_{\text{norm}}$  is the normalized force,  $v_1$  is the loading rate and  $a$  and  $b$  are fitting parameters, is fitted to the data points. The data points and the fit are seen in figure 18. It is evident that the development follows a power fit for the range of tests performed. It is expected that the strength increase reaches a plateau at around the level of the fastest test caused by the cavitation limit. Whether this is the case needs further investigation in future tests. The parameter of the fit is seen in table 3.

#### 6.5 Non-dimensional Analysis

It was in Foglia et al. (2013) investigated whether the test results could be fitted to a non-dimensional function. The results are made non-dimensional by assuming a relationship,

$$\Delta p \propto \left( \frac{1}{k}, \frac{1}{T_L}, L_d, \gamma_w \right), \quad (10)$$

where  $k$  [m/s] is the permeability of the soil,  $T_L$  [s] is the loading period,  $L_d$  [m] is the drainage length assumed proportional to the skirt length  $L$  and  $\gamma_w$  [N/m<sup>3</sup>] is the unit weight of the soil. While the loading period  $T_L$ , and

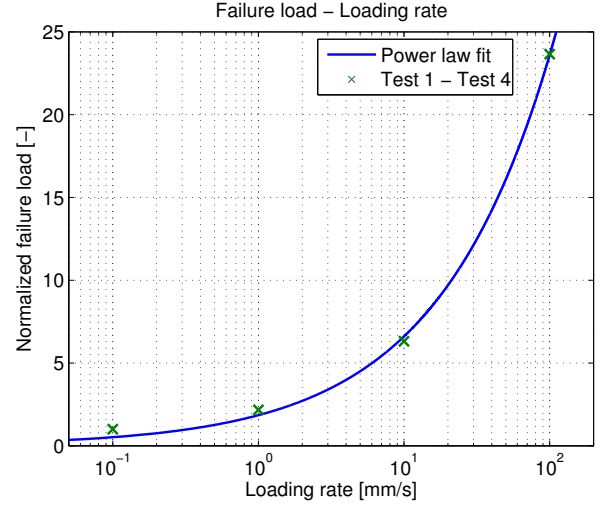


Figure 18: The normalized failure loading plotted against the loading rate.

the unit of it, is a term from dynamic loading, it is assumed that the loading rate can be used instead, despite having a wrong unit. The non-dimensional group is thus,

$$\frac{\Delta p}{\gamma_w L} = f \left( \frac{L}{k T_L} \right). \quad (11)$$

The function  $f$  is unknown, and a fit with a power function is examined,

$$\frac{\Delta p}{\gamma_w L} = c \left( \frac{L}{k T_L} \right)^d. \quad (12)$$

With the parameters  $c$  and  $d$  being fitting parameters. The data from pressure gauges P4 and P11 are used, since these gauges show the maximum response under the lid. For each of the four tests the maximum value is chosen from the dataset, making the non-dimensional group an expression of the maximum obtained pressure difference for a given soil, loading rate and geometry. With the two gauges chosen there are thus eight data points in total with four different loading rates. In figure 19 the data points are shown together with the fitted function. The fitted parameters are seen in table 3. The fitted power law follows the data points quite good and is somewhat an indication that a function of this type is suitable. More test data should be used before a final function can be fitted to the data.

## 7 Conclusion

The new test equipment in the pressure tank has been implemented and four successful tests have been executed. The displacement rates used ranged from 0.1

Table 3: The fitted parameters of equations (9) and (12).

$a$	$b$	$c$	$d$
1.848	0.553	$1.033 \cdot 10^5$	-0.654

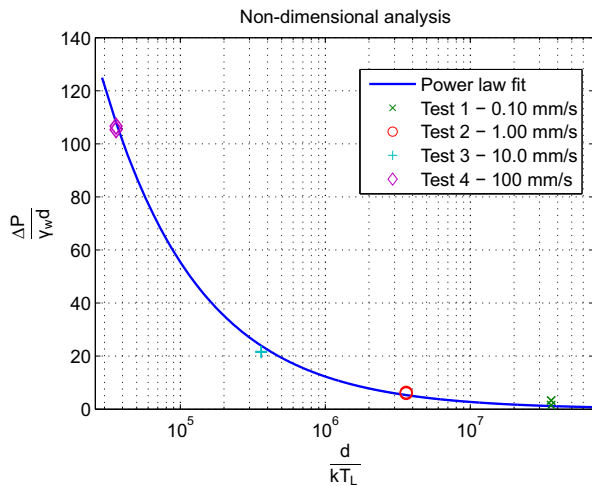


Figure 19: Non-dimensional analysis of maximum pore pressure development.

mm/s to 100 mm/s. The results showed a significant increase in the bearing capacity from approximate 0.5 kN in the slowest test to 12.7 kN in the fastest test. From the displacements gauges it was seen that the overall displacement of the bucket foundation decreased as the loading rate increased. An explanation for this is the lack of sufficient seepage of pore water allowing for deformations with the fast loading rates.

The pore pressure development was tracked by 13 pressure gauges during all four tests. For the slowest test a very low pore pressure change occurred, indicating almost fully drained conditions. As the loading rate increased, the measured pore pressures increased, indicating partially undrained conditions. For the fastest tests the build up of pore pressures increased throughout the entire loading sequence pointing to substantially undrained conditions. There was a clear correlation between the faster loading rates, the build up of pore pressures and the rise in lateral capacity of the foundation.

The pressure distribution of the bucket foundation was found to be similar to earlier investigations, albeit without a discontinuity on the inside of the back skirt. The shape of the distribution was almost identical in all four tests, further proving the reliability of the results. All gauges showed a negative development of pore pressure, meaning suction occurred around the entire bucket under loading.

The initial stiffness of the lateral response was investigated by looking at the first 10 mm of applied displacement. Apart from the slowest test all tests showed a similar response with similar slopes of the force-displacement curve. This proves earlier findings, where the initial stiffness has been found to be independent on the loading rate.

The capacity of the bucket foundation increased with the loading rate in a manner that could be fitted with a power law, more test data is needed to determine whether this trend continues beyond the test rates of this article. Lastly the results from two of the pressure gauges were analyzed using a non-dimensional group. It was found that the development of pore pressures can also be described using a power law, although more test data with different geometries is needed to improve the reliability of the findings.

Overall the initial thesis of the article proved to be verified by all the findings in the treatment of the results.

## 8 Further Work

The results put forward in this article are a product of the very first tests with the new test-setup in the pressure tank at the Geotechnics Laboratory at Aalborg University. During the work in the laboratory several useful experiences with the setup and new equipment were made, which continuously leads to optimization of the whole setup. In time this will lead to better tests, which can further validate the points presented in this article.

During the analysis of the test results it was found that the signals from the transducers were polluted with noise to a quite large degree. The noise present was of varying amplitude for the various signals, and could indicate problems with the wiring and soldering of the cables and plugs. Further work could involve trying to minimize this noise.

The tests 1 to 4 showed in the article are all done with a foundation with  $L/D = 0.5$ . Further work in the laboratory involves similar testing with suction buckets of other dimensions, already now tests with a  $L/D = 1.0$  bucket are planned. Furthermore the test setup is able to handle cyclic loading and two-way loading, which can further be used to analyze the behaviour of the suction bucket foundation type.

## References

- Fisker and Kromann, 2004.** L.B. Fisker and K. Kromann. *Cyklisk Belastning af Bøttefundament i Tryktank - Speciale*, 2004.
- Foglia, Ibsen, Nielsen, and Mikalauskas, 2013.** A. Foglia, L.B. Ibsen, S.K. Nielsen, and L. Mikalauskas. *A Preliminary Study on Bucket Foundations under Transient Lateral Loading*. 2013.
- Ibsen, Hanson, Hjort, and Thaarup, 2009.** Lars Bo Ibsen, M. Hanson, T. Hjort, and M. Thaarup. *MC-Parameter Calibration for Baskarp Sand No. 15*. 2009.
- Ibsen and Lade, 1997.** L.B. Ibsen and P.V. Lade. *A study of the phase transformation and the characteristic lines of sand behavior*. 1997.
- Ibsen and Lade, 1998.** L.B. Ibsen and P.V. Lade. *The Role of the Characteristic Line in Static Soil Behavior*. 1998.
- Larsen and Brorsen, 2009.** Torben Larsen and Michael Brorsen. *Lærebog i Hydraulik*. 978-87-7307-691-0. Aalborg Universitetsforlag, 2009.
- Nielsen, Ibsen, Sørensen, and Shajarati, 2013.** Søren Kjær Nielsen, Lars Bo Ibsen, Kris Wessel Sørensen, and Amir Shajarati. *Undrained Cyclic Behaviour of Dense Frederikshavn Sand*. 2013.
- Sjelmo, Mikalauskas, Ibsen, and Foglia, 2012.** Å. Sjelmo, L. Mikalauskas, L.B. Ibsen, and A. Foglia. *Soil-Structure Interaction in Cohesionless Soils due to Monotonic Loading*. 2012.
- Universal Foundation A/S, 2013.** Universal Foundation A/S. *Press material*. URL: <http://www.universalfoundation.dk/en/press/10/7/5>, 2013. Downloaded: 29-05-2013.

## **Recent publications in the DCE Technical Memorandum Series**

DCE Technical Memorandum no. 31, Determination of p-y Curves for Bucket Foundations in Sand Using Finite Element Modeling, Bjørn Staghøj Knudsen, Martin Underlin Østergaard, Lars Bo Ibsen and Johan Clausen, June 2013.

DCE Technical Memorandum no. 32, Implementation of a Stress-dependent Strength Material Model in PLAXIS 3D, Bjørn Staghøj Knudsen, Martin Underlin Østergaard and Johan Clausen, June 2013.

DCE Technical Memorandum no. 33, Small-scale Testing of Bucket Foundations in Sand, Bjørn Staghøj Knudsen, Martin Underlin Østergaard and Lars Bo Ibsen, June 2013.



# 2 Conclusion

---

This thesis has been a research study related to different aspects regarding the bucket foundation, an offshore foundation concept developed at Aalborg University. The concept has proven to be feasible in comparison to other types of offshore substructures like the monopile. Research is however still done regarding especially the design and verification of the bucket foundation, and this thesis has been a contribution to that ongoing work. The thesis has dealt with three different areas regarding the bucket foundation, and the results from the investigations will be summarized in the following.

The  $p - y$  curves developed for slender embedded piles have long been the preferred method of designing monopiles, although the behaviour of such structures cannot be compared to the original test piles. For the bucket foundation, which is even less slender than the monopile, a new formulation of  $p - y$  curves is needed to readily and easily design bucket foundations for use in offshore wind farms. The numerical tool PLAXIS 3D was employed in order to determine the soil response for a given displacement. 18 different combinations of geometry and soil strength were examined, ultimately determining ten coefficients for a mathematical model, which can be used to determine the soil response for an arbitrary geometry and soil strength. Although 18 models were examined, the mathematical model needs to be further improved before it is introduced in design tools, since only two different embedment ratios were examined.

An important part of the verification of the bucket foundation has been scaled model tests. An issue in relation to small-scale testing is correct scaling that enables the results from the small-scale test to be used to assess the structure in real life. For soils, this fact is important since the behaviour of the soil is influenced by the stress state within the soil. A material model that takes this fact into account has been developed, and the goal to implement this model in the commercial geotechnical finite element software PLAXIS 3D has been reached. PLAXIS 3D is a widely used tool in both the predesign, the design and the verification phase, and the implementation of the strength dependent material model enables PLAXIS 3D-users to model small-scale tests in which the higher strength of soils under low stress is taken into account. The material model needs input calibrated towards a specific type of sand, and in this case the material model has been calibrated for Aalborg University Sand No. 1. The material model utilizes a non-linear Mohr-Coulomb criterion that when tested produces better results than the linear Mohr-Coulomb model for low stress ranges. The non-linear Mohr-Coulomb model is tested for triaxial tests and small-scale bucket foundation tests performed at Aalborg University. In future research, a non-linear elastic behaviour should be implemented, as well as examining the input parameters for the failure criterion for different types of soil. A general expression based on the soil characteristics, such as maximum void ratio, minimum void ratio and average grain size, could be developed.

One key attribute that separates the bucket foundation from traditional foundational solutions, is the fact that suction is utilized - during installation, service and decommissioning. At sea, the bucket foundation has to endure a variety of loading situations, ranging from slow moving tidal motions to impulsive loads such as freak waves or emergency stops. The bearing capacity of the bucket foundation is dependent on the loading rate, as it has a higher resistance towards impulsive loads which can be characterized as nearly undrained. To quantify the bearing capacity in the near-

undrained state, a series of tests was conducted with a bucket foundation exerted to different loading rates. The tests showed that the phenomenon does indeed exist and the bearing capacity seemed to increase with the loading rate following a power law. The results also showed that the pore pressure recorded under the bucket lid were almost constant even during high loading rates. This is somewhat contrary to the general conception which is that the suction under the lid will be eliminated through internal dissipation, which does not seem to be the case. Since these tests are important in order to prove and verify the bucket foundation during extreme loading, more tests at higher loading rates should be carried as well. Bucket foundations with different embedment ratios should be examined as well, since only a bucket foundation with  $L/D = 0.5$  was examined for this thesis.

# References

---

- Brinkgreve, Engin, and Swolfs, 2012.** R.B.J. Brinkgreve, E. Engin, and W.M. Swolfs. *Manual for PLAXIS 3D 2012*, 2012.
- Brødbæk, Møller, Sørensen, and Augustesen, 2009.** K.T. Brødbæk, M. Møller, S.P.H. Sørensen, and A.H. Augustesen. *Review of p-y relationships in cohesionless soil*. 2009.
- Det Norske Veritas, 2007.** Det Norske Veritas. *Design of Offshore Wind Turbine Structures*, 2007.
- DONG Energy, 2009.** DONG Energy. *DONG Energy Horns Reef 2*. URL: <http://www.dongenergy.com/hornsrev2/DA/Pages/Index.aspx>, 2009. Downloaded: 09-06-2013.
- Santos and Correia, 2001.** J. A. dos Santos and A. G. Correia. *Reference threshold shear strain of soil. Its application to obtain an unique strain-dependent shear modulus curve for soil*. Proceedings of the Fifteenth International Conference on Soil Mechanics and Geotechnical Engineering, Istanbul, Turkey, 27-31 August 2001. Volumes 1-3 2001 pp. 267-270., 2001.
- Foglia, Ibsen, Nielsen, and Mikalauskas, 2013.** A. Foglia, L.B. Ibsen, S.K. Nielsen, and L. Mikalauskas. *A Preliminary Study on Bucket Foundations under Transient Lateral Loading*. 2013.
- Global Wind Energy Council, 2012.** Global Wind Energy Council. *Global Wind Statistic 2012*. URL: [http://www.gwec.net/wp-content/uploads/2013/02/GWEC-PRstats-2012\\_english.pdf](http://www.gwec.net/wp-content/uploads/2013/02/GWEC-PRstats-2012_english.pdf), 2012. Downloaded: 01-06-2013.
- Ibsen and Bødker, 1994.** Lars Bo Ibsen and Lars Bødker. *Data Report 9301: Baskarp Sand No 15*, 1994.
- Ibsen, Liingaard, and Nielsen, 2008.** L.B. Ibsen, Morten Liingaard, and Søren A. Nielsen. *Bucket Foundation, a status*. 2008.
- Karstunen, 2012.** Minna Karstunen. *Hardening Soil Model - Presentation, University of Strathclyde*. URL: [https://noppa.aalto.fi/noppa/kurssi/rak-50.3149/materiaali/Rak-50\\_3149\\_1.\\_l12-\\_hardening\\_soil\\_model.pdf](https://noppa.aalto.fi/noppa/kurssi/rak-50.3149/materiaali/Rak-50_3149_1._l12-_hardening_soil_model.pdf), 2012. Downloaded: 12-11-2012.
- Knudsen, Østergaard, and Ibsen, 2013a.** Bjørn Staghøj Knudsen, Martin Underlin Østergaard, and Lars Bo Ibsen. *Small-scale Testing of Bucket Foundations in Sand*. 2013.
- Knudsen, Østergaard, Ibsen, and Clausen, 2013b.** Bjørn Staghøj Knudsen, Martin Underlin Østergaard, Lars Bo Ibsen, and Johan Clausen. *Determination of p-y Curves for Bucket Foundations in Sand Using Finite Element Modeling*. 2013.
- Krabbenhøft, 2002.** Kristian Krabbenhøft. *Basic Computational Plasticity*, 2002.
- Krabbenhøft, Clausen, and Damkilde, 2011.** Sven Krabbenhøft, Johan Clausen, and Lars Damkilde. *The Bearing Capacity of Circular Footings in Sand: Comparison between Model Tests and Numerical Simulations Based on a Nonlinear Mohr Failure Envelope*. Advances in Civil Engineering, Volume 2012, Article ID 947276, 10 pages, doi:10.1155/2012/947276, 2011.

- Larsen, 2008.** Kim André Larsen. *Static Behaviour of Bucket Foundations, vol. 1*, 2008.
- Ovesen, Fuglsang, and Bagge, 2009.** Niels Krebs Ovesen, Leif Fuglsang, and Gunnar Bagge. *Lærebog i Geoteknik*. 978-87-502-0961-4. Polyteknisk Forlag, 2009.
- Schanz, Vermeer, and Bonnier, 1999.** T. Schanz, P.A. Vermeer, and P.G. Bonnier. *The hardening soil model: Formulation and verification*. Beyond 2000 in Computational Geotechnics - 10 years of PLAXIS International., 1999.
- Sjelmo, Mikalauskas, Ibsen, and Foglia, 2012.** Å. Sjelmo, L. Mikalauskas, L.B. Ibsen, and A. Foglia. *Soil-Structure Interaction in Cohesionless Soils due to Monotonic Loading*. 2012.

**Part II**

**Appendices**



# A Convergence and Test of Physical Domain in PLAXIS 3D

The PLAXIS 3D models used for the  $p - y$  curve determination are tested for both convergence with respects to the mesh quality and sufficient physical domain size of the model. The method and results of this will be explained in the following. Since the mesh quality affects the physical domain requirements and vice versa, the procedure of investigating both is iterative.

## A.1 Element types

PLAXIS 3D does not offer any possibilities as far as choosing the type of element used in the model. However, an overview of the applied element types is given in the following based on Brinkgreve et al. [2012].

### A.1.1 Soil element

To discretize the soil volumes a 10-noded tetrahedral element is used. This type of element has 10 nodes and 4 Gauss points (integration points). It has three degrees of freedom per node corresponding to a translation in each of the three coordinate directions,  $u_x$ ,  $u_y$  and  $u_z$ . The shape functions for this type of elements are of second order. Figure A.1 shows the 10-noded tetrahedral element.

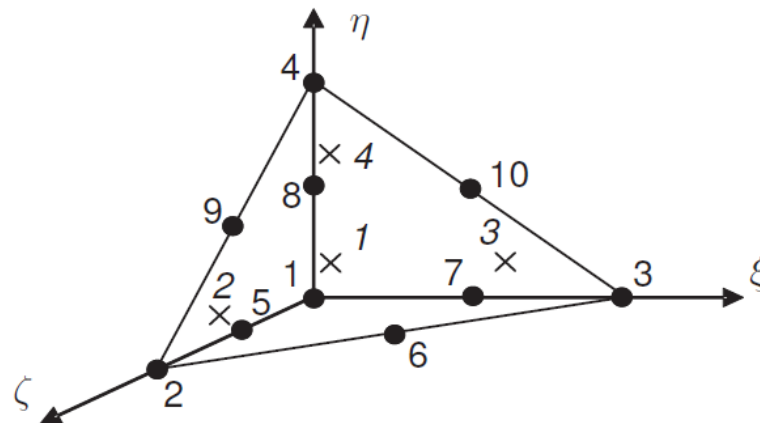


Figure A.1. 10-noded tetrahedral element with 10 nodes (dots) and 4 Gauss points (crosses).

### A.1.2 Plate element

For the plate elements, a 2D 6-noded triangular element is used. It has 6 nodes and 3 Gauss points. Each node has six degrees of freedom corresponding to three translational degrees of freedom ( $u_x$ ,  $u_y$  and  $u_z$ ) and three rotational degrees of freedom ( $\phi_x$ ,  $\phi_y$  and  $\phi_z$ ). The shape functions are of second order. Figure A.2 shows the 6-noded triangular element.

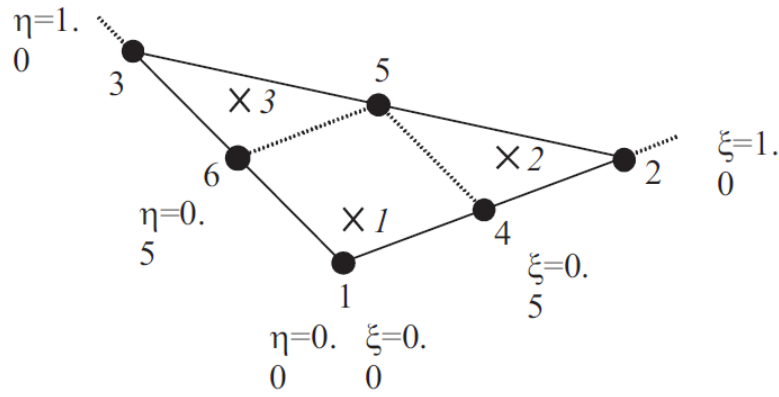


Figure A.2. 6-noded triangular element with 6 nodes (dots) and 3 Gauss points (crosses).

### A.1.3 Interface element

The elements used for the interfaces between soil and plate is in principle identical to the 6-noded triangular element used for the plates in the model. The difference is that the interface element consists of 8 pairs of nodes with an internal distance of 0. Each node has three translational degrees of freedom ( $u_x$ ,  $u_y$  and  $u_z$ ). The degrees of freedom for two nodes in a pair is not the same meaning that this element can have differential displacement between nodes in pairs. Figure A.3 shows the 16-noded triangular element.

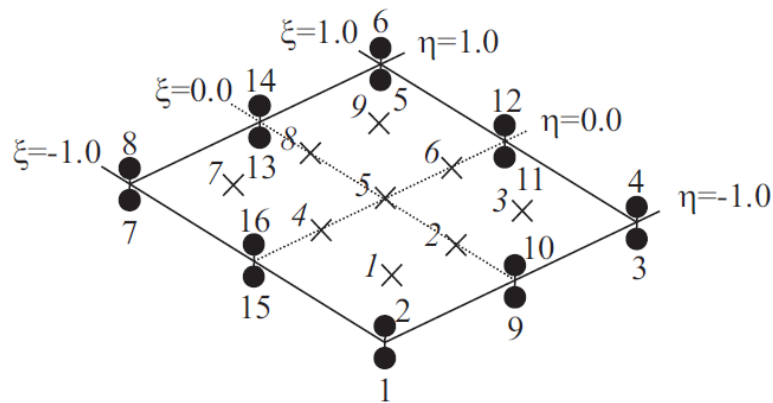


Figure A.3. 16-noded triangular element with 8 nodepairs (dots) and 9 Gauss points (crosses).

## A.2 Convergence analysis

In order to ensure that the mesh quality does not influence the results of the finite element analysis (FEA), convergence analyses are carried out. Since a total of 18 different models are used, with varying geometry and soil parameters, the required mesh quality will be different from model to model. This could lead to the conclusion that a convergence analysis of every single model is necessary, however some simplifications are made. First of all, the geometry only yields six different models, which with three sets of material properties gives a total of 18 models. If the skirt-length variation is taken out, by only examining the buckets with  $L = D$  since the failure mechanism will be largest, this results in 9 unique models.

The deciding factor in the material models is the effective friction angle, with values of  $30^\circ$  to  $40^\circ$ . A higher friction angle of the soil will cause the failure mechanism to expand further and at the same time increase the complexity of solving the numerical system. Therefore it can be assumed that the highest friction angle will require both the highest mesh quality and the largest physical domain. If only the largest friction angle is investigated, only 3 models remain to be tested. These three models will be representative, and on the conservative side, for the buckets with respectively 10, 15 and 20 meters in diameter.

The soil domain is divided into two main sections; a proximity volume and a surrounding volume, cf. figure A.4. In the proximity volume the mesh is refined, since large stress gradients are expected in this area. The diameter of the half-cylinder, i.e. the proximity volume, is three times the diameter of the bucket and the height is twice the length of the skirt. In the convergence analysis, the mesh of the soil in the proximity volume is changed, and the result is tracked.

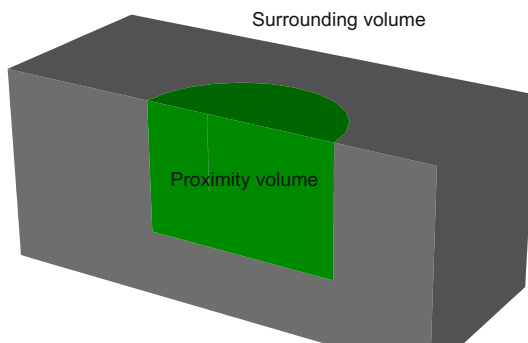


Figure A.4. Division of domain.

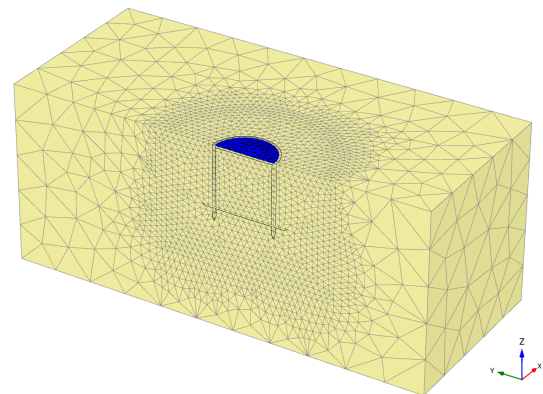


Figure A.5. Example of mesh.

The meshing facility in PLAXIS is highly automated, leaving only a few parameters to control. Generally the element size is determined relative to the domain size, with a choice of coarseness of the overall mesh varying from *very coarse* to *very fine*. The models are meshed by choosing an overall mesh density of *coarse* and then refining the proximity volume relative to this. The refinement is applied by choosing a mesh refinement factor, which if equal to 1 gives the same element size as the overall and half the size if equal to 0.5.

The convergency analysis is done by applying a prescribed displacement to the bucket. The reaction force towards this displacement is tracked in the analysis. When the model is converged this value should not vary for an increasing number of elements in the mesh. The result from the three analyses are seen in the next sections.

### A.2.1 Convergence of Model 6

This model represents the diameter of 10 m. The convergence graph is seen in figure A.6.

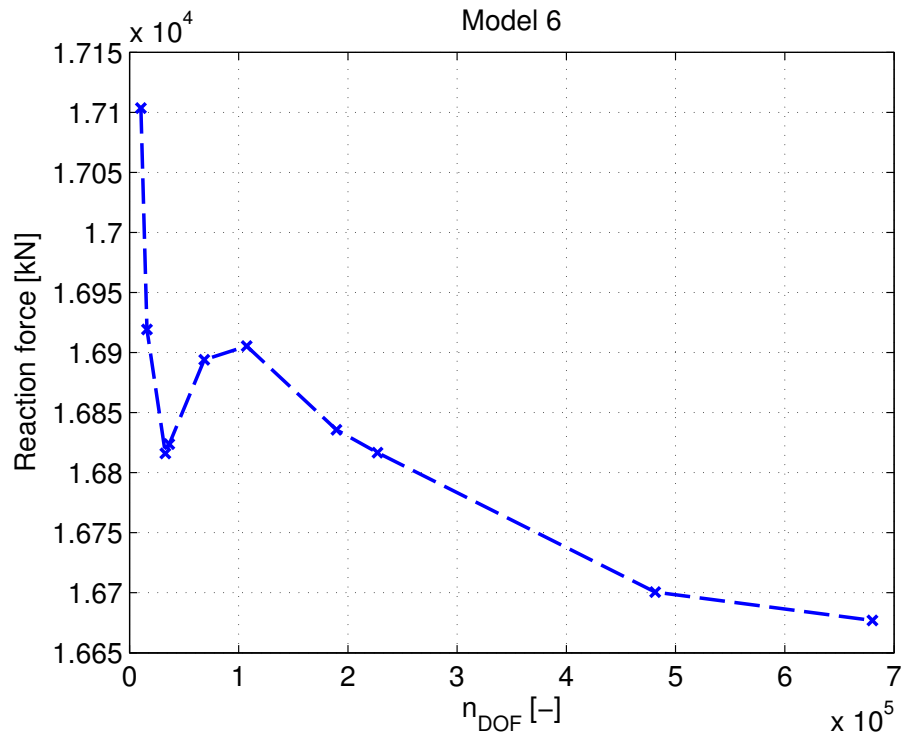


Figure A.6. Division of domain.

The following table contains the values from the graph.

Fineness factor	$n_{DOF}$	$F_y$
1.000	10545	17103.520
0.800	16038	16919.244
0.500	32805	16815.987
0.400	36516	16823.753
0.300	68421	16894.040
0.250	107268	16905.334
0.200	189417	16835.700
0.175	277029	16816.560
<b>0.150</b>	<b>481251</b>	<b>16700.630</b>
0.125	680268	16677.000

Table A.1. Model 6 - convergence results. Fineness factor in proximity volume.

The model is considered to be converged at a fineness in the proximity volume of 0.150, even though the reaction value still changes as the relative fineness increases. The change is however small enough to be neglectable.

## A.2.2 Convergence of Model 12

This model represents the diameter of 15 m. The convergence graph is seen in figure A.7.

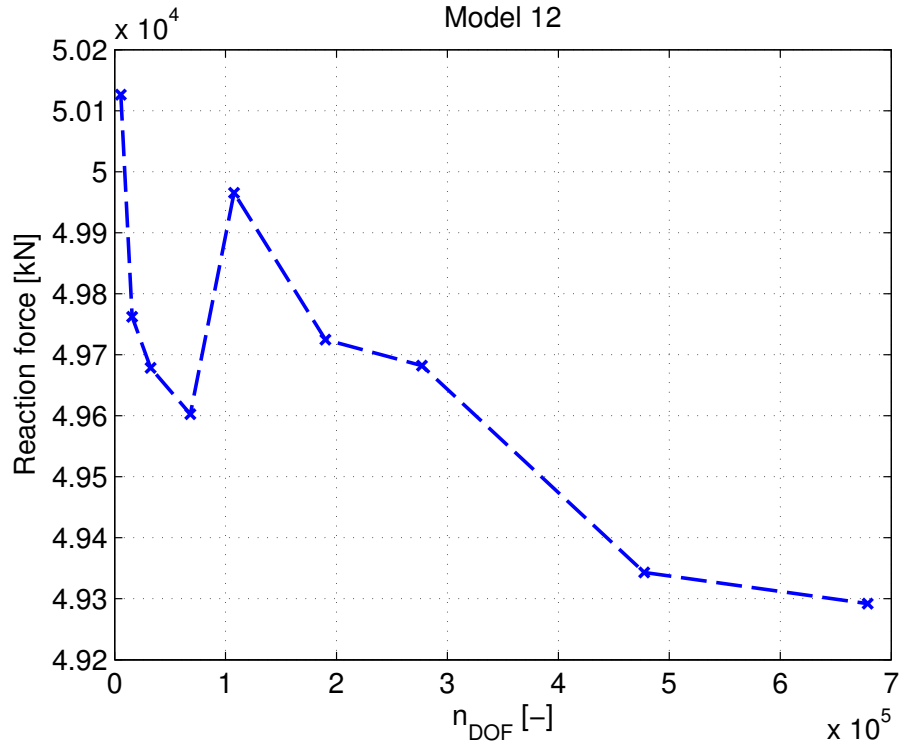


Figure A.7. Division of domain.

The following table contains the values from the graph.

Fineness factor [-]	$n_{\text{DOF}}$	$F_y$ [kN]
1.000	5586	50126.183
0.800	15906	49762.100
0.500	32541	49678.350
0.300	68262	49602.777
0.250	107637	49965.248
0.200	190026	49724.805
0.175	277086	49682.053
<b>0.150</b>	<b>477423</b>	<b>49343.000</b>
0.125	678852	49292.000

Table A.2. Model 12 - convergence results. Fineness factor in proximity volume.

As Model 6, Model 12 is considered to be converged at a fineness in the proximity volume of 0.150.

### A.2.3 Convergence of Model 18

This model represents the diameter of 20 m. The convergence graph is seen in figure A.8.

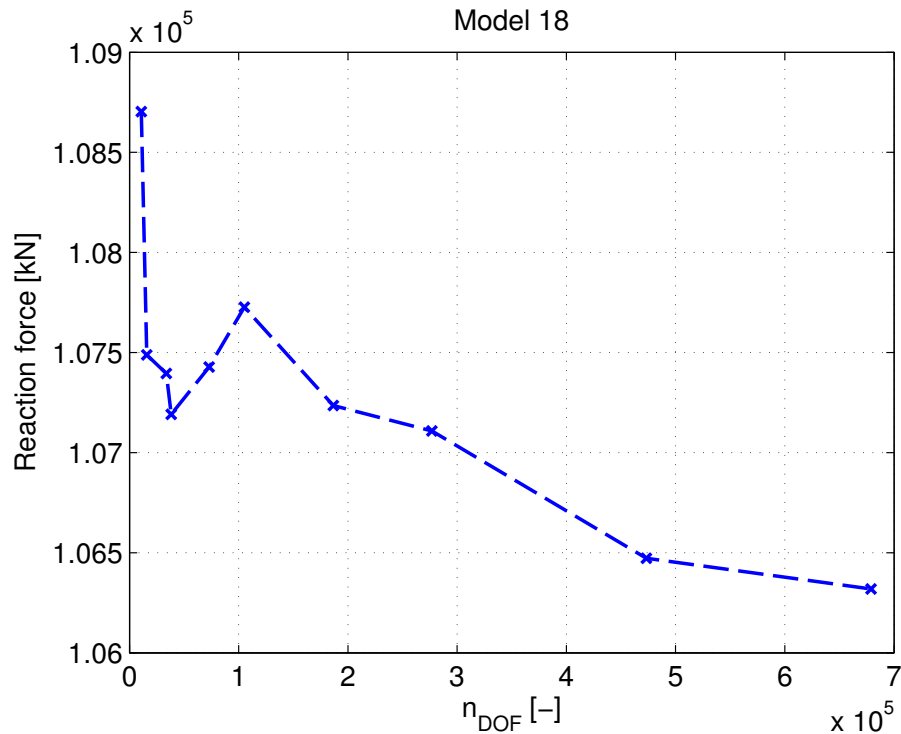


Figure A.8. Division of domain.

The following table contains the values from the graph.

Fineness factor [-]	$n_{DOF}$	$F_y$ [kN]
1.000	10776	108703.821
0.800	15828	107488.725
0.500	33705	107395.621
0.400	38286	107191.079
0.300	72921	107427.351
0.250	105186	107727.049
0.200	186555	107235.105
0.175	276795	107107.880
<b>0.150</b>	<b>473193</b>	<b>106472.000</b>
0.125	678882	106319.000

Table A.3. Model 18 - convergence results. Fineness factor in proximity volume.

As the previous models, Model 18 is considered to be converged at a fineness in the proximity volume of 0.150.

As a conclusion a fineness factor of 0.150 has shown to be sufficient for all three models. The fineness factor of 0.150 in the proximity volume will therefore be used for all the models in the p-y investigation.

### A.3 Model Domain

The boundaries of the physical domain should be far enough away from the bucket to not have any influence on the results, however the larger the domain the more degrees of freedom the model will have, which directly increases the calculation time. A general rule of thumb is implemented, stating that at the boundaries a maximum stress increment of 10% of the stress increment right next to the bucket should be present. This is tested by doing horizontal cuts in the soil volume and comparing contour curves of the stress at respectively a nil-step, i.e. a step with no external loads or displacements, and the final load-step. Examples of such two horizontal plots are shown in figure A.9 and A.10.

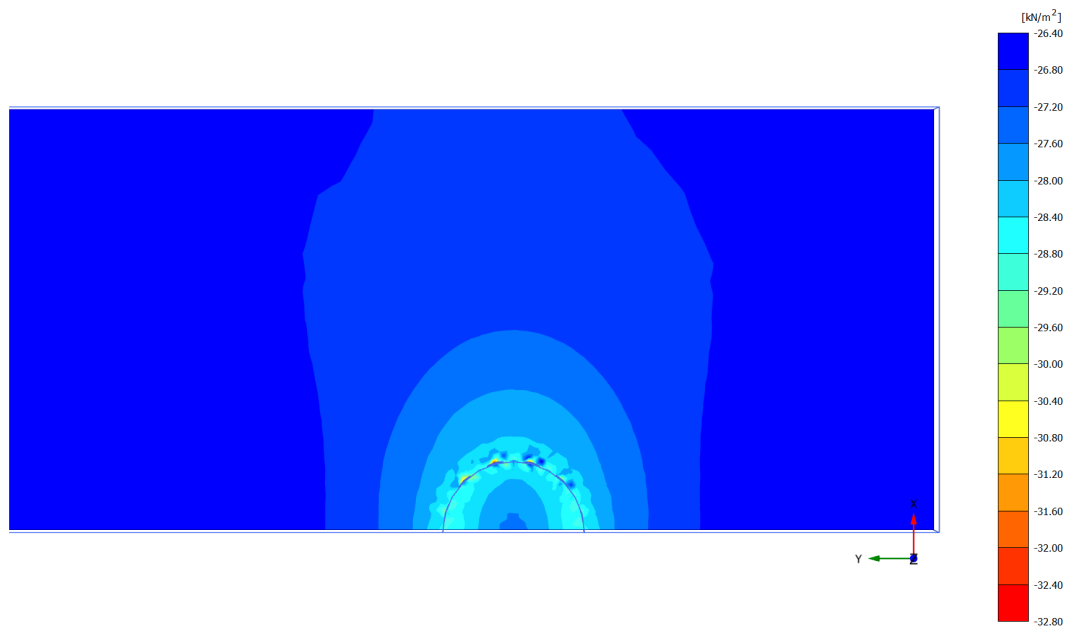


Figure A.9.  $\sigma'_{yy}$  in a nil-step. Horizontal cut at  $z = -7.5 = L/2$ .

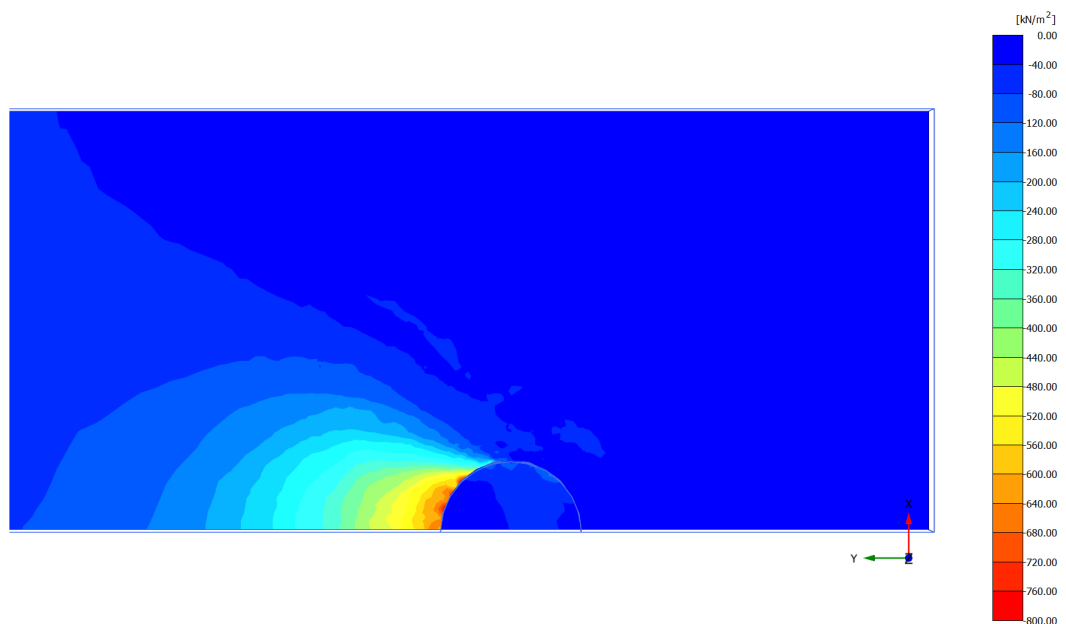


Figure A.10.  $\sigma'_{yy}$  in a load-step. Horizontal cut at  $z = -7.5 = L/2$ .



# B Additional p-y Results

This appendix contains the results of all 18 models used in the determination of new  $p - y$  curves for the bucket foundation in sand in the drained condition. The physical properties of each model can be seen in the figure header.

The results are shown with the best fit of the filtered data in the second figure of each model. Appendix C - *Mathematical Formulation of the New p-y Curves* contains figures with the general mathematical model.

## B.1 Model 1

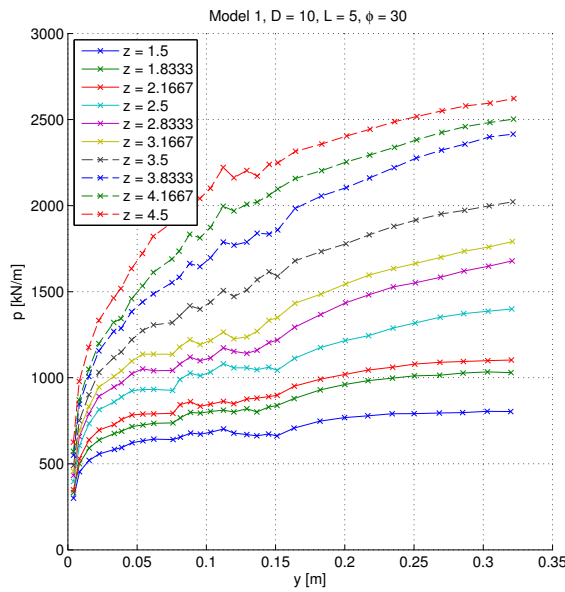


Figure B.1.  $p - y$  data

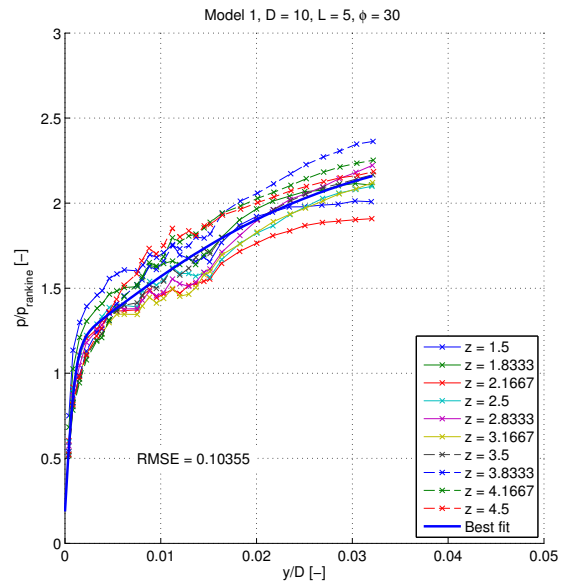


Figure B.2.  $\frac{p}{p_R} - \frac{y}{D}$  data

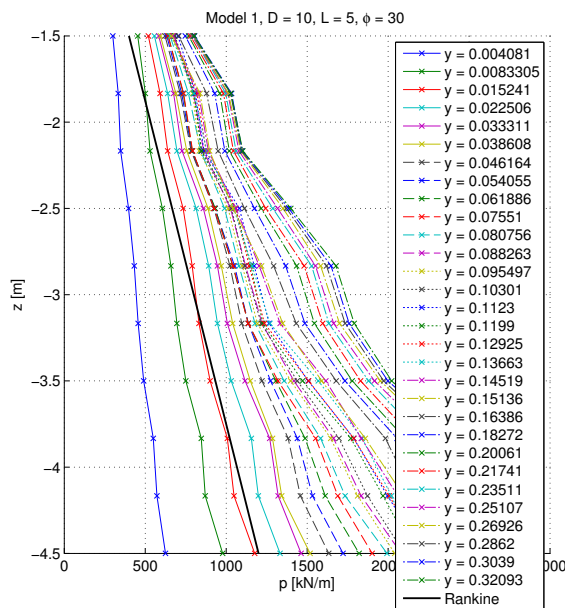


Figure B.3.  $p - z$  data

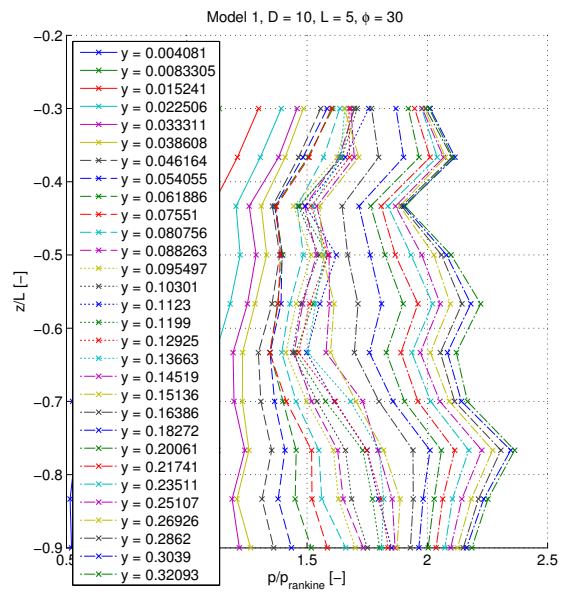


Figure B.4.  $\frac{p}{p_R} - \frac{z}{L}$  data

## B.2 Model 2

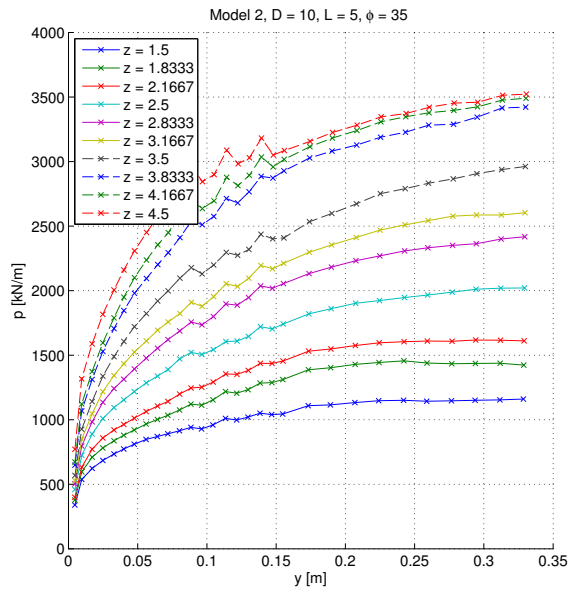


Figure B.5.  $p - y$  data

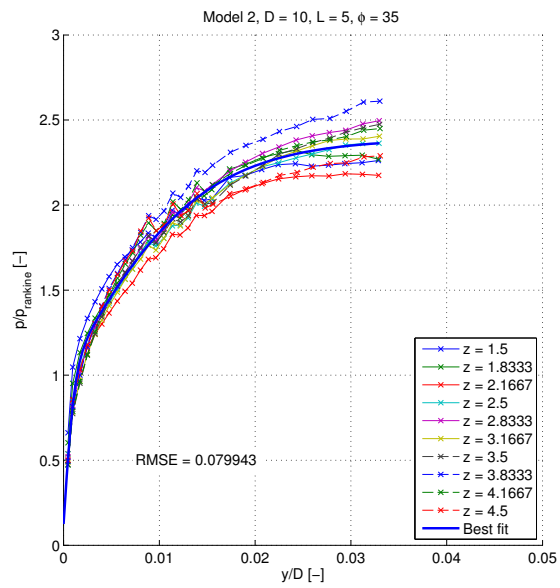


Figure B.6.  $\frac{p}{p_R} - \frac{y}{D}$  data

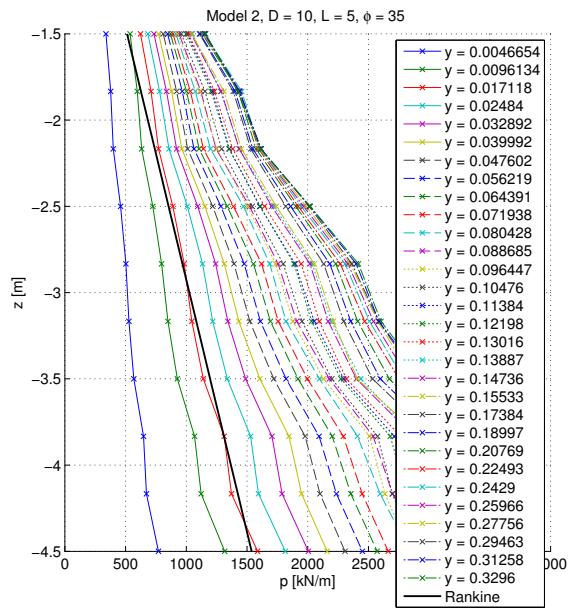


Figure B.7.  $p - z$  data

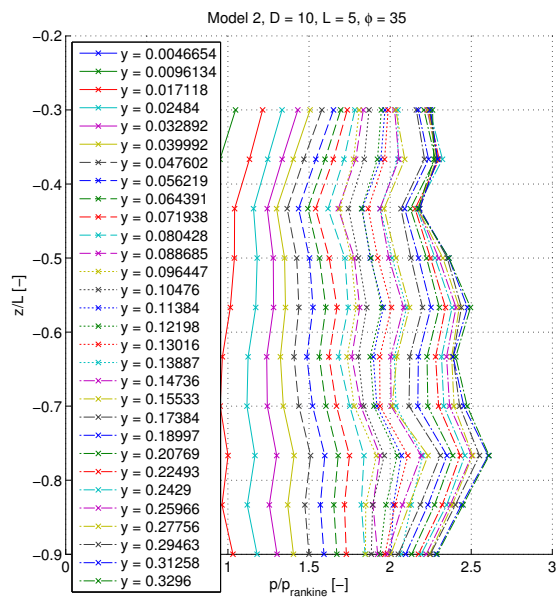


Figure B.8.  $\frac{p}{p_R} - \frac{z}{L}$  data

### B.3 Model 3

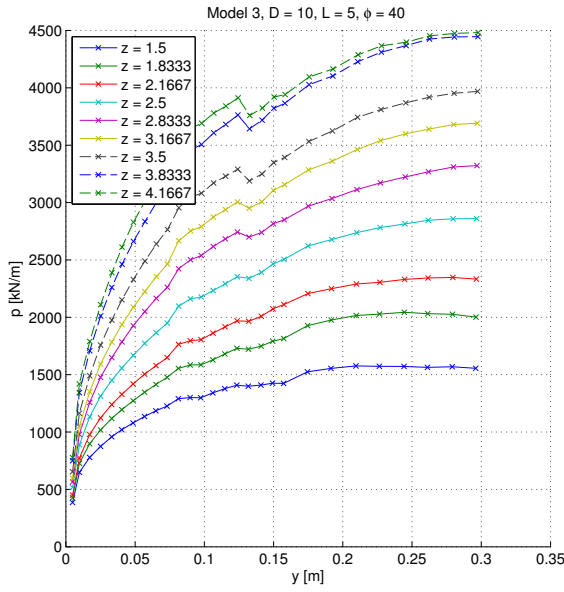


Figure B.9.  $p - y$  data

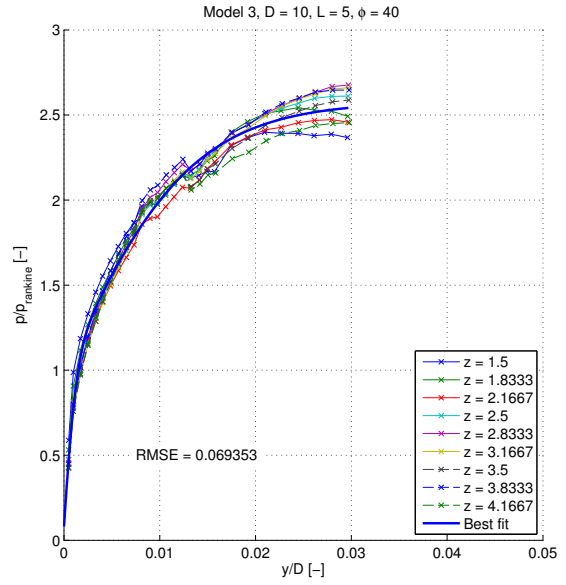


Figure B.10.  $\frac{p}{p_R} - \frac{y}{D}$  data

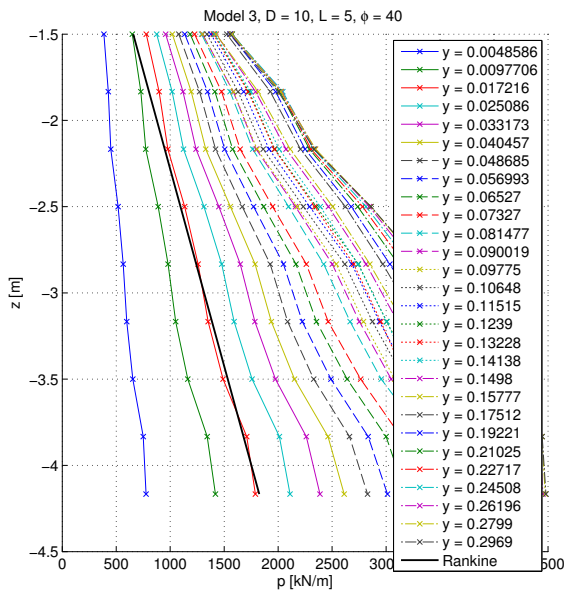


Figure B.11.  $p - z$  data

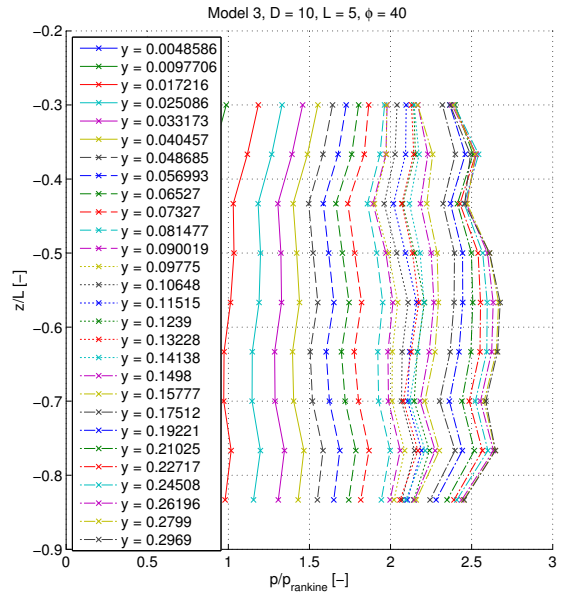


Figure B.12.  $\frac{p}{p_R} - \frac{z}{L}$  data

## B.4 Model 4

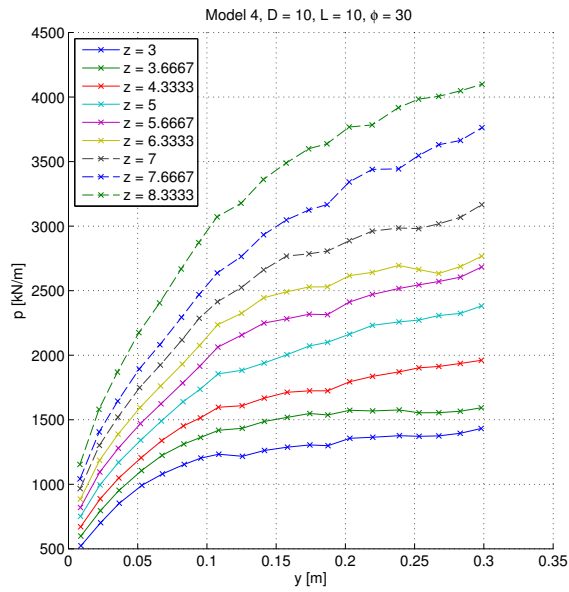


Figure B.13.  $p - y$  data

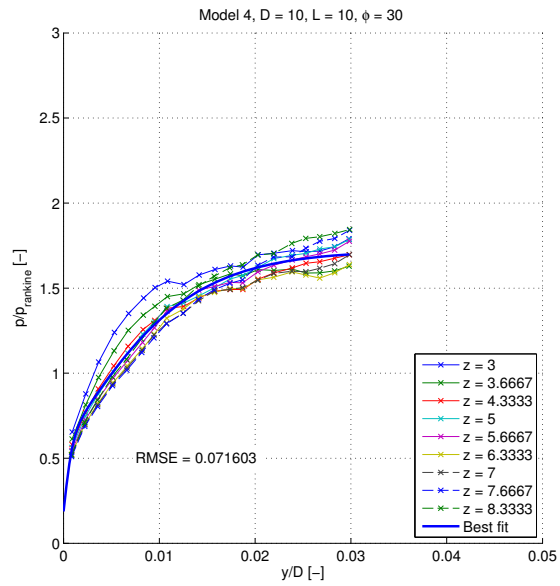


Figure B.14.  $\frac{p}{p_R} - \frac{y}{D}$  data

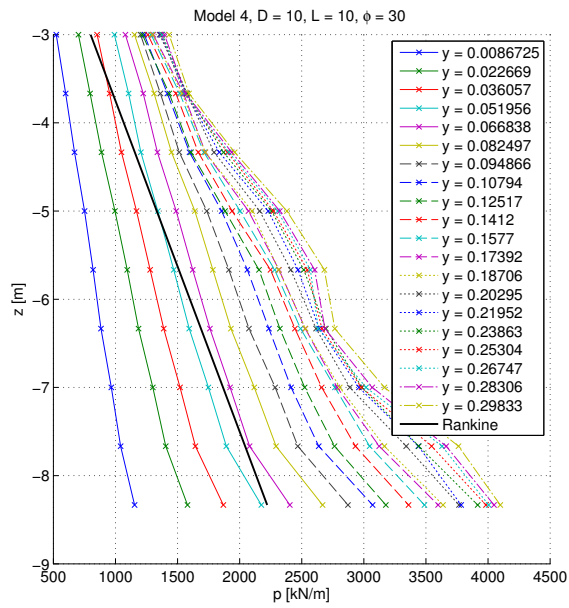


Figure B.15.  $p - z$  data

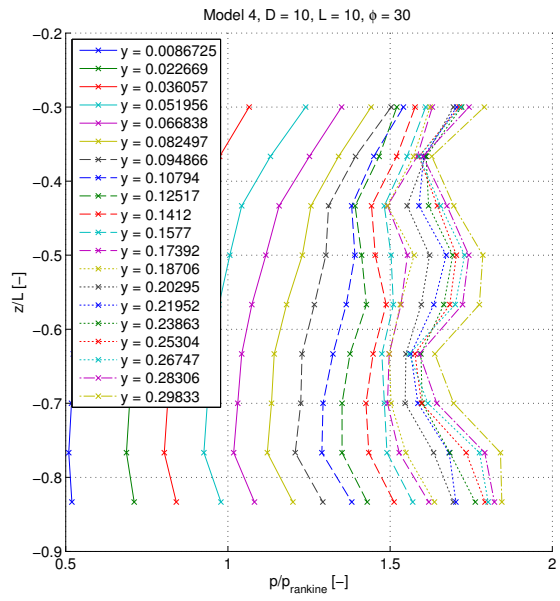


Figure B.16.  $\frac{p}{p_R} - \frac{z}{L}$  data

## B.5 Model 5

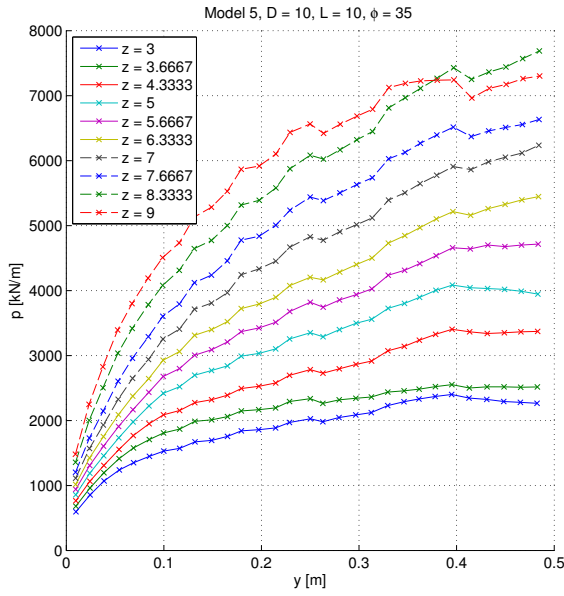


Figure B.17.  $p - y$  data

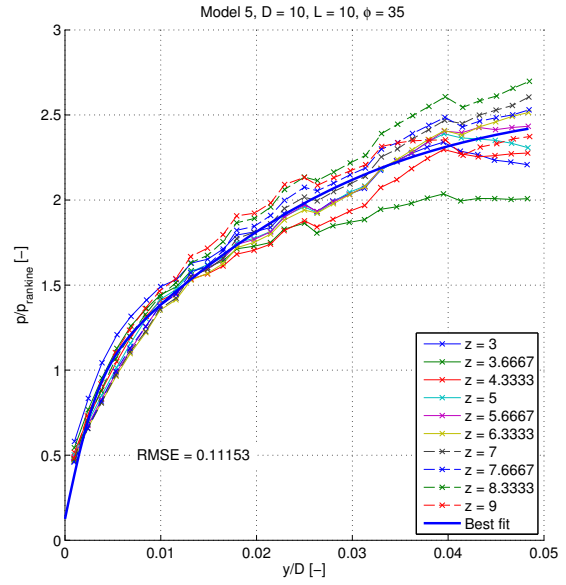


Figure B.18.  $\frac{p}{p_R} - \frac{y}{D}$  data

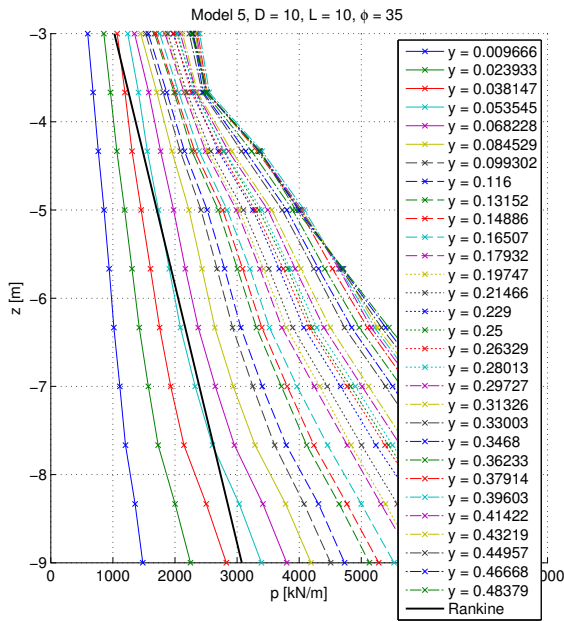


Figure B.19.  $p - z$  data

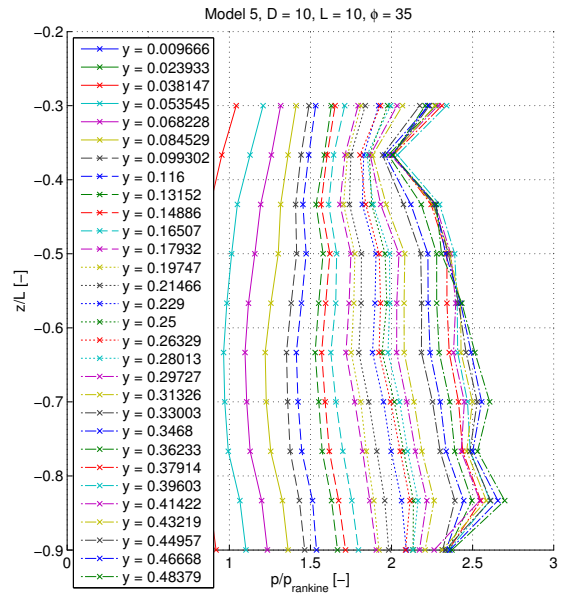


Figure B.20.  $\frac{p}{p_R} - \frac{z}{L}$  data

## B.6 Model 6

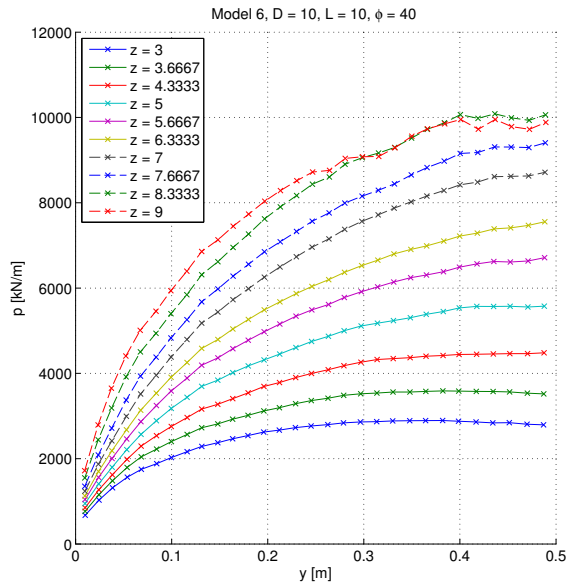


Figure B.21.  $p - y$  data

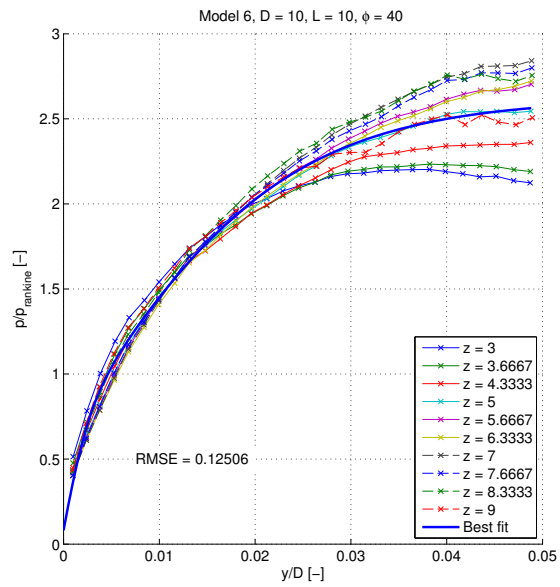


Figure B.22.  $\frac{p}{p_R} - \frac{y}{D}$  data

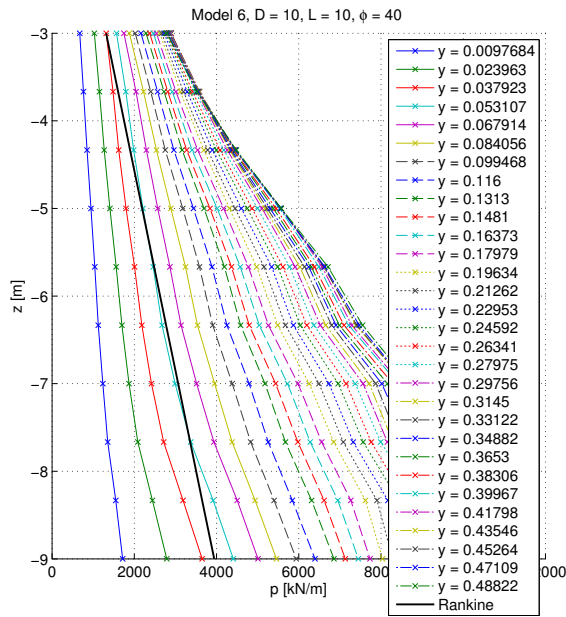


Figure B.23.  $p - z$  data

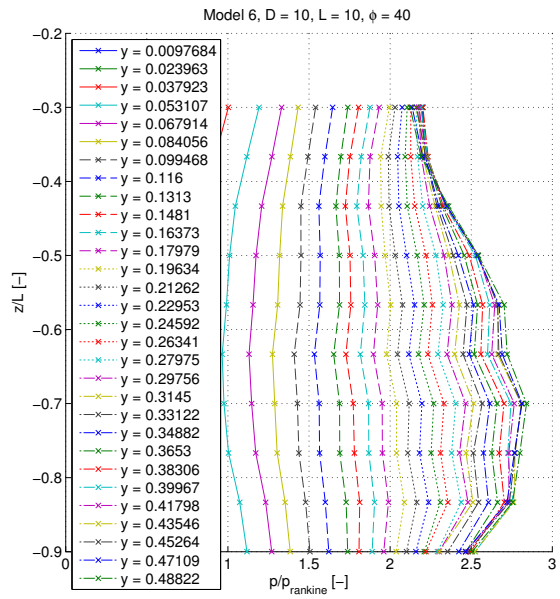


Figure B.24.  $\frac{p}{p_R} - \frac{z}{L}$  data

## B.7 Model 7

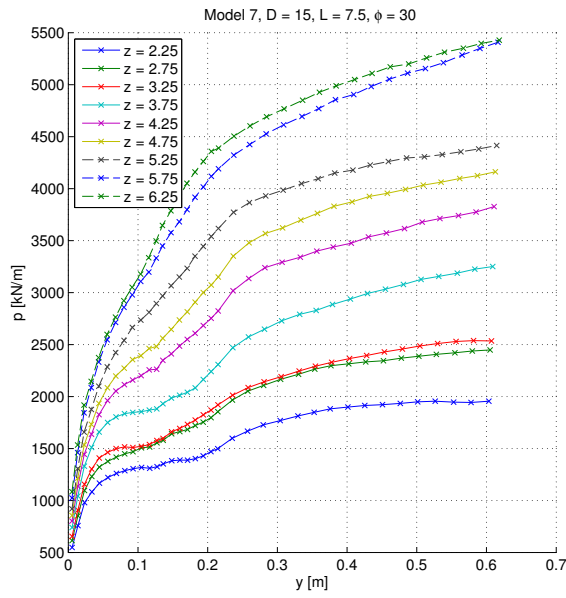


Figure B.25.  $p - y$  data

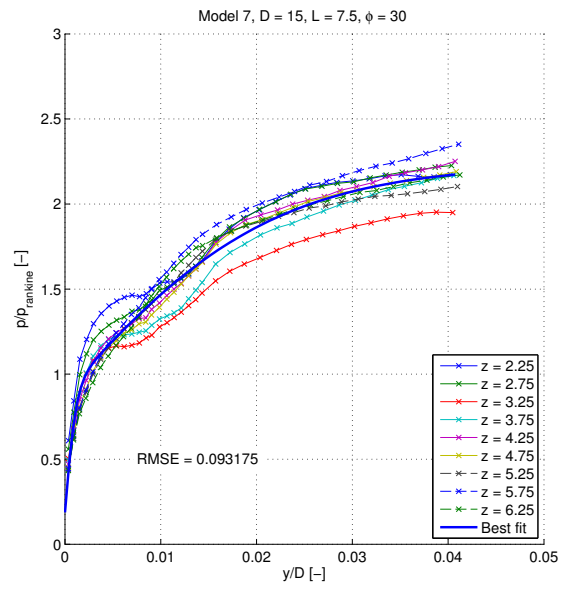


Figure B.26.  $\frac{p}{p_R} - \frac{y}{D}$  data

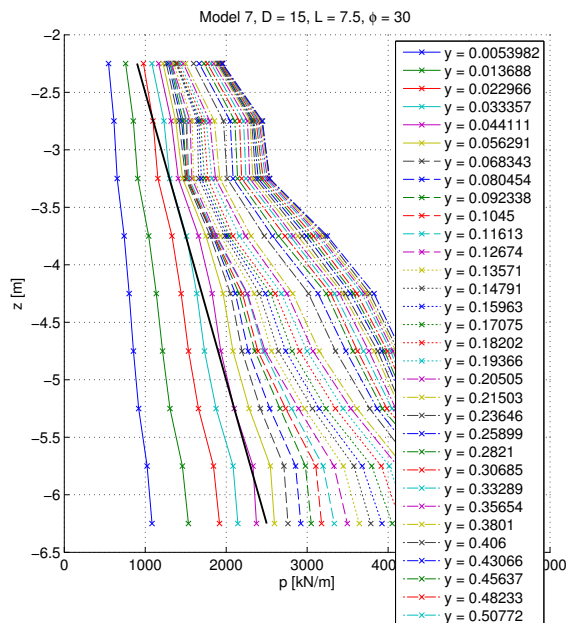


Figure B.27.  $p - z$  data

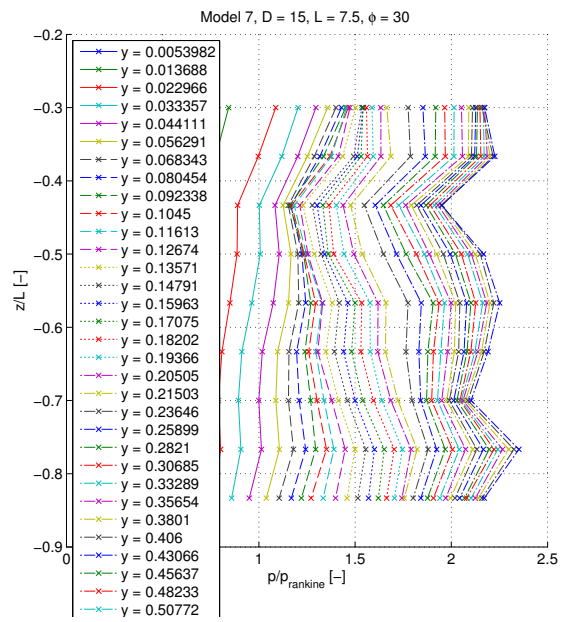


Figure B.28.  $\frac{p}{p_R} - \frac{z}{L}$  data

## B.8 Model 8

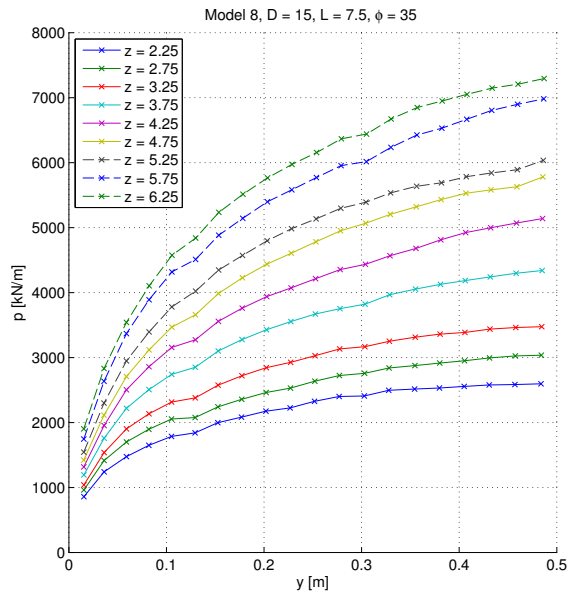


Figure B.29.  $p - y$  data

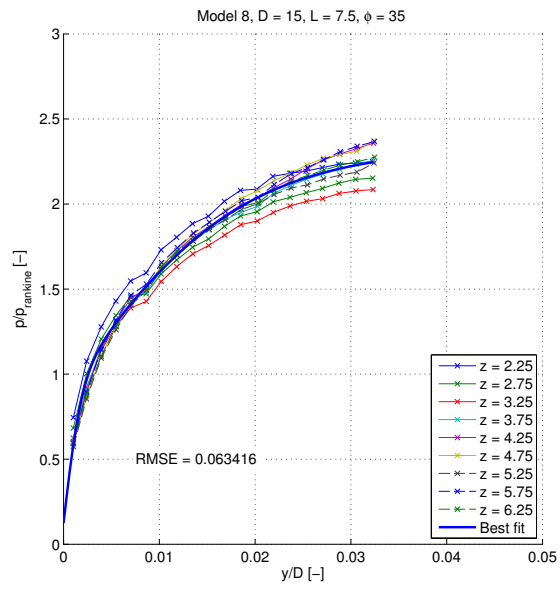


Figure B.30.  $\frac{p}{p_R} - \frac{y}{D}$  data

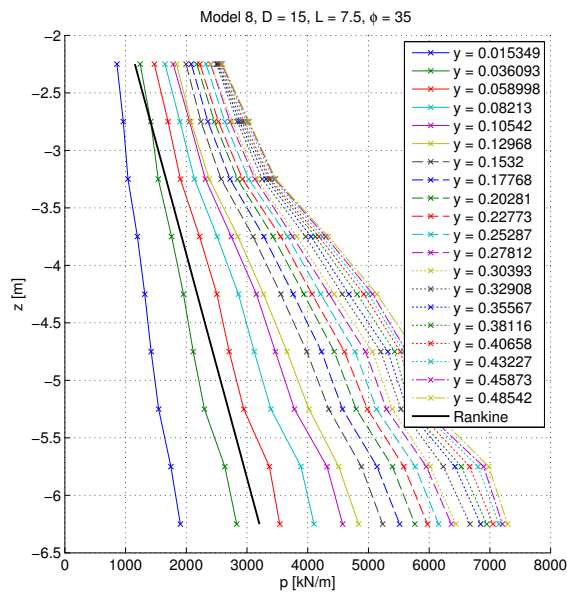


Figure B.31.  $p - z$  data

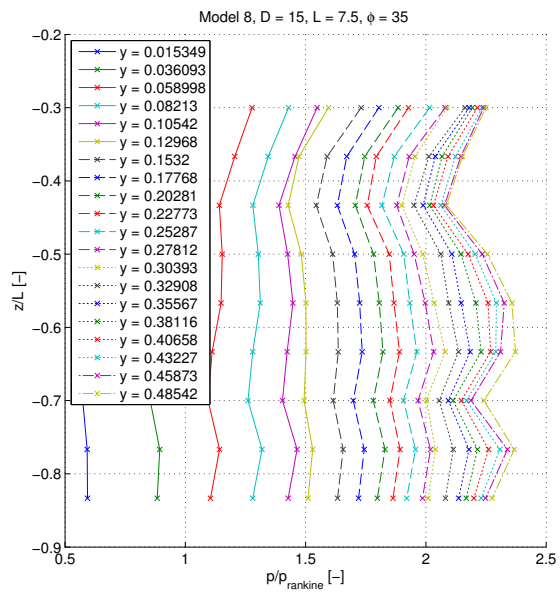


Figure B.32.  $\frac{p}{p_R} - \frac{z}{L}$  data

## B.9 Model 9

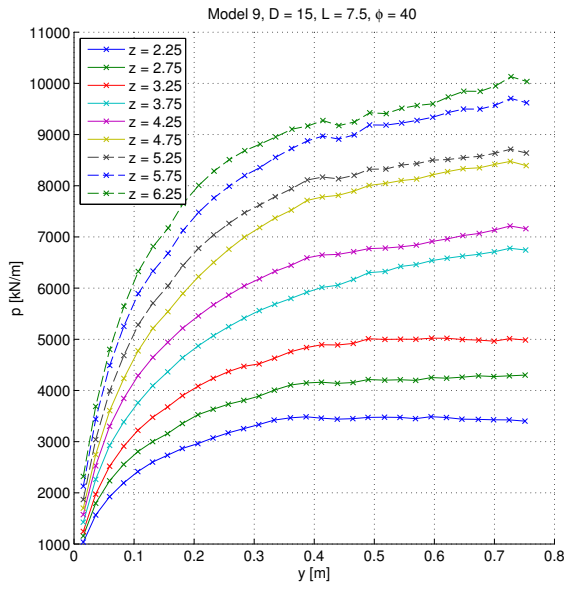


Figure B.33.  $p - y$  data

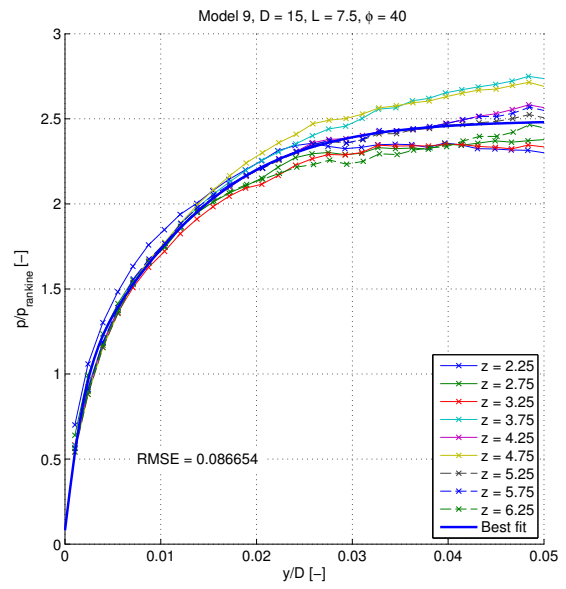


Figure B.34.  $\frac{p}{p_R} - \frac{y}{D}$  data

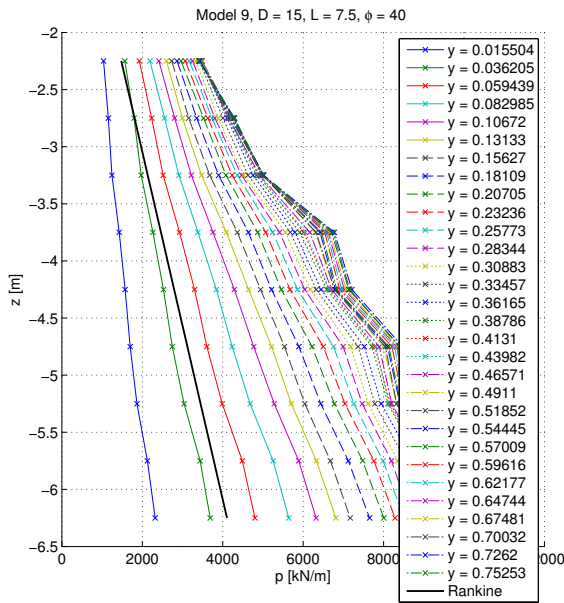


Figure B.35.  $p - z$  data

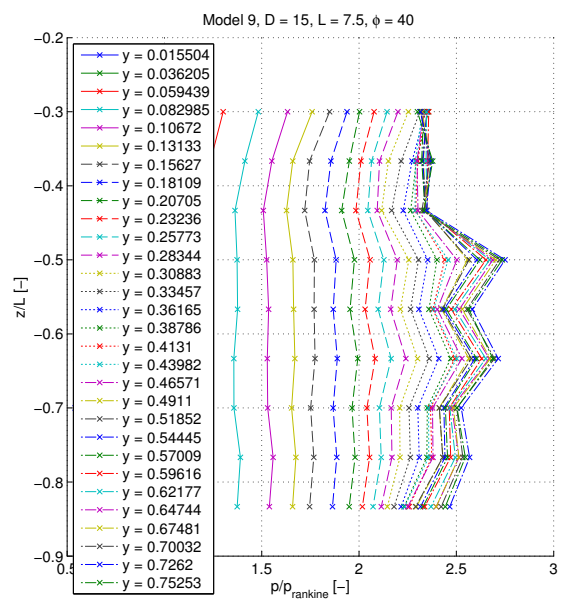


Figure B.36.  $\frac{p}{p_R} - \frac{z}{L}$  data

## B.10 Model 10

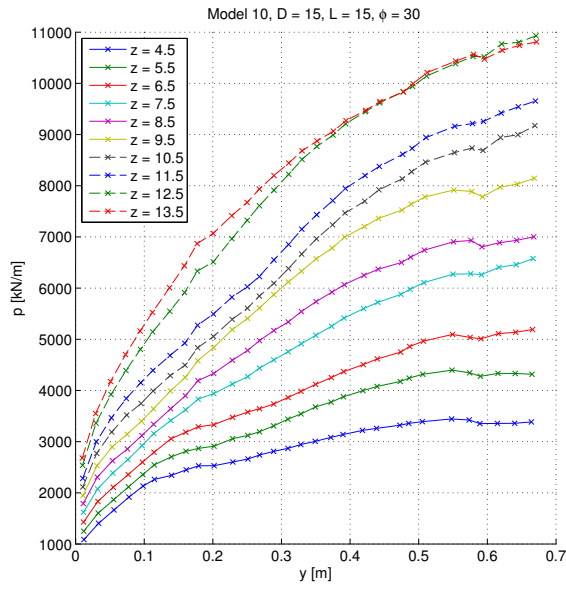


Figure B.37.  $p - y$  data

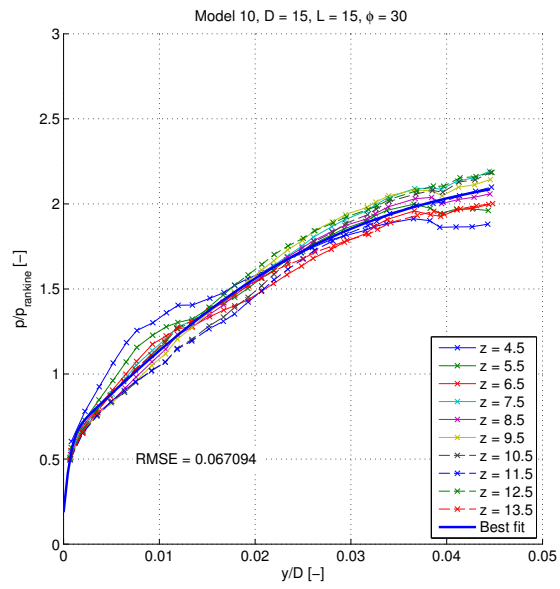


Figure B.38.  $\frac{p}{p_R} - \frac{y}{D}$  data

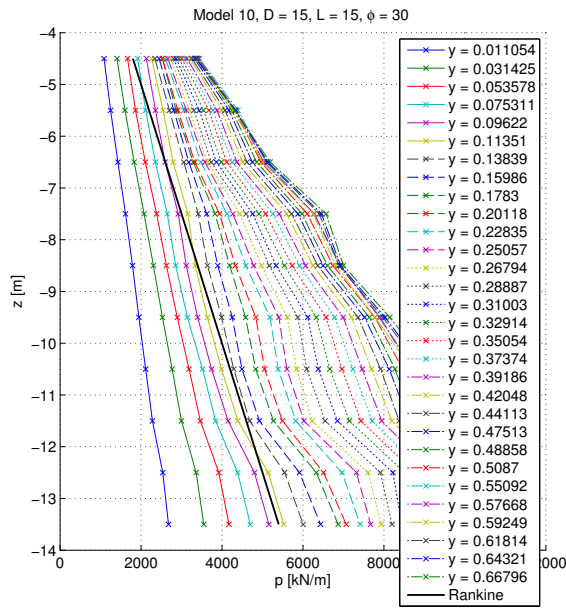


Figure B.39.  $p - z$  data

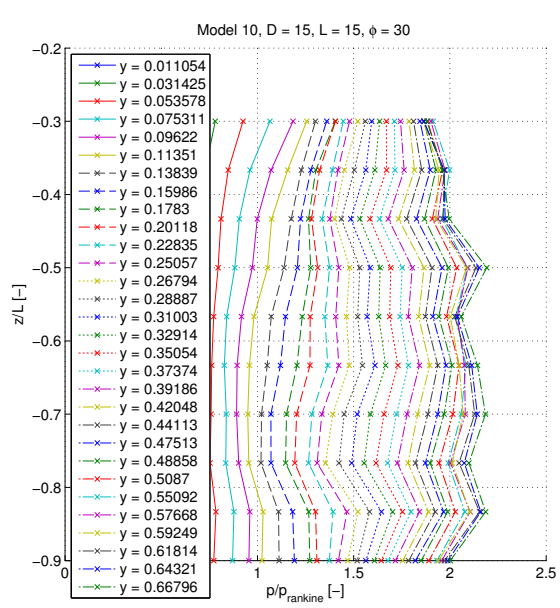


Figure B.40.  $\frac{p}{p_R} - \frac{z}{L}$  data

## B.11 Model 11

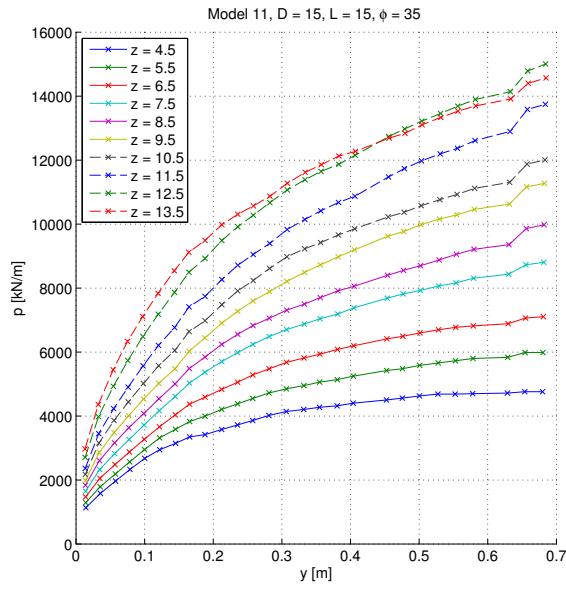


Figure B.41.  $p - y$  data

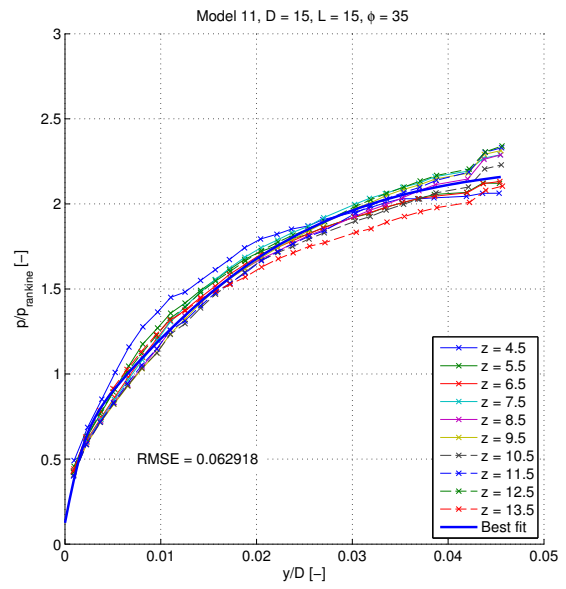


Figure B.42.  $\frac{p}{p_R} - \frac{y}{D}$  data

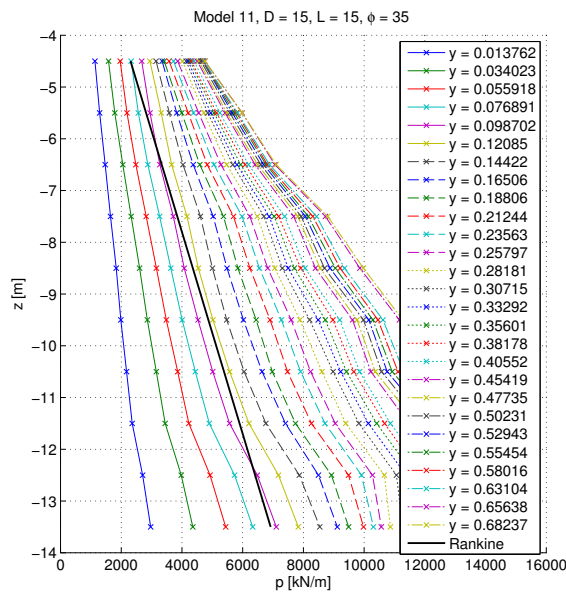


Figure B.43.  $p - z$  data

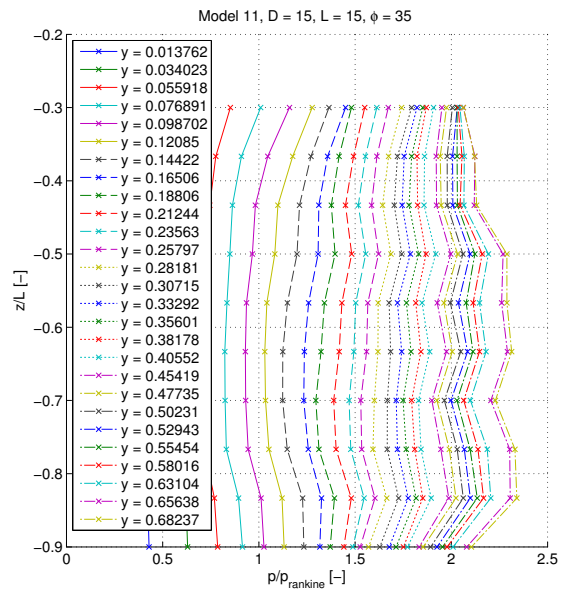


Figure B.44.  $\frac{p}{p_R} - \frac{z}{L}$  data

## B.12 Model 12

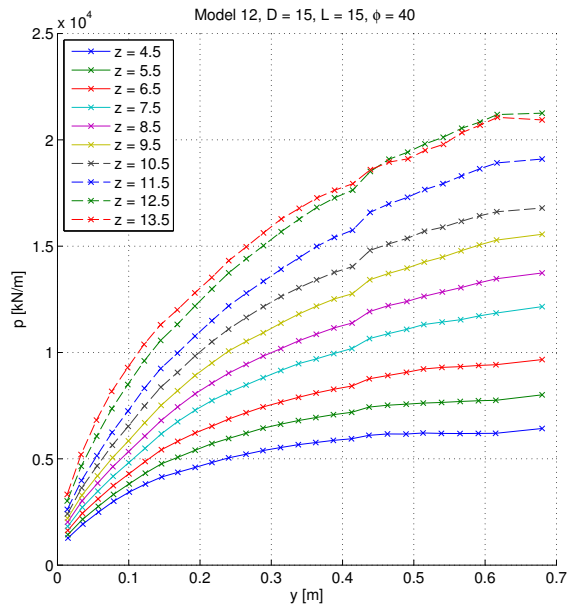


Figure B.45.  $p - y$  data

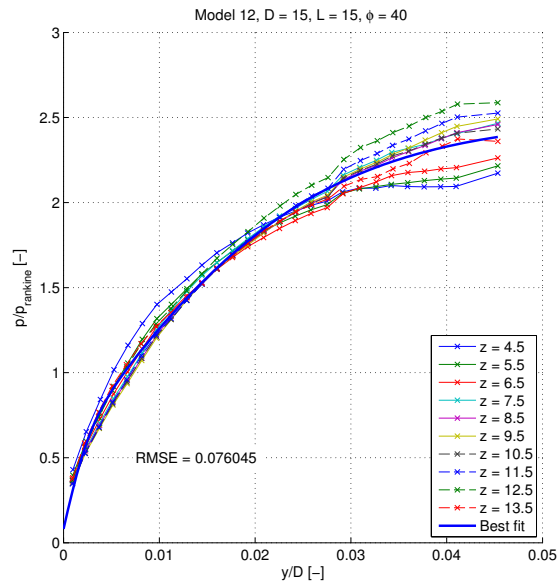


Figure B.46.  $\frac{p}{p_R} - \frac{y}{D}$  data

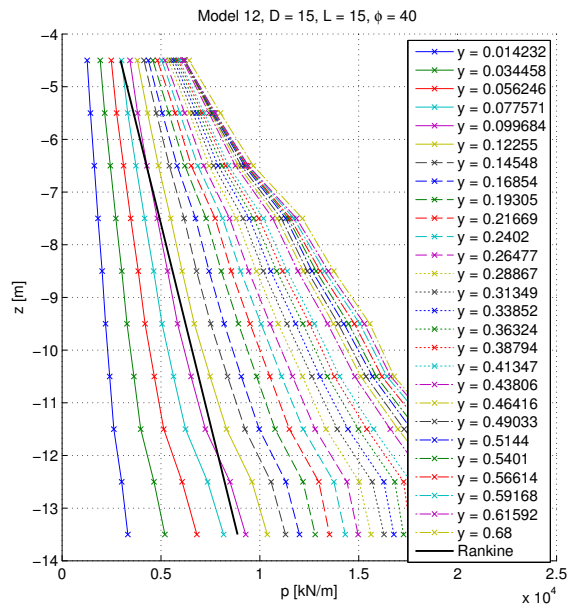


Figure B.47.  $p - z$  data

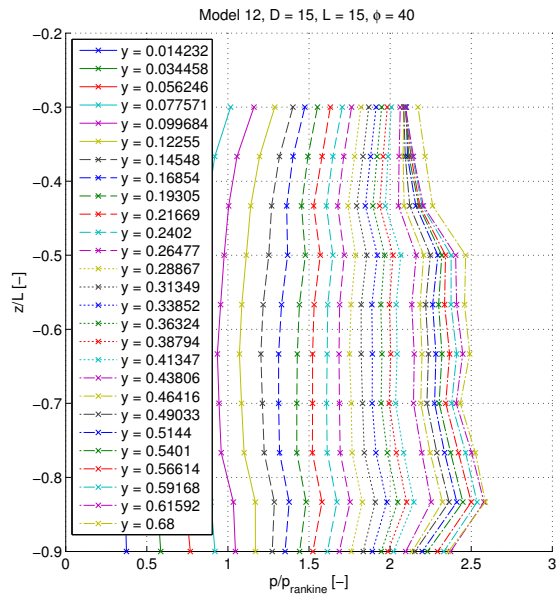


Figure B.48.  $\frac{p}{p_R} - \frac{z}{L}$  data

## B.13 Model 13

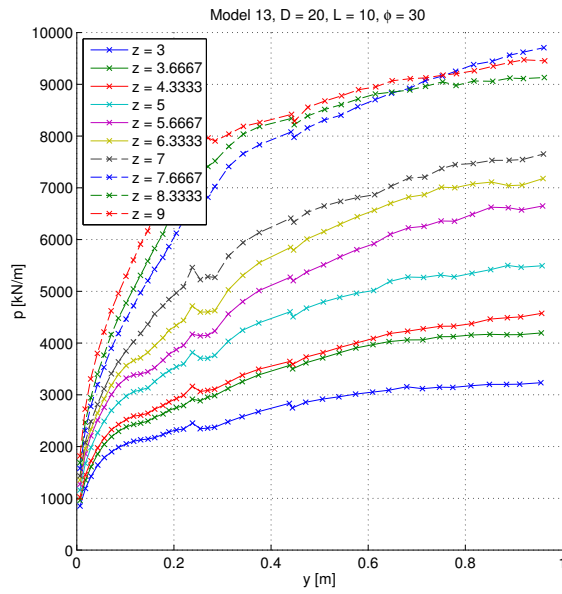


Figure B.49.  $p - y$  data

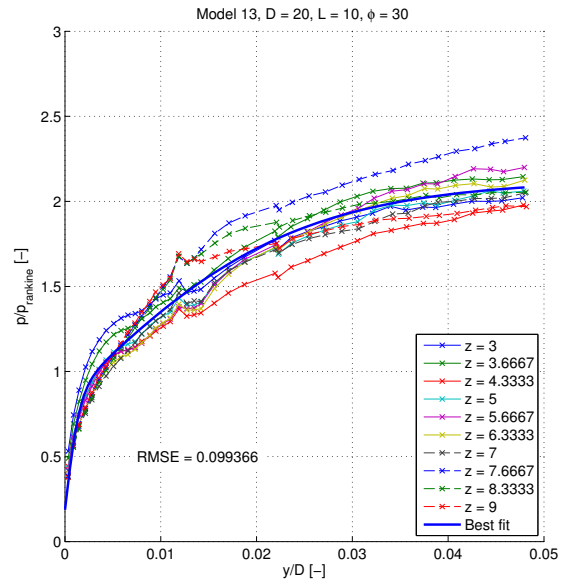


Figure B.50.  $\frac{p}{p_R} - \frac{y}{D}$  data

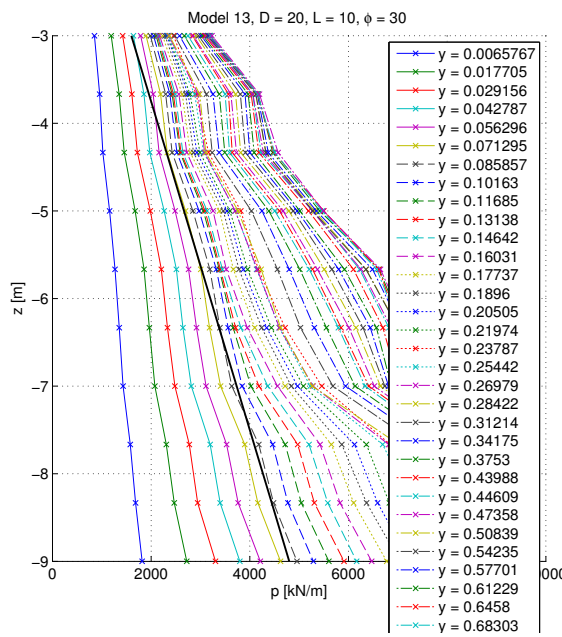


Figure B.51.  $p - z$  data

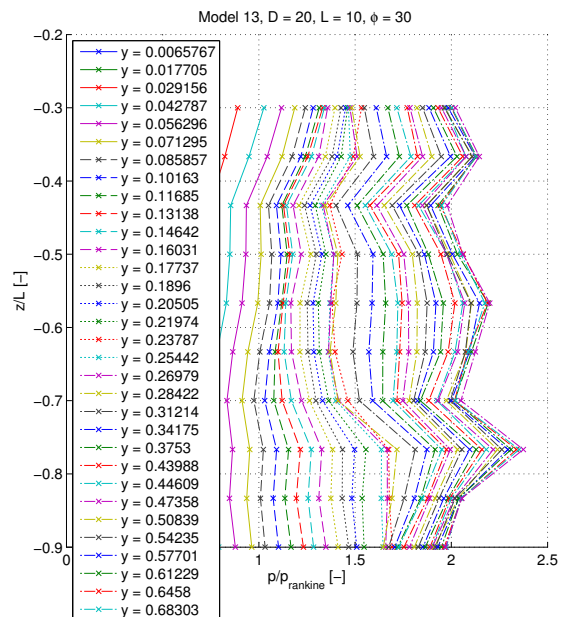


Figure B.52.  $\frac{p}{p_R} - \frac{z}{L}$  data

## B.14 Model 14

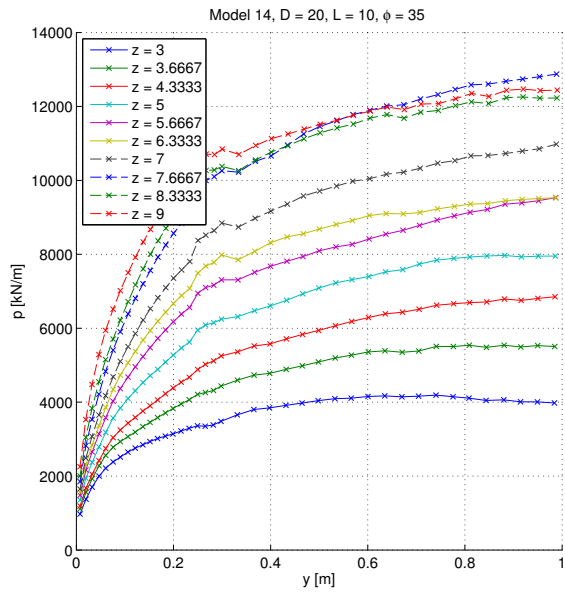


Figure B.53.  $p - y$  data

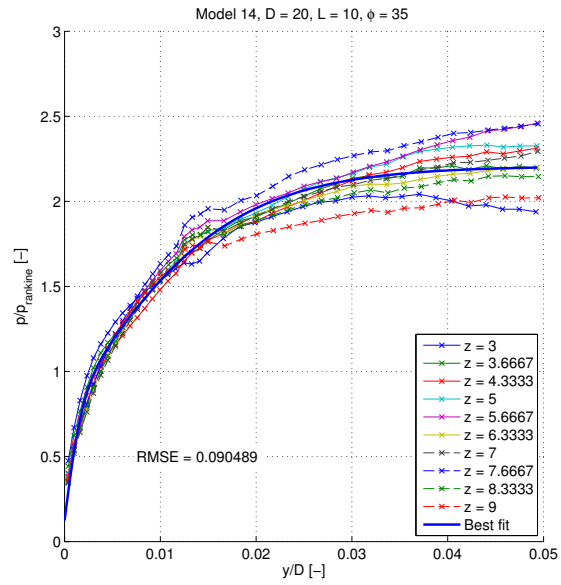


Figure B.54.  $\frac{p}{p_R} - \frac{y}{D}$  data

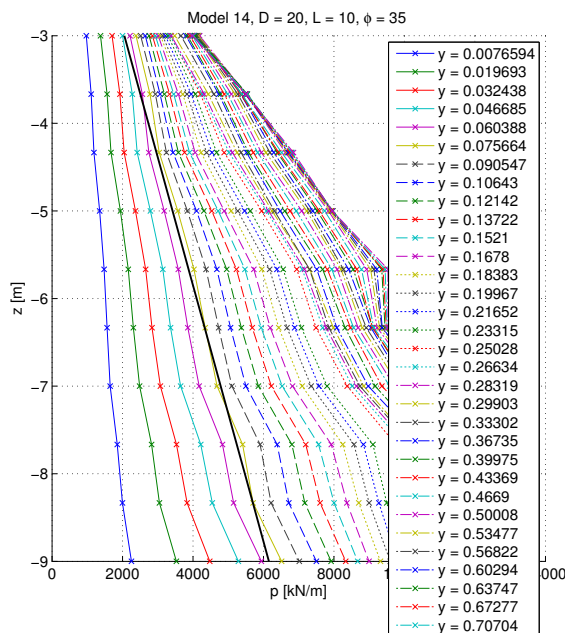


Figure B.55.  $p - z$  data

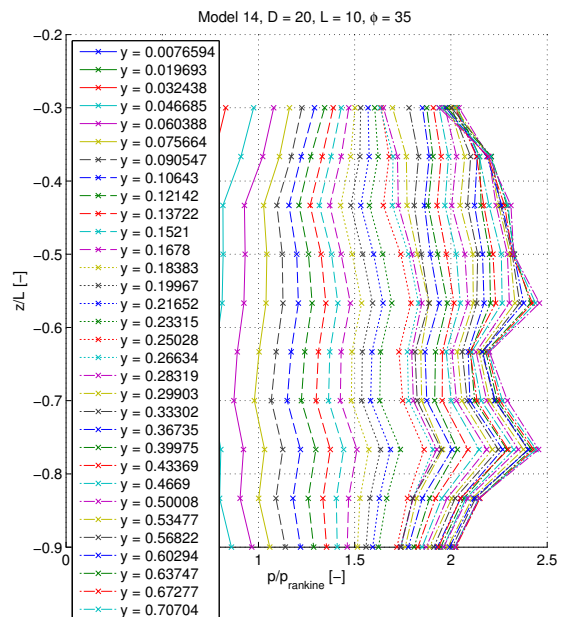


Figure B.56.  $\frac{p}{p_R} - \frac{z}{L}$  data

## B.15 Model 15

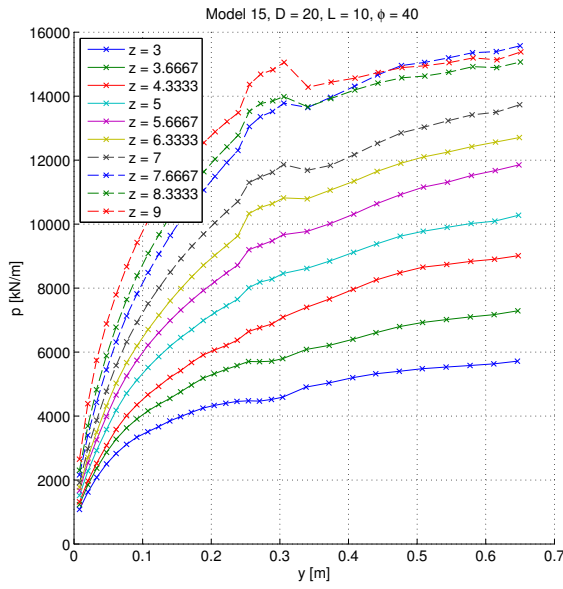


Figure B.57.  $p - y$  data

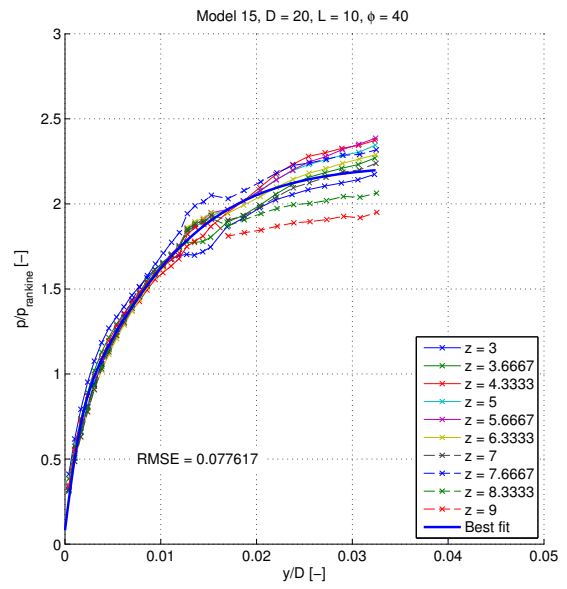


Figure B.58.  $\frac{p}{p_R} - \frac{y}{D}$  data

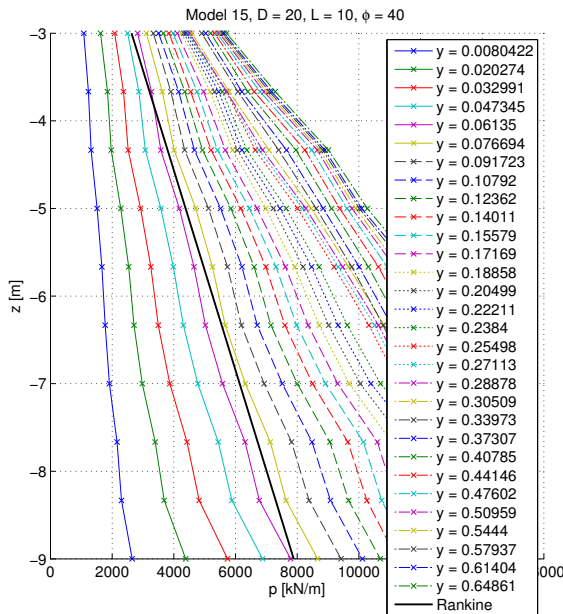


Figure B.59.  $p - z$  data

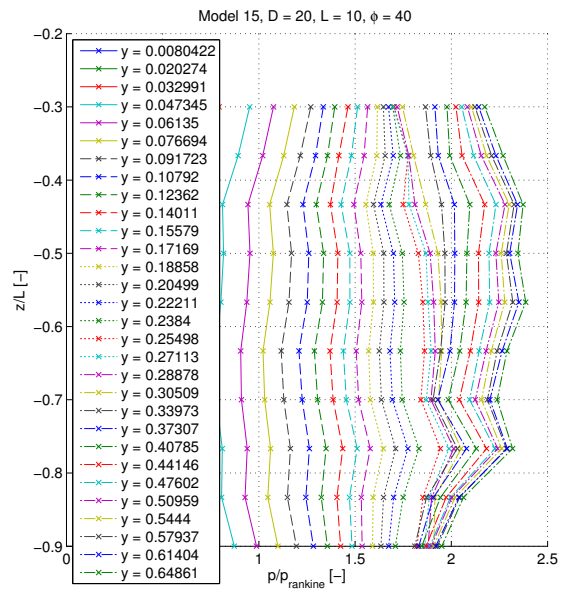


Figure B.60.  $\frac{p}{p_R} - \frac{z}{L}$  data

## B.16 Model 16

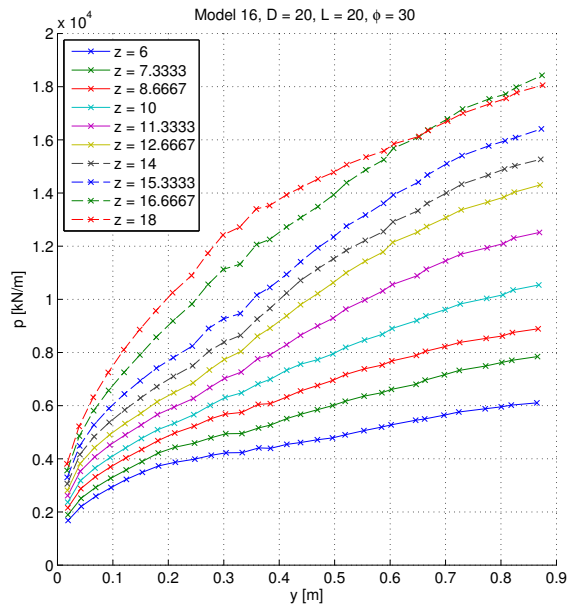


Figure B.61.  $p - y$  data

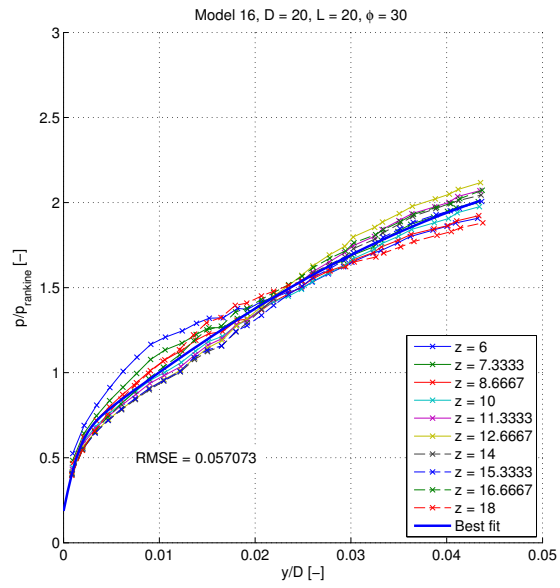


Figure B.62.  $\frac{p}{p_R} - \frac{y}{D}$  data

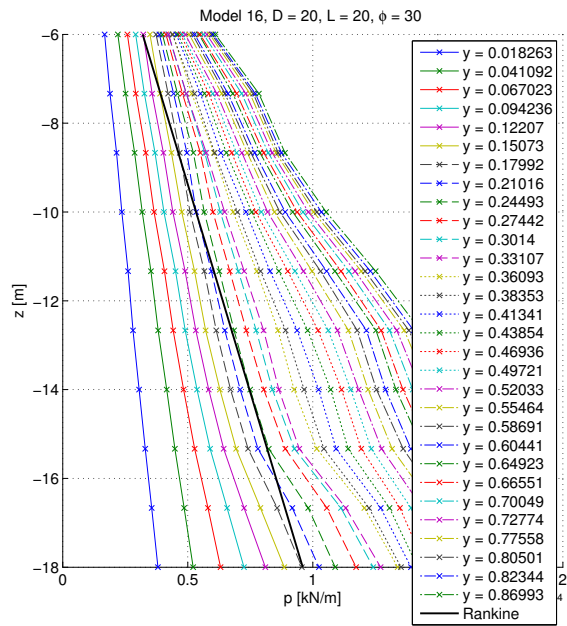


Figure B.63.  $p - z$  data

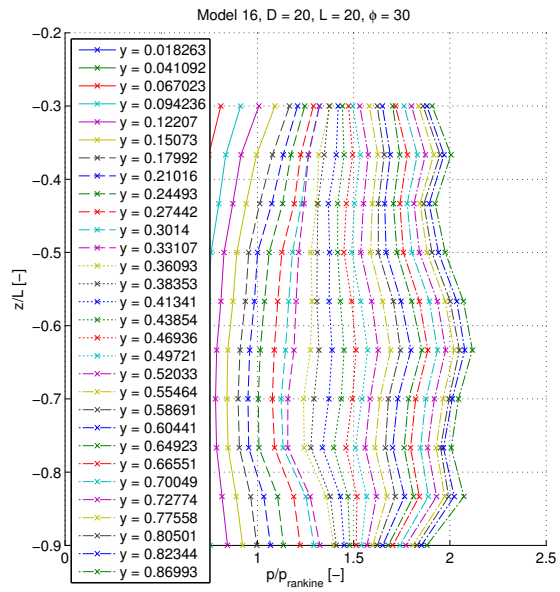


Figure B.64.  $\frac{p}{p_R} - \frac{z}{L}$  data

## B.17 Model 17

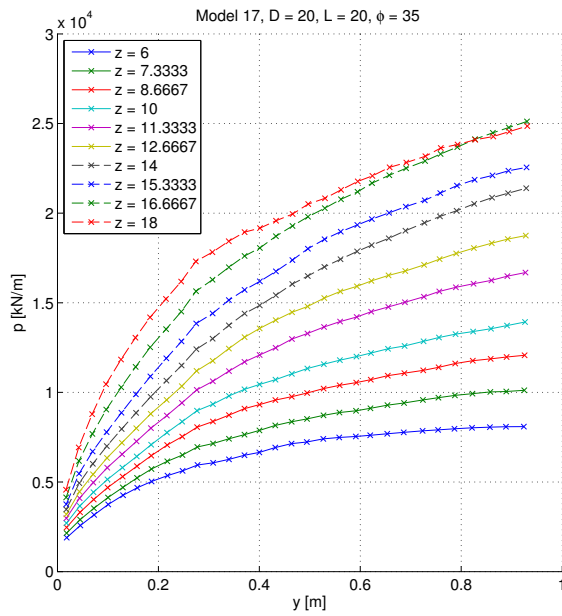


Figure B.65.  $p - y$  data

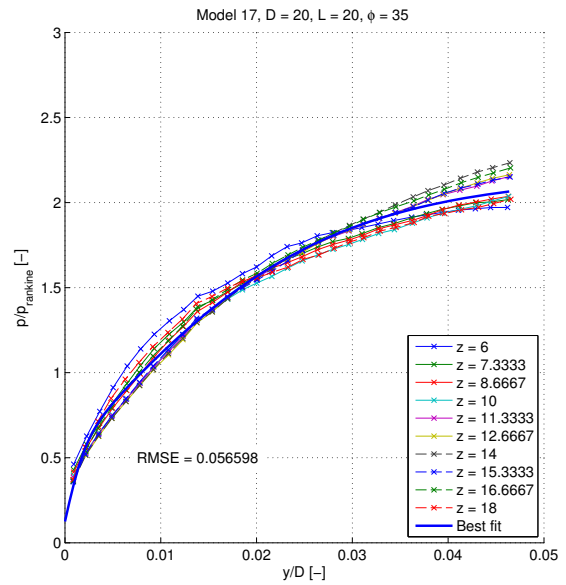


Figure B.66.  $\frac{p}{p_R} - \frac{y}{D}$  data

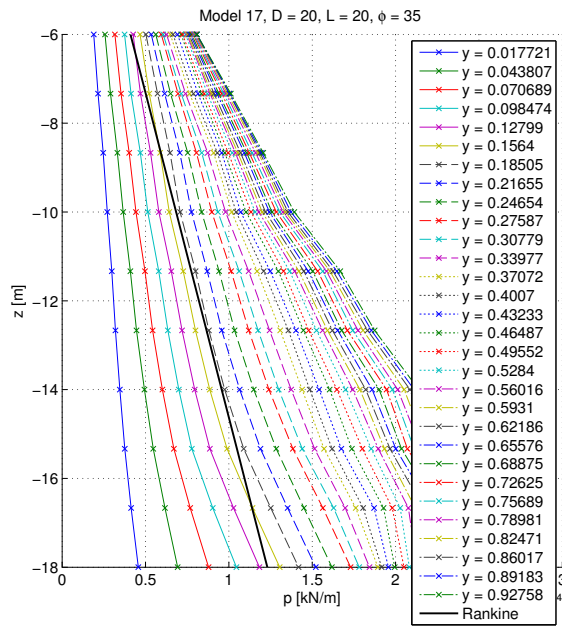


Figure B.67.  $p - z$  data

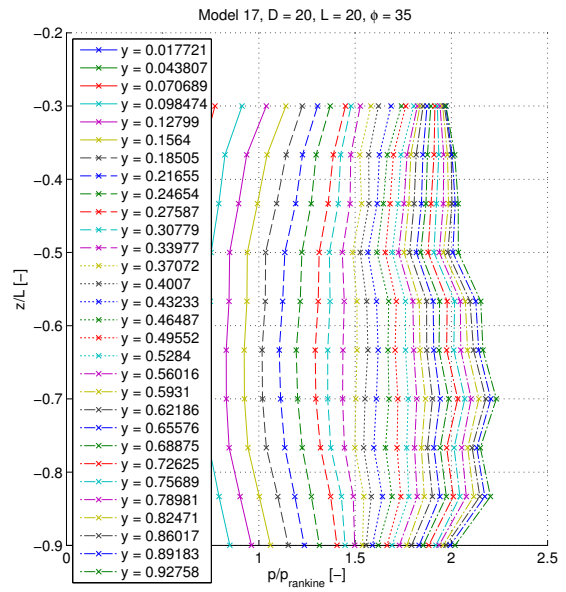


Figure B.68.  $\frac{p}{p_R} - \frac{z}{L}$  data

## B.18 Model 18

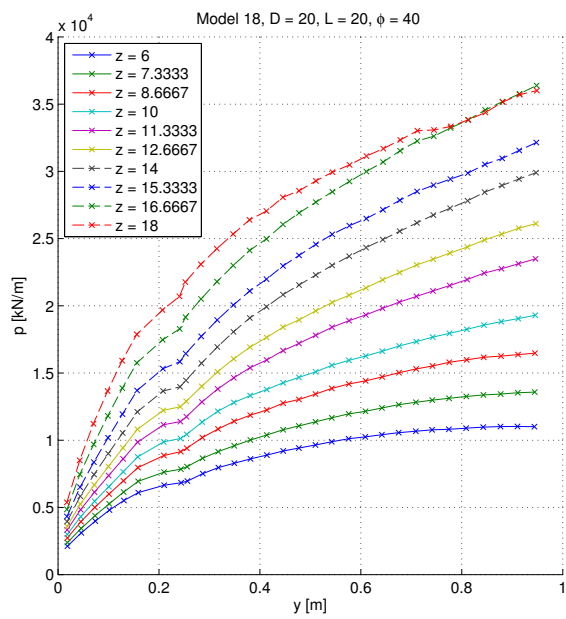


Figure B.69.  $p - y$  data

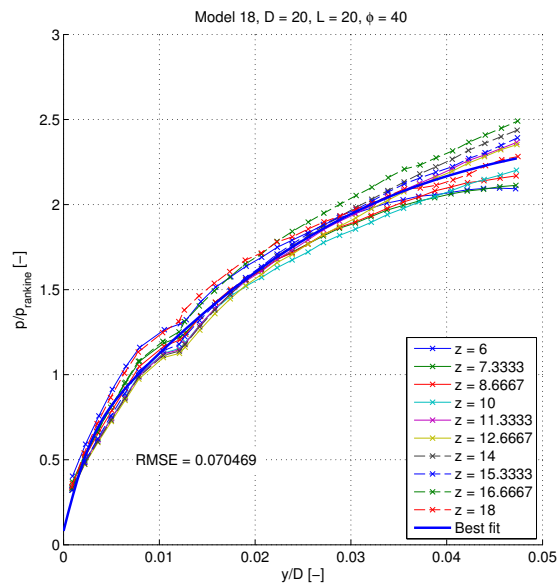


Figure B.70.  $\frac{p}{p_R} - \frac{y}{D}$  data

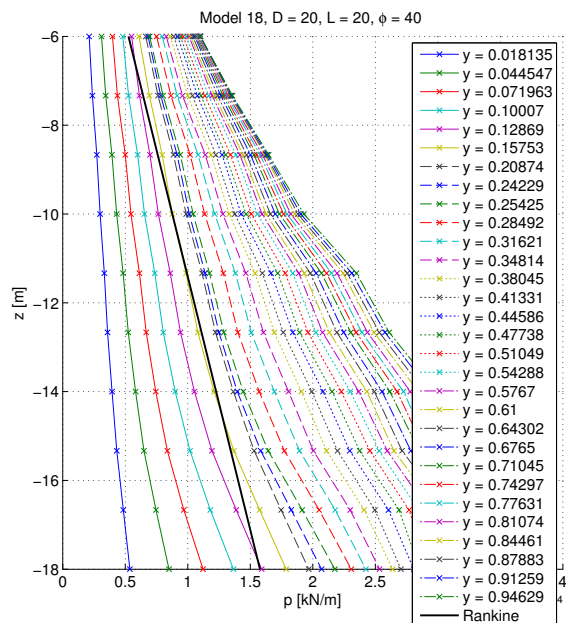


Figure B.71.  $p - z$  data

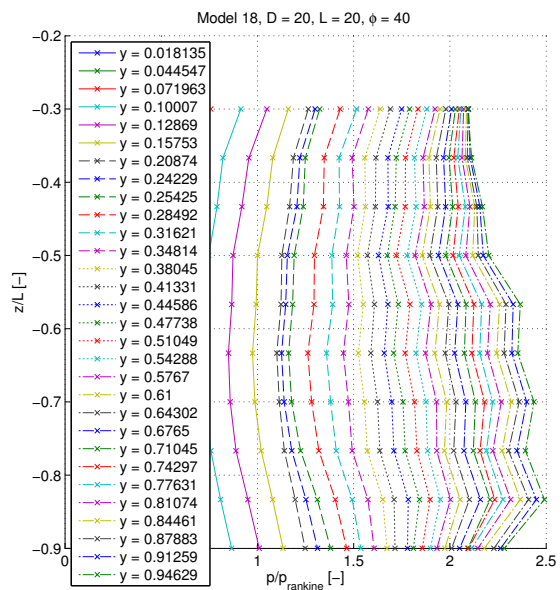


Figure B.72.  $\frac{p}{p_R} - \frac{z}{L}$  data

# C Mathematical Formulation of the New p-y Curves

Based on the results of the 18 PLAXIS 3D models, a proposal of a new mathematical formulation of  $p - y$  curves for the bucket foundation in drained sand has been made in Knudsen et al. [2013b]. The formulation of the model is a sum of two hyperbolic tangent terms and a constant term based of the soil pressure at rest.

$$\frac{p}{p_R} = \beta_1 \tanh\left(\beta_2 \frac{y}{D}\right) + \beta_3 \tanh\left(\beta_4 \frac{y}{D}\right) + \frac{K_0}{K_\gamma^p - K_\gamma^a} \quad (\text{C.1})$$

$p$	Soil pressure [kN/m]
$p_R$	Resultant Rankine pressure [kN/m]
$\beta_1 - \beta_4$	Fitting parameters [-]
$y$	Displacement [m]
$D$	Diameter of bucket [m]
$K_0$	Coefficient of soil pressure at rest [-]
$K_\gamma^p$	Passive Rankine pressure
$K_\gamma^a$	Active Rankine pressure

As the displacement  $y$  goes towards infinity, the absolute pressure is obtained,

$$\frac{p}{p_R} \rightarrow \beta_1 + \beta_3 + \frac{K_0}{K_\gamma^p - K_\gamma^a} \text{ for } \frac{y}{D} \rightarrow \infty, \quad (\text{C.2})$$

In order to find the coefficients  $\beta_i$  for a arbitrary sand and geometry of the bucket, the following equations should be solved simultaneous in pairs,

$$\beta_1 + \beta_3 = a_1 \frac{\phi}{L} + a_2 \quad (\text{C.3})$$

$$\beta_1 \beta_3 = b_1 \frac{\phi}{L} + b_2 \quad (\text{C.4})$$

$$\beta_2 + \beta_4 = c_1 \left(\frac{\phi}{L}\right)^2 + c_2 \frac{\phi}{L} + c_3 \quad (\text{C.5})$$

$$\beta_2 \beta_4 = d_1 \left(\frac{\phi}{L}\right)^2 + d_2 \frac{\phi}{L} + d_3 \quad (\text{C.6})$$

All the constants  $a_i$ ,  $b_i$ ,  $c_i$  and  $d_i$  are found in table C.1.

$a_1$	$a_2$	$b_1$	$b_2$	$c_1$	$c_2$	$c_3$	$d_1$	$d_2$	$d_3$
$\left[\frac{m}{\circ}\right]$	$[-]$	$\left[\frac{m}{\circ}\right]$	$[-]$	$\left[\left(\frac{m}{\circ}\right)^2\right]$	$\left[\frac{m}{\circ}\right]$	$[-]$	$\left[\left(\frac{m}{\circ}\right)^2\right]$	$\left[\frac{m}{\circ}\right]$	$[-]$
0.041	2.050	0.107	0.560	8.900	-13.12	66.24	936.5	-4579	5989

*Table C.1.* Constants used to find  $\beta_1$  to  $\beta_4$  in the general mathematical expression.

The model can be used with an arbitrary set of  $L$ ,  $D$  and  $\phi$ , however since the model is derived from models with  $L \in [5,20]$ ,  $D \in [10,20]$  and  $\phi \in [30,40]$  it cannot be expected to be valid outside this range. In the following the results from the models, the best fit and the mathematical model are shown together.

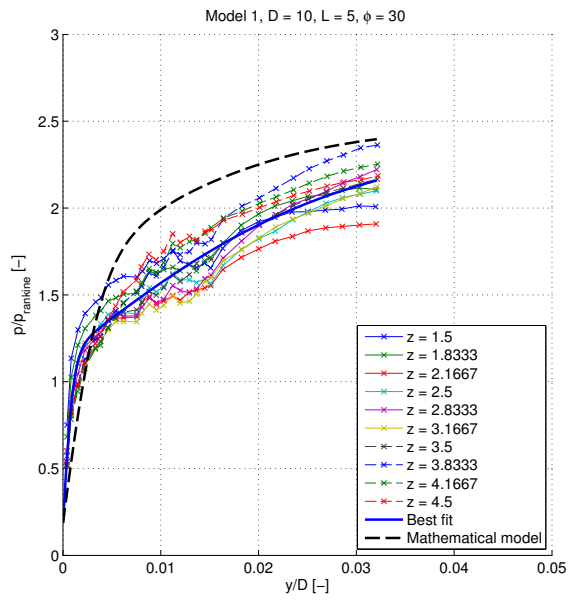


Figure C.1. Model 1

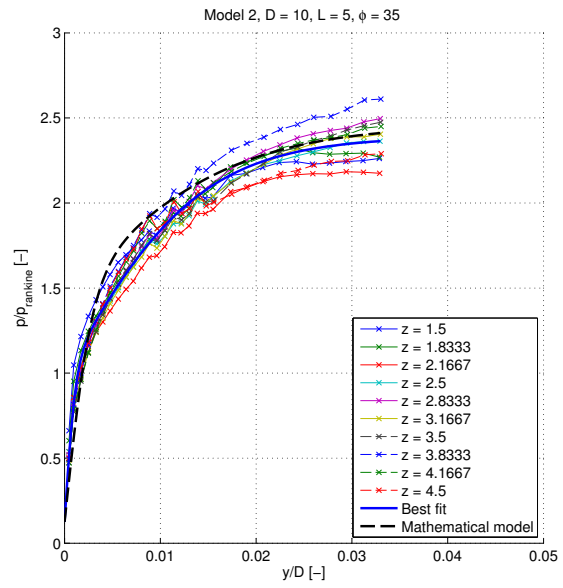


Figure C.2. Model 2

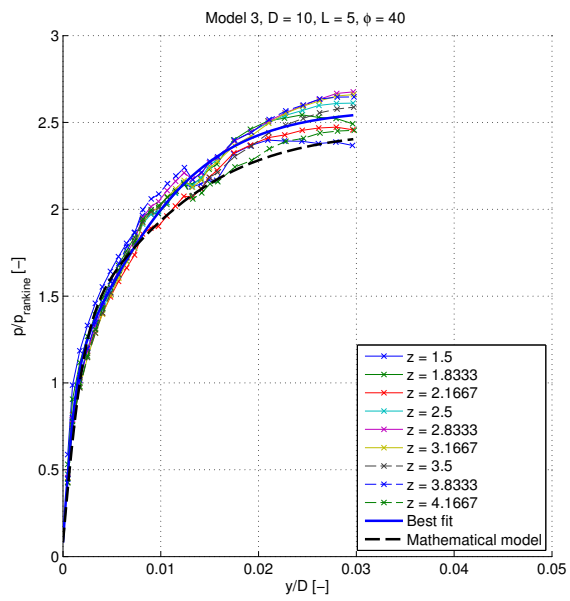


Figure C.3. Model 3

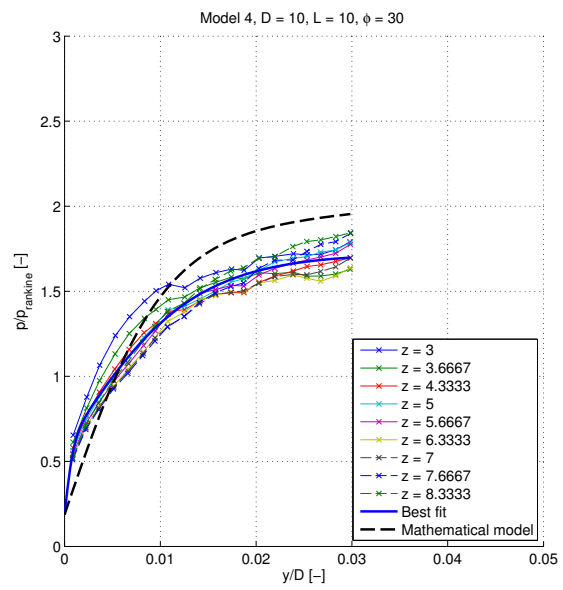


Figure C.4. Model 4

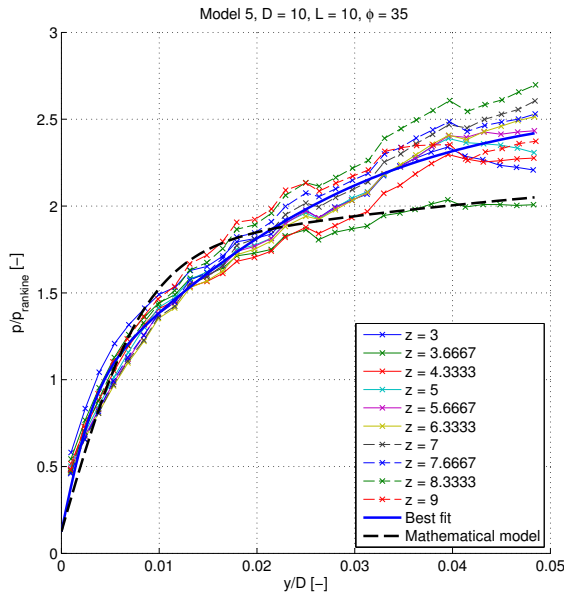


Figure C.5. Model 5

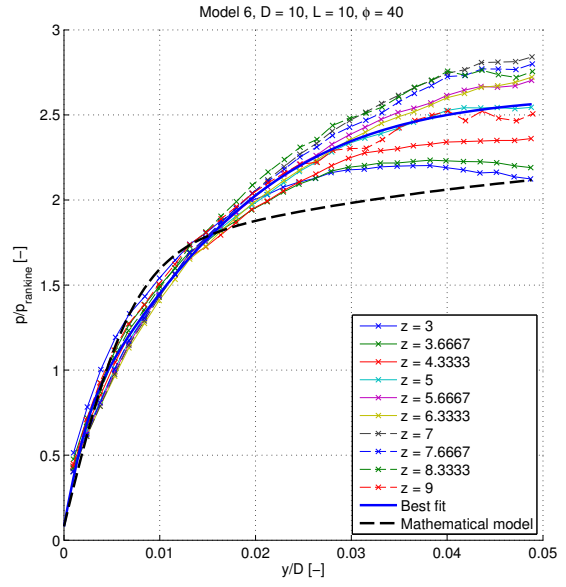


Figure C.6. Model 6

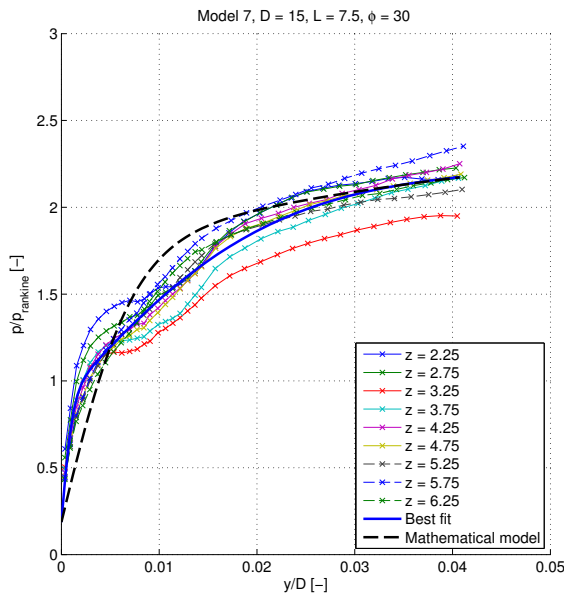


Figure C.7. Model 7

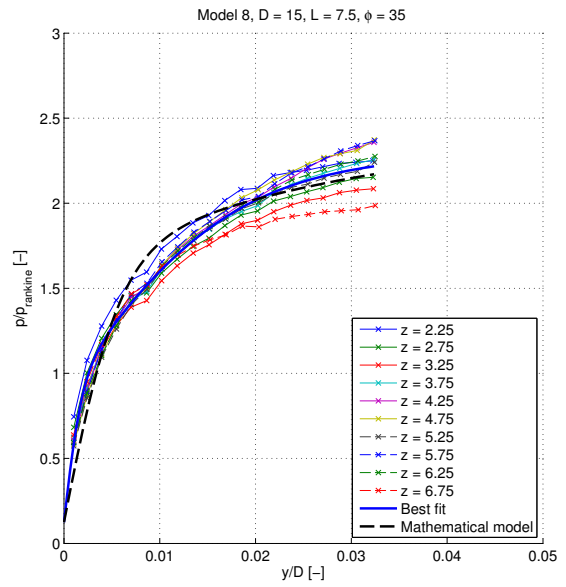


Figure C.8. Model 8

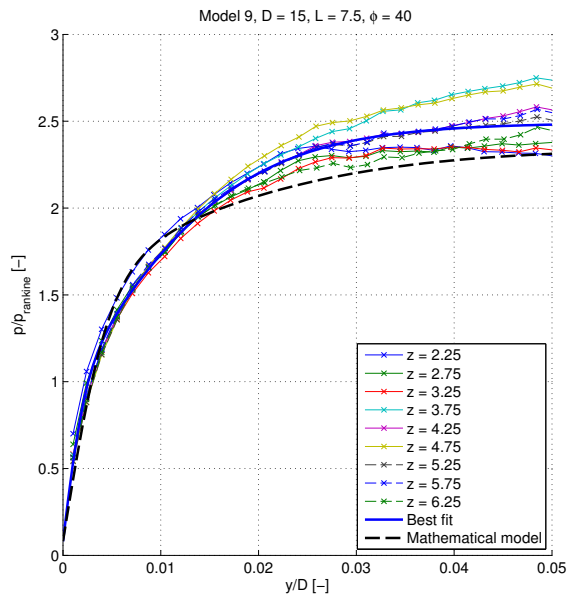


Figure C.9. Model 9

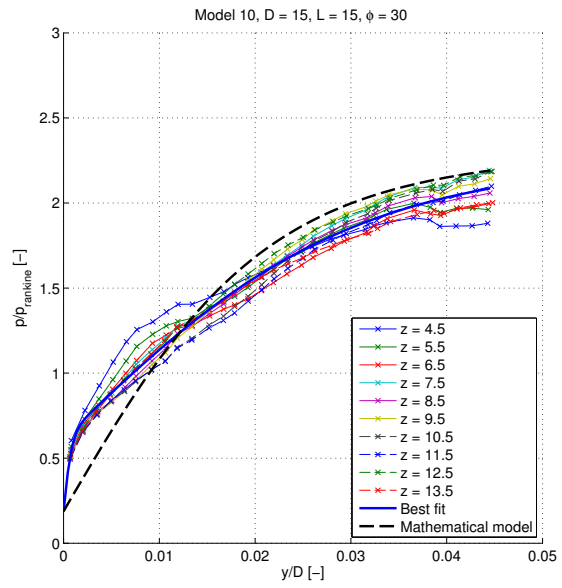


Figure C.10. Model 10

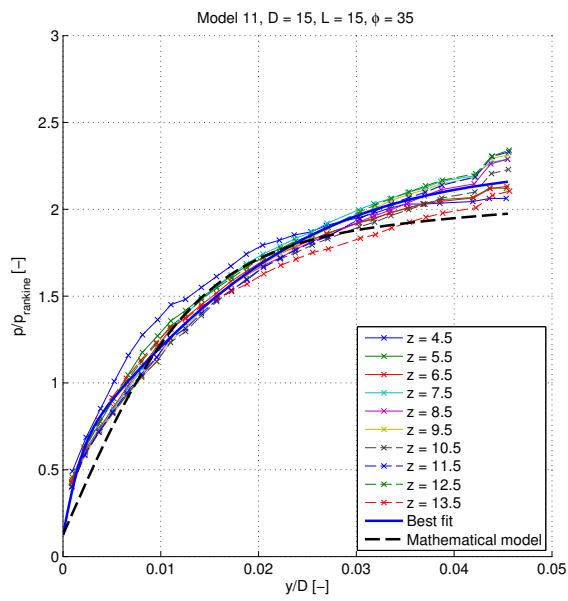


Figure C.11. Model 11

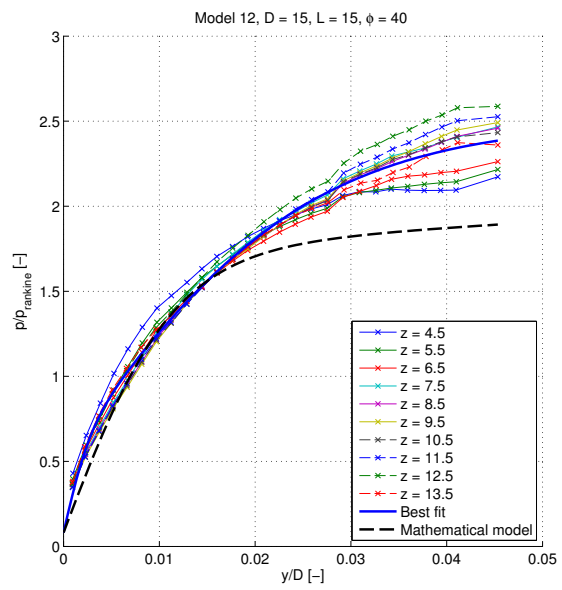


Figure C.12. Model 12

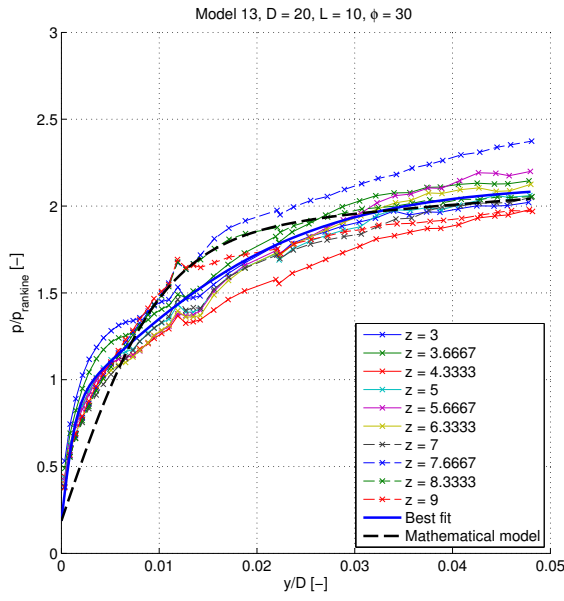


Figure C.13. Model 13

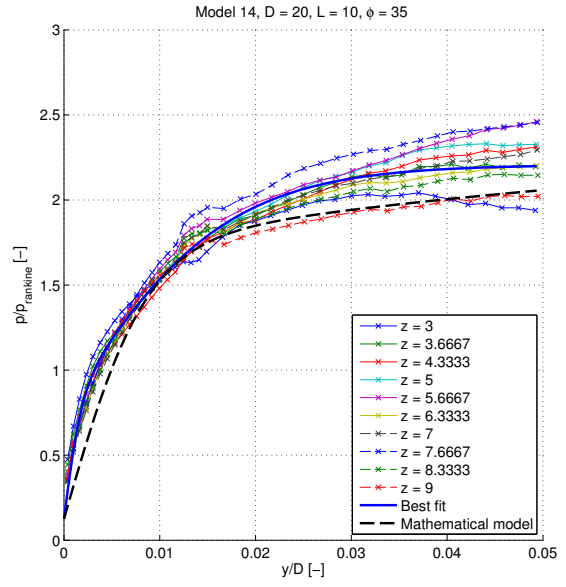


Figure C.14. Model 14

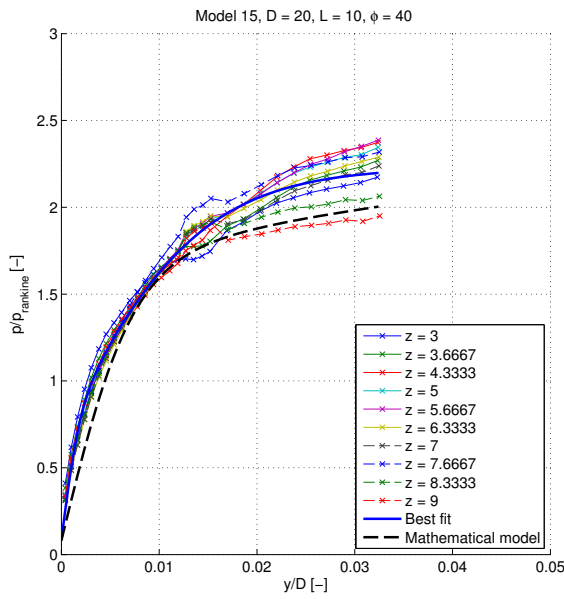


Figure C.15. Model 15

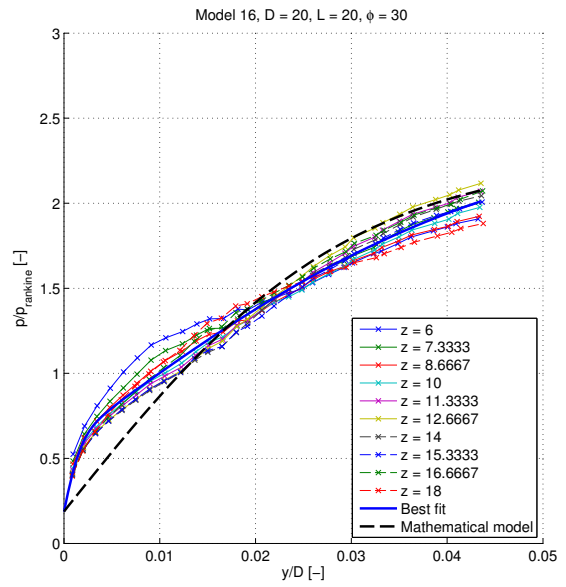


Figure C.16. Model 16

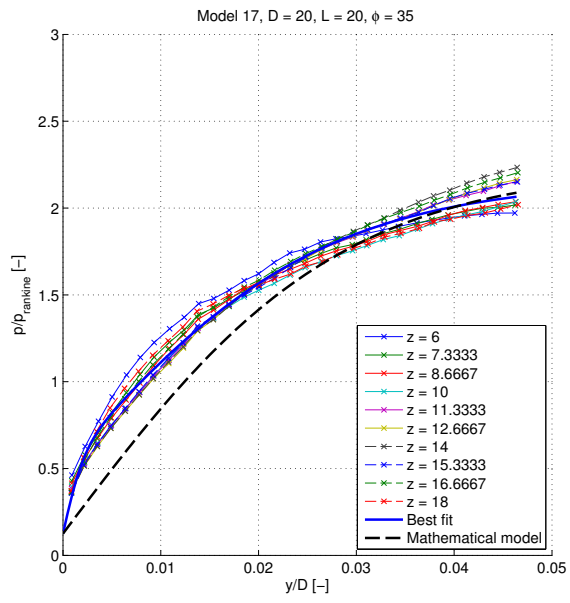


Figure C.17. Model 17

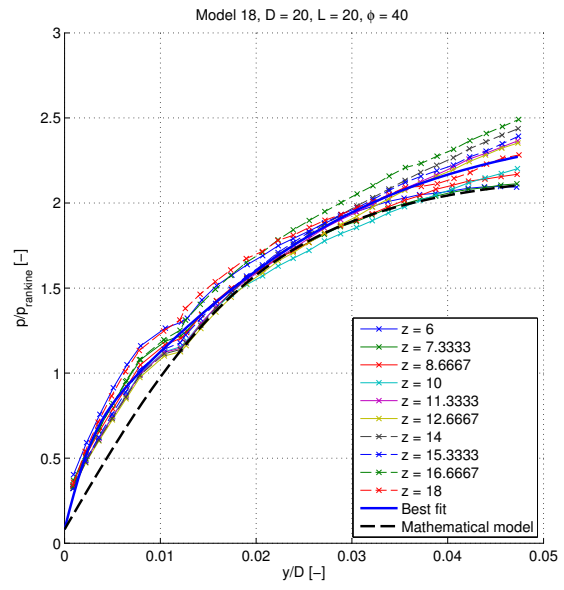


Figure C.18. Model 18

# D Hardening Soil Small Strain material model

In the investigation of p-y curves for the bucket, the Hardening Soil Small Strain (HSsmall) material model is used. In this appendix an outline of the mechanics of this model is given. Firstly the Hardening Soil (HS) model is explained, whereafter the small strain part is added.

The model is chosen as it is a well suited model for investigating soil response at low stress levels and because it is able to handle unloading-reloading problems as the one used in this project. The HS model gives a formulation of the stiffness parameters as a function of the stress state in the soil, while the failure of the soil is governed by the Mohr Coulomb (MC) failure criterion.

The HSsmall model requires a relatively large number of soil parameters, requiring detailed information about the soil to be modelled. An important fact is thus that the model is never better than the input-parameters. In this project standard well-tested expressions and relations between the soil parameters are used, all based on the friction angle and the minimum and maximum void ratio of the soil.

## D.1 Mohr-Coulomb criterion in 3D

The ultimate failure of the soil is governed by the Mohr-Coulomb criterion, using the friction angle  $\varphi$  and the cohesion  $c$  as the material strength parameters. It can be expressed explicitly in the principal stresses as,

$$\pm \frac{\sigma_1 - \sigma_2}{2} = \left( \frac{\sigma_1 + \sigma_2}{2} \right) \sin(\varphi) - c \cos(\varphi), \quad (\text{D.1})$$

$$\pm \frac{\sigma_2 - \sigma_3}{2} = \left( \frac{\sigma_2 + \sigma_3}{2} \right) \sin(\varphi) - c \cos(\varphi), \quad (\text{D.2})$$

$$\pm \frac{\sigma_3 - \sigma_1}{2} = \left( \frac{\sigma_3 + \sigma_1}{2} \right) \sin(\varphi) - c \cos(\varphi). \quad (\text{D.3})$$

In the principal stress space, the yield surface can be visualised as seen in figure D.1. Tension is negative in this formulation, compression is positive.

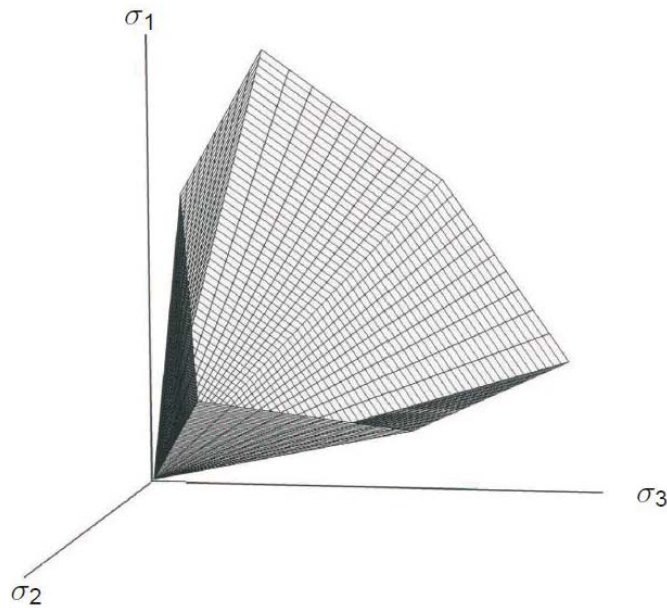


*Figure D.1.* The Mohr-Coulomb failure surface in the three dimensional principal stress space. [Brinkgreve et al., 2012]

## D.2 The HS model

The HS model provides a formulation to calculate the strain development in the soil using a stress-dependent stiffness. The model uses different stiffness models in respectively virgin loading and un- and reloading. This makes the model suitable for this project. The model is formulated based on classical theory of plasticity, and an outline will be given in the following.

The HS model uses a hyperbolic relationship between the stresses and strains, which is observed during primary triaxial loading. The relationship is exemplified in figure D.2. In the figure, the two of the stiffness moduli used in the model are also shown.

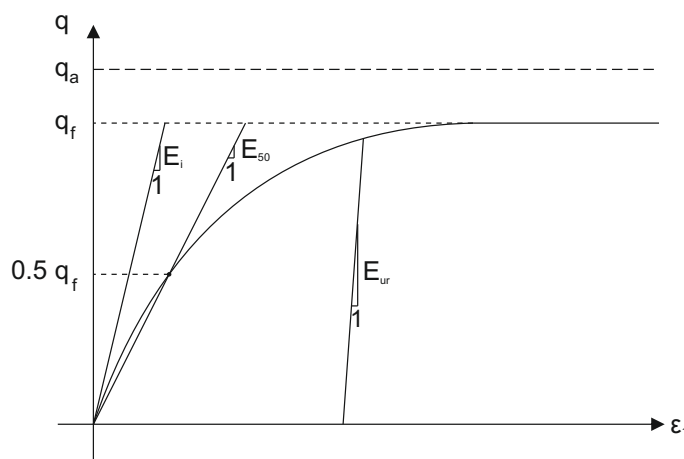


*Figure D.2.* The relationship between stresses and strain in primary deviatoric loading. The deviatoric failure stress is  $q_f$ , the deviatoric asymptotic stress is  $q_a$ , the initial stiffness is  $E_i$ , the secant stiffness through the half of the deviatoric failure stress  $q_{50}$  is  $E_{50}$  and the unloading-reloading stiffness is  $E_{ur}$ . [Schanz et al., 1999]

The HS model incorporates hardening in the soil once the stress-state has reached the present yield surface. As the stress state reaches the yield surface, the material will start hardening as the yield surface expands. The yield surface of the HS model is a so-called multisurface yield criterion, causing two different kinds of hardening to take place.

The two types of hardening are shear hardening and compression hardening. Shear hardening occurs as a function of deviatoric loading, i.e.  $q = \sigma_1 - \sigma_3$  increases. When  $q$  increases, so does the shear stress in the soil, hence the name shear hardening. The yield envelope with respect to deviatoric loading, resembles the hexagonal cone of the MC yield surface. As the material hardens, the cone expands until it reaches the ultimate state given by the MC criterion. The hardening is illustrated in figure D.3.

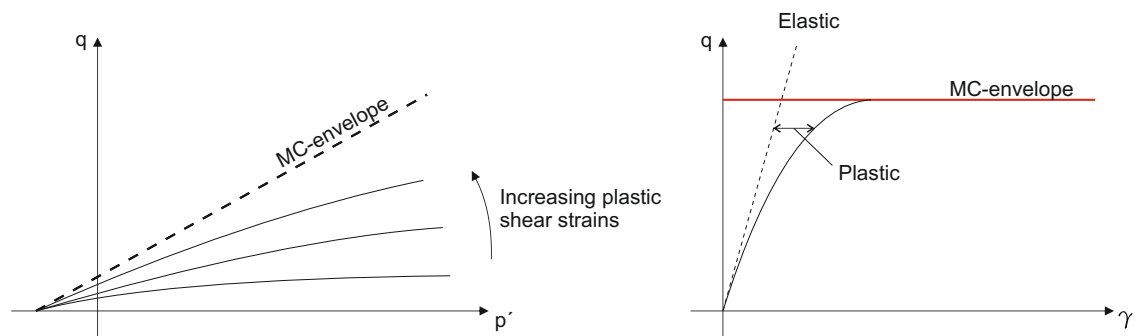


**Figure D.3.** Deviatoric hardening shown in  $p$ - $q$  (mean stress-deviatoric stress) and  $\gamma$ - $q$  (shear strain-deviatoric stress) diagram. [Schanz et al., 1999] [Karstunen, 2012]

As the deviatoric loading is increased, the yield surface expands while an increasing amount of plastic strains develop.

The other type of hardening is compression hardening, which occurs as the mean stress increases, e.g. isotropic compression, and plastic strains develop. The hexagonal yield surface, cf. figure D.1, does not account for this type of strain development, as the hydrostatic stress axis, i.e.  $\sigma_1 = \sigma_2 = \sigma_3$ , does not intersect the yield surface in the compression regime. To cope with this a cap is introduced to the yield surface closing off the elastic region in the direction of the  $p$  - axis. The cap has the same hexagonal shape as the MC criterion, while its dimensions are determined from the pre-consolidation stress  $p_c$ , the coefficient of lateral earth pressure  $K_0$  and the modulus of elasticity for oedometer loading  $E_{\text{oed}}$ . The cap and the different hardening zones are shown on figure D.4.

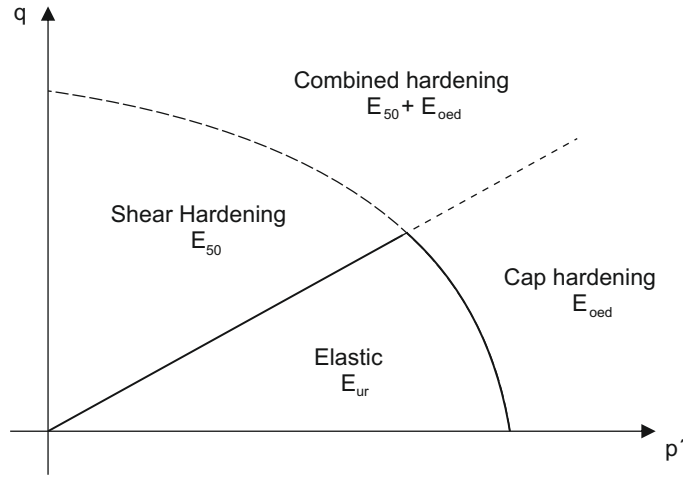


Figure D.4. The multisurface yield surface in p-q space. The four possible stiffness zones are shown. [Schanz et al., 1999]

In the three dimensional stress space, the multi-surface yield locus is a hexagonal cone with a hexagonal cap. The shape is illustrated in figure D.5.

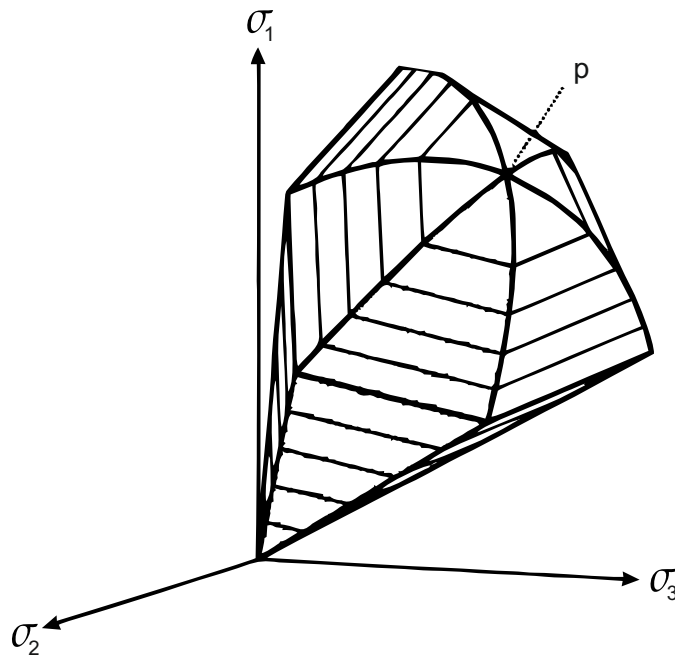
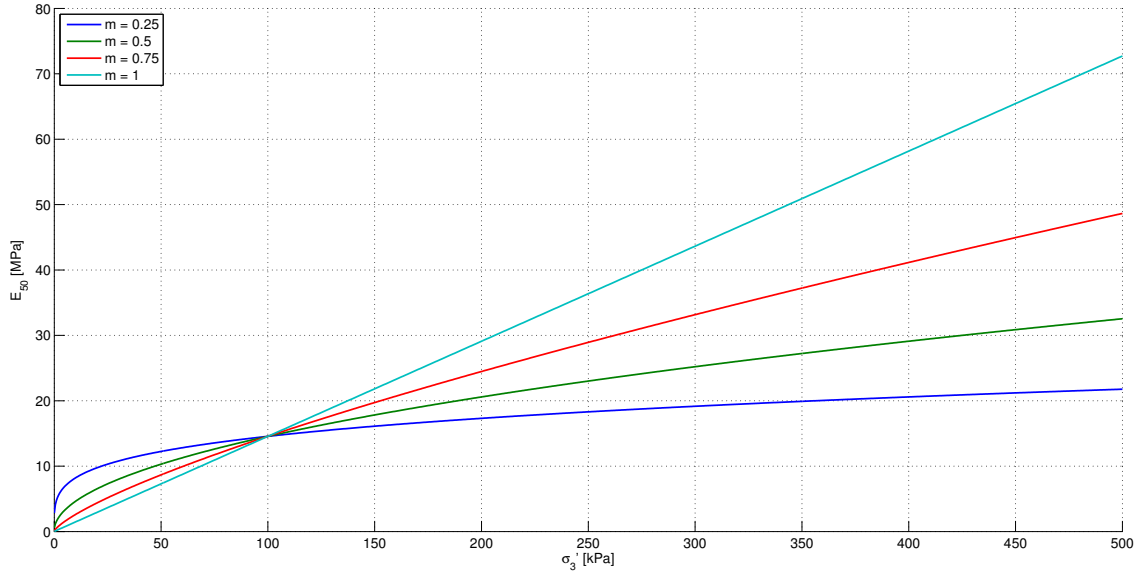


Figure D.5. The yield surface in 3d stress space. [Schanz et al., 1999]

The stiffness moduli incorporated in the model, such as  $E_{50}$ ,  $E_{oed}$  and  $E_{ur}$  are all dependent on the stress state in the soil. The values are input at a given reference stress  $\sigma_3 = \sigma_{ref}$ , from which values at other stress states are calculated. The expression for  $E_{50}$  is given in equation (D.4).

$$E_{50} = E_{50}^{ref} \left( \frac{\sigma_3 + c \cot(\varphi)}{\sigma_{ref} + c \cot(\varphi)} \right)^m \quad (D.4)$$

In equation (D.4) the parameter  $m$  is the shape parameter of the curve, which is an input parameter for the HS model. In figure D.6 the development of  $E_{50}$  is shown with varying  $m$  values.



**Figure D.6.** Plot of the development of  $E_{50}$  as a function of the  $\sigma_3$  and the shape parameter  $m$  for  $E_{50}^{ref} = 14.56$  MPa,  $c = 0.1$  kPa,  $\varphi = 35^\circ$  and  $\sigma_{ref} = 100$  kPa.

All the curves on figure D.6 intersects at the value of  $(\sigma_{3,ref}' ; E_{50}^{ref})$ . The value of  $m$  is dictated by the soil type, and it is usually recommended to use around 1.0 for soft clays and 0.5 for sand and silt.  $m = 0.5$  is used in this project. Similar expression as equation D.4 exists for  $E_{ur}$  and  $E_{oed}$ . [Brinkgreve et al., 2012].

### D.3 The HSsmall model

At small strains, i.e. below  $10^{-6}$ , empirical data has shown stiffness of soil to be a lot higher than at the strain amplitudes normally used in laboratory tests. The stiffness of the soil then decreases as the amplitude of the applied strains increase. This larger stiffness was at first experienced in soil dynamics, as the strains in relation to propagating waves in the soil volume are very small. Due to this, a dynamic stiffness of the soil has previously been used. This dynamic stiffness is equal to the small strain stiffness in the formulation of the HSsmall model called respectively  $E_0$  and  $G_0$ . Figure D.7 shows an illustration of the development of the ratio of the present shear modulus to the initial shear modulus.

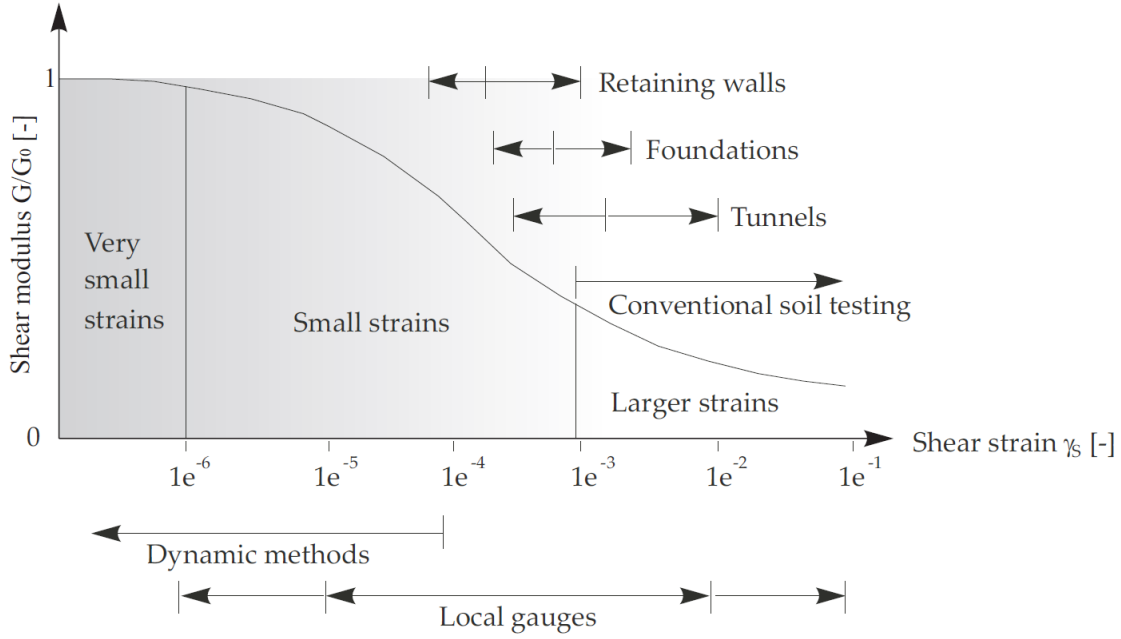


Figure D.7. The ratio of  $G/G_0$  as a function of strain amplitude. [Brinkgreve et al., 2012]

Various formulations of the development of  $G/G_s$  have been proposed, and PLAXIS uses a formulation suggested by dos Santos and Correia [2001]. The additional stiffness at small strains is incorporated through the parameters  $G_0$  and  $\gamma_{0.7}$ , which are the initial shear modulus and the value of the strain strain where  $G/G_0 \approx 0.7$ . The shear stiffness found in laboratory tests is the secant shear modulus  $G_s$ , which is used to formulate the stress-strain relationship,

$$\tau = G_s \gamma = \frac{G_0 \gamma}{1 + 0.385 \frac{\gamma}{\gamma_{0.7}}}. \quad (D.5)$$

Differentiating this relationship gives the tangent shear modulus in equation (D.6), which is the current shear stiffness used in HSsmall at a shear strain ratio  $\frac{\gamma}{\gamma_{0.7}}$ .

$$G_t = \frac{G_0}{\left(1 + 0.385 \frac{\gamma}{\gamma_{0.7}}\right)^2}, \quad G_t \geq G_{ur}. \quad (D.6)$$

The reduction of  $G_t$  has effect both in the elastic and plastic region, and is cut off at a lower bound equal to  $G_{ur}$ . Equation (D.7) and (D.8) provide relations between the different stiffness parameters.

$$G_t = \frac{E_t}{2(1 + \nu_{ur})}, \quad E_t \geq E_{ur}, \quad (D.7)$$

$$G_{ur} = \frac{E_{ur}}{2(1 + \nu_{ur})}. \quad (D.8)$$

For primary loading scenarios, the HSsmall model then uses the same formulations as the HS model, with  $E_{ur}$  and  $G_{ur}$  replaced by  $E_t$  and  $G_t$ .

In the HS model the unloading/reloading path is assumed to be linearly elastic, i.e. the slope of the stress-strain curve is constant at a value of  $E_{ur}$ . This property of the soil

is however not realistic, when the change in strain is large. In other words, it is not possible for the soil to recover from strains totally, unless the applied strains are very small. The unloading-reloading in the HSsmall model takes this into account, which is illustrated in figure D.8.

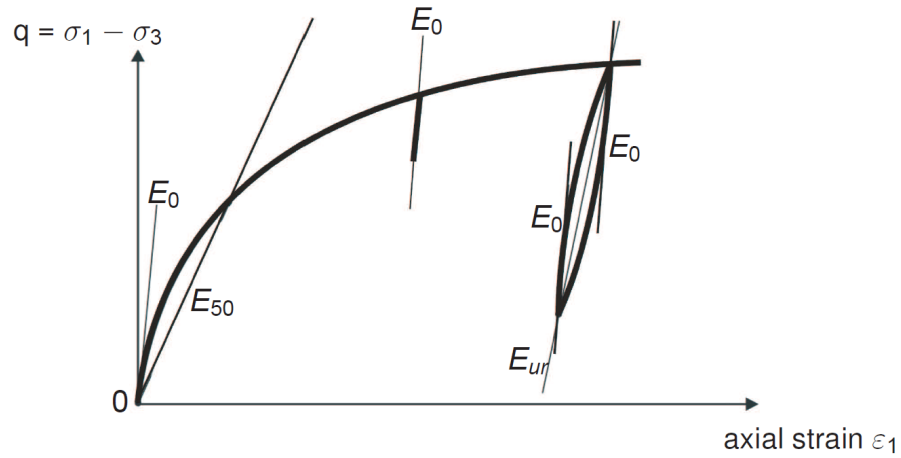


*Figure D.8.* The unloading-reloading relationship in the HSsmall model. [Brinkgreve et al., 2012]

This is done by monitoring the loading history of the soil, and taking this into account before each strain increment is calculated.

## D.4 On the significance of using small strain hardening soil

The HSsmall model introduces additional calculation complexity, as the stiffness parameters vary not only due to hardening but also due to the additional small strain stiffness. Furthermore the monitoring of loading history also requires additional calculation, all in all causing the use of the HSsmall model to be more demanding. It is however justified to do so, since the model often yield results that are closer to the real case.

By not accounting for the additional small strain stiffness of the soil, the deformations of the soil body may be overestimated and as a consequence the stresses will be underestimated. This is both the case when comparing to the HS model, and of course even more severe compared to the MC model. In the investigations of this project, the deformations and stresses even at very small loads are important, since the objective is to define the p-y relationship all the way from a very small deformation to the ultimate failure case. Not using HSsmall would thus give a less stiff, and less realistic, response at small deformations.

Another advantage of the HSsmall model is that it is less sensitive to the boundaries of the FEM domain, as parts with small straining are very stiff. The following figure is taken from a comparison HS and HSsmall, when calculation settlements of a simple foundation.

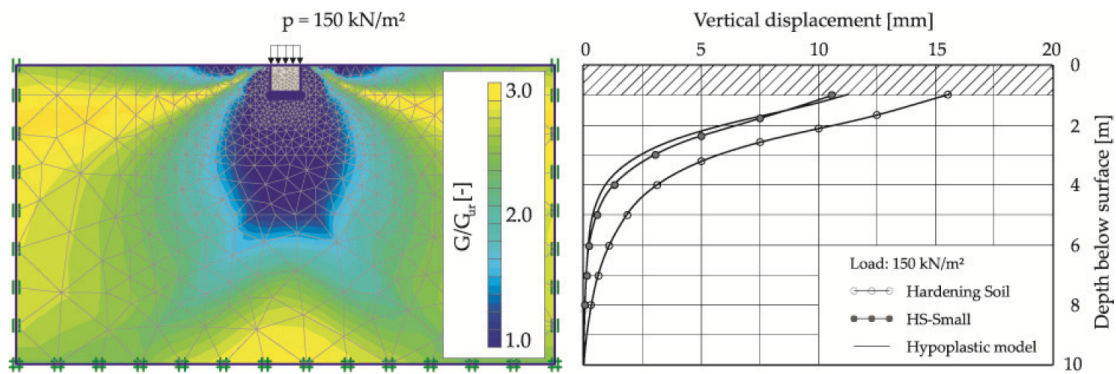


*Figure D.9.* Comparison of settlements calculated with a HS, a HSsmall and a hypoplastic model. As can be seen, the HSsmall model gives smaller vertical displacements. [Karstunen, 2012]

# E Implementation of a UDSM in PLAXIS

---

This chapter deals with the methodology and principles of creating a User Defined Soil Model (UDSM) and using it together with the interface and calculation engine of PLAXIS 3D. The goal of the process is to implement a soil model where the strength is dependent on the stress level in the soil. A model like this is not currently available in PLAXIS.

In the next sections the emphasis for using such a soil model is given along with a description of the mechanics of the model. The UDSM is programmed in Fortran, and a detailed hands-on description of the necessary steps needed to do the actual implementation in PLAXIS is presented. Furthermore the FEM calculation procedure is outlined, to give an understanding of what tasks are carried out by PLAXIS and what is done in the UDSM.

## E.1 Emphasis for using a UDSM

Even though several advanced soil models are available in the PLAXIS 3D software, not all aspects of soil mechanics can be calculated properly using the existing models. In the field of geotechnics at Aalborg University a very large degree of the research conducted is done using experimental methods. In the experimental approach scaled models are used, mainly due to practical and economical possibilities. With scaling of models comes the usage of scaling laws, however an appropriate method of scaling soil mechanic properties is not available.

It has been observed through various triaxial tests of soil that both the stiffness and strength parameters of the soil are not constant nor simply linearly varying with the mean stress state  $p = (\sigma_1 + \sigma_2 + \sigma_3)/3$ . While the variation of the stiffness parameters are accounted for by the Hardening Soil (HS) model in PLAXIS, the change in strength parameters are not. At very low mean stress levels, such as those occurring in scaled laboratory tests, the friction angle of non-cohesive materials has been observed to be significantly higher than at higher levels of  $p$ , where it becomes close to constant. [Krabbenhøft et al., 2011].

In figure E.1 the variation of the angle of friction using both experimental methods and calculations with Boltons formula is shown. The increase in friction angle is clearly seen at low confining pressures.

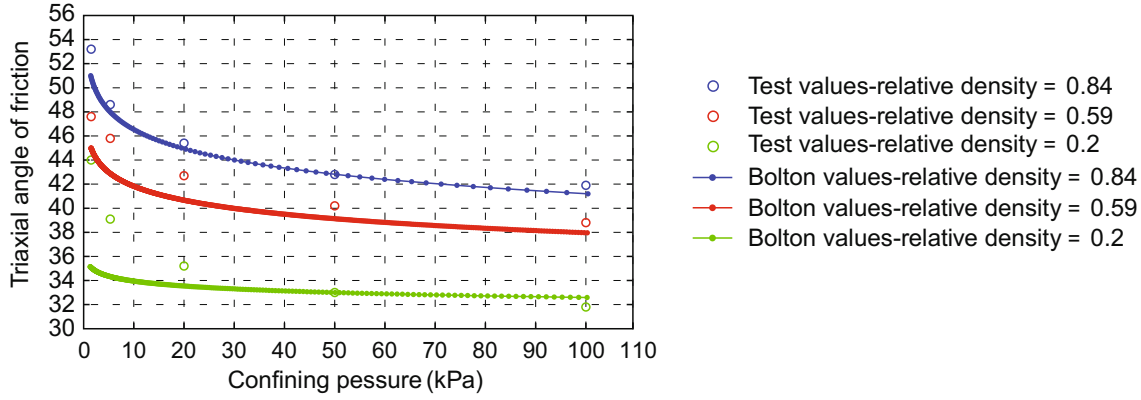


Figure E.1. The variation of the friction angle from tests and from Bolton's formula. [Krabbenhøft et al., 2011]

With a material model that takes the significant increase of strength at low stress level into account, it will be possible to better reproduce and verify the experimental results using numerical methods. This is the main emphasis for implementing a UDSM in PLAXIS.

## E.2 The soil mechanics of the UDSM

In this section the mechanics of the applied soil model is explained. Throughout the section the sign convention is such that compression is positive and tension is negative. This is opposite of the general finite element approach. The geotechnical approach however, is to have the sign convention as used in this description.

### E.2.1 The failure criterion

The failure criterion used is a non-linear Mohr-Coulomb criterion. The non-linear part of the criterion is used to model the observation of higher relative strength at low stress levels. The formulation of the criterion is,

$$f = k_0\sigma_3 - \sigma_1 + s_{c0} \left( 1 - \exp \left( -a \frac{\sigma_3}{s_{c0}} \right) \right) = 0. \quad (E.1)$$

The shape of the criterion is controlled by the three constants  $k_0$ ,  $s_{c0}$  and  $a$ . The formulation of the criterion goes towards an asymptote, when  $\sigma_3$  goes towards a very large positive value, e.g. very high compressions. Thus the formulation becomes,

$$f = k_0\sigma_3 - \sigma_1 + s_{c0} \quad , \quad \sigma_3 \rightarrow \infty, \quad (E.2)$$

which is identical to the Mohr-Coulomb criterion. Due to the nature of the mathematical formulation, the material constants are not directly comparable to any of the commonly used soil parameters. The slope of the asymptote is determined by  $k_0$ , and is thus comparable to the normally used friction parameter  $k$ , which is directly a function of the friction angle. The intersection with the  $\sigma_1$  axis of the asymptote is given by the parameter  $s_{c0}$ , and is thus comparable to the cohesion of the soil. The parameter  $a$  controls the curvature of the criterion, which is dominant at small stress levels.

The criterion can be calibrated to be used with any material exhibiting Mohr-Coulomb-like behaviour. In this project the criterion is fitted to be used with Aalborg University

Sand no. 1. In order to calibrate the parameters a series of triaxial tests are used, in which the back-pressure is varied to give failure points at different stress level. Since the curvature of the criterion is dominant at low stress levels, a series of tests including very low back pressures are used. The tests are carried out at the Geotechnics Laboratory at Aalborg University and are available in the data report by Ibsen and Bødker [1994].

### E.3 The contents of the UDSM

The PLAXIS calculation engine allows for usage of user-defined soil models, making it possible to implement any desired constitutive model for the soil. The constitutive model defines the relation between the strain and stress increments, and if needed also the time dependency, of the soil material. In principle the task of the UDSM is to calculate the current stress state based on strain and time increments and the previous stress state, which are all given by PLAXIS. As the implemented constitutive model is independent of time, no more references will be given to time dependency of the UDSM implementation in the following.

The UDSM has to be made in a programming language and compiled into a DLL-file (Dynamic Link Library), which is then read by PLAXIS. The implementation here is done using the Fortran programming language and the Intel Visual Fortran (IVF) compiler, however another language could be used if desired. The source-code for the UDSM is given in appendix F - *Source Code for UDSM*.

The UDSM programmed in Fortran must be a subroutine named *User\_Mod*, which can handle the following objectives,

- Initialisation of any needed state variables.
- Calculation of stresses using a constitutive model.
- Creation of the elastic and effective material stiffness matrices.

To execute the above mentioned objectives, the subroutine needs to be able to execute six different tasks called by the integer variable *IDTask*. A thorough description of all variables used will be given later. The six tasks are as follows, where the enumeration follows the variable  $IDTask = [1..6]$ ,

1. Initialize state variables in *StVar0*.
2. Calculate effective stresses and excess pore pressure in *Sig* and *Swp*.
3. Calculate effective material stiffness matrix *D*.
4. Output number of state variables *nStat*.
5. Output matrix properties *NonSym*, *iStrsDep*, *iTimeDep* and *iTang*.
6. Calculate elastic material stiffness matrix  $D^e$ .

The exchange of information between PLAXIS and the UDSM happens using a number of input and output variables listed in table E.1.

Variable	In/Out	Type	Description
<i>IDTask, iMod, iStep, iTer, iEl, Int</i>	In	I	Task number, model number, calculation step, iteration step, element number, integration point.
<i>IsUndr</i>	In	I	Indicating whether the soil is drained (= 0) or undrained (= 1).
<i>X, Y, Z</i>	In	R	Global coordinates of stress integration point.
<i>Time0, dTime</i>	In	R	Time at end of last step and time increment.
<i>Props</i>	In	R(:)	Array containing material properties.
<i>Sig0, Swp0, dEps</i>	In	R(:)	Stress and excess pore pressure from last step and strain increment.
<i>iPrjDir, iPrjLen</i>	In	I	Integers used for debugging.
<i>StVar0</i>	In/Out	R(:)	Initial value of state parameters, output in first step and input in all others.
<i>D</i>	Out	R(:,:)	Stiffness matrix effective if <i>IDTask</i> = 3 or elastic if <i>IDTask</i> = 6.
<i>BulkW</i>	Out	R	Bulk modulus of water for stress point.
<i>Sig, Swp, StVar</i>	Out	R(:)	Stress state, excess pore pressure and state variables.
<i>iPl</i>	Out	I	Plastic indicator. 0 = No plasticity, 1 = MC failure, 2 = Tension cut-off, 3 = Cap hardening, 4 = Cap friction, 5 = Friction hardening.
<i>nStat, iAbort</i>	Out	I	Number of state variables and abort parameter (1 = abort).
<i>NonSym, iStrsDep, iTimeDep, iTang</i>	Out	I	D matrix attributes: Symmetric, stress-dependent, time-dependent, tangent stiffness. 1 = true and 0 = false.

**Table E.1.** Variables used in the exchange of information between PLAXIS and the user defined subroutine. I = Integer, R = Real value, R(:) = Real value array.

In Fortran all variables used have to be declared, and for the subroutine to function with PLAXIS, the data type of the variables need to correspond exactly to table E.1. All the variables are listed and explained in detail in the PLAXIS material model manual Brinkgreve et al. [2012]. The calling sequence of the subroutine is,

```
1 subroutine User_Mod(IDTask, iMod, IsUndr, iStep, iTer, iEl, Int, X, Y, Z,
    Time0, dTime, Props, Sig0, Swp0, StVar0, dEps, D, BulkW, Sig, Swp,
    StVar, ipl, nStat, NonSym, iStrsDep, iTimeDep, iTang, iPrjDir,
    iPrjLen, iAbort)
```

The order of the variables is essential for the exchange of information to work properly. In the subroutine, local variables can furthermore be freely used to do calculations.

The 6 tasks of the subroutine are explained in detail along with the variables used in each task in the following subsections.

### E.3.1 IDTask = 1 - Initialising state parameters

In the first task the state parameters of the UDSM are initialised in the array *StVar0*, which is thus an output from task 1. This task is only called by PLAXIS in the first load step, since it defines the starting point for the state variables. An example could be the effective mean stress  $p'$  or the deviatoric stress  $q$ . All PLAXIS calculations begin with an initial phase, where the in-situ stress state is established, e.g. through a  $K_0$ -procedure or gravitational loading. In this initial phase the state variables are not established, as they are dependent of the material model, whereas the initial phase calculation is not. Therefore, if  $p$  and  $q$  are needed in the material model, they need to be calculated in the first load step. A code example is shown below.

```
1 If (IDTask == 1) Then ! Initialize state variables
2     p = (Sig0(1) + Sig0(2) + Sig0(3))/3 ! Compression is negative
3     StVar0(1) = p
4 End If ! IDTask = 1
```

All variables need to be defined in the beginning of the subroutine, here the local variable  $p$  is a real value. Note that everything written after an exclamation mark is ignored by the compiler, and can therefore be used to input comments.

In all load steps after the first one, the *StVar0* vector contains the state variables from the previous steps and thus turns into an input given from PLAXIS.

### E.3.2 IDTask = 2 - Calculating stress and pore pressure

In this task the main part of the subroutine calculation takes place. The main goal of the task is to provide a stress state that obeys the material model from a given strain increment. The main input arrays used in task 2 is the previous stress state in *Sig0*, the material properties in *Props* and the stress increment *dEps*. The stress update procedure is as follows,

- Calculation of elastic stress predictor based on *Sig0*, *dEps* and the elastic stiffness matrix  $D^e$ .
- Test of predicted stress state against the yield criterion applied.
- If the stress state is elastic, the elastic predictor stress is the updated stress state used as output *Sig*.
- If the stress state is plastic, the stress state is returned to the yield surface using a return algorithm and the stress state is output as *Sig*.
- If the model is undrained the excess pore pressure is calculated using a very large bulk modulus for water and the strain increment *dEps*.

An example of the main code for the task, where a Mohr-Coulomb model is used is given below.

```
1 If (IDTask == 2) Then ! Calculate stresses based on elastic predictor
   and then stress-update
2
3     ! Calculating elastic stiffness matrix
4     call DlinElas(E,nu,nsigma,De,Dinv)
```

```

5
6      ! Elastic stress predictor
7      Do j = 1,6
8          Sig_p(j)=Sig0(j)
9          Do i = 1,6
10             Sig_p(j) = Sig_p(j) + De(j,i)*dEps(i)
11         end do
12     end Do
13
14     ! Stress return algorithm
15     call
16         MohrCoulombStressReturn(Sig_p,nsigma,PlasPar,De,Dinv,Sig,Depc,region)
17
18     ! Plasticity indicator iPl
19     if (region == 0) then
20         ipl = 0
21     else
22         ipl = 1
23     end if
24
25     If (IsUndr == 1) Then ! If undrained, a large bulk modulus of
26         water is calculated to find excess pore pressure
27         g = E/(2*(1+nu)) ! Shear modulus
28         Nu_U = 0.495 ! Undrained Poissons' ratio
29         Fac = (1+Nu_U)/(1-2*Nu_U) - (1+nu)/(1-2*nu)
30         Fac = 2*g/3 * Fac
31         BulkW = Fac
32         dEpsV = dEps(1) + dEps(2) + dEps(3) ! Volumetric strain
33             increment
34         dSwp = BulkW * dEpsV
35         Swp = Swp0 + dSwp
36     Else
37         BulkW = 0 ! If drained, bulk modulus is zero
38         Swp = Swp0 ! And no change in pore pressure
39     end if
40
41 End If ! IDTask = 2

```

The subroutines *DLinElas* and *MohrCoulombStressReturn* are used to perform the main calculations of the task.

### E.3.3 IDTask = 3 - Effective stiffness matrix and bulk modulus

In task 3 the effective stiffness matrix should be calculated and given to the program. Several different stiffness matrices can be used, e.g. the full elastoplastic or the purely elastic matrix. The standard procedure used in PLAXIS however is to simply use the elastic stiffness matrix, which is easily calculated. This implies using more iteration steps to establish equilibrium, compared to using the full elastoplastic matrix. The

coding of the UDSM is shorter and simpler using the elastic matrix which is often preferable. In the code the subroutine *DLinElas* is thus simply called and the bulk modulus of water is calculated.

```

1 If (IDTask == 3) Then ! Calculated effective D and bulk modulus of water
2
3     ! Calculating elastic stiffness matrix
4     call DlinElas(E,nu,nsigma,D,Dinv)
5
6     If (IsUndr == 1) Then ! If undrained, a large bulk modulus of
7         water is calculated to find excess pore pressure
8         g = E/(2*(1+nu)) ! Shear modulus
9         Nu_U = 0.495 ! Undrained Poissons' ratio
10        Fac = (1+Nu_U)/(1-2*Nu_U) - (1+nu)/(1-2*nu)
11        Fac = 2*g/3 * Fac
12        BulkW = Fac
13
14    Else
15        BulkW = 0 ! If drained, bulk modulus is zero
16    end if
17
18 End If ! IDTask = 3

```

### E.3.4 IDTask = 4 - Return number of state variables

This task simply tells PLAXIS how many state variables are used in the model, and thus are to be transferred from one load increment to the next.

```

1 If (IDTask == 4) Then ! Initialize state variables
2     nStat = 2 ! Equal to two, if p and q are used
3 End If ! IDTask = 4

```

### E.3.5 IDTask = 5 - Matrix attributes

In task 5 the matrix attributes of the effective stiffness matrix are given to the calculation kernel in PLAXIS. The attributes determine the kind of iteration procedure used. When using a purely elastic stiffness matrix, the code is as shown below.

```

1 If (IDTask == 5) Then ! Matrix attributes
2     NonSym = 0 ! 1 for non-symmetric D-matrix
3     iStrsDep = 0 ! 1 for stress dependent D-matrix
4     iTang = 0 ! 1 for tangent D-matrix
5     iTimeDep = 0 ! 1 for time dependent D-matrix
6 End If ! IDTask = 5

```

### E.3.6 IDTask = 6 - Elastic stiffness matrix

Task 6 is simply giving PLAXIS the elastic stiffness matrix, which makes it identical to task 3 in the described case.

## E.4 Calculation Procedure in PLAXIS

As described earlier, the USDM enables PLAXIS to perform calculations using soil material models not readily available in PLAXIS. However, regardless of the material model, PLAXIS uses the same calculation procedure and have equal demands to what the material model needs to deliver. This procedure will be explained in the following based on Krabbenhøft [2002].

### E.4.1 General Procedure

In general finite element theory, the systems of equations can be formulated as equation (E.3).

$$\mathbf{f} = \mathbf{K} \mathbf{u} \quad (\text{E.3})$$

The stiffness matrix is given as seen in equation (E.4).

$$\mathbf{K} = \int_{\Omega} \mathbf{B}^T \mathbf{D}_{ep} \mathbf{B} d\Omega \quad (\text{E.4})$$

Since the constitutive matrix  $\mathbf{D}_{ep}$  depends on the current stress state, the stiffness matrix  $\mathbf{K}$  is non-linear. Because of this fact, the load is applied in increments utilizing instead the tangent stiffness matrix  $\mathbf{K}_t$  as seen in equation (E.5) compared to equation (E.3).

$$\Delta \mathbf{f} = \mathbf{K}_t \Delta \mathbf{u} \quad (\text{E.5})$$

From this approximation of the real elasto-plastic behaviour, the residual forces can be calculated. To have equilibrium, the residual forces must be  $\mathbf{r} = 0$ , meaning that the internal forces  $\mathbf{q}$  must be balanced by the externally applied load  $\mathbf{f}$ . If this is not the case, the residual forces  $\mathbf{r}$  are applied as an external load which will cause another strain increment and a corresponding stress increment. This iterative procedure must be repeated until the residual forces are sufficiently small, and can be carried out by means of a Newton-Raphson scheme.

### E.4.2 Iteration Procedure

In order for PLAXIS to determine a solution for the given problem, it utilizes a iterative solution scheme known as Newton-Raphson. Unlike explicit methods like the Forward Euler-method, the Newton-Raphson solution involves iteration to find equilibrium in each load step. The Newton-Raphson scheme can be formulated in different ways depending on the number of times, the stiffness is updated.

1. Full Newton-Raphson: Stiffness is updated in each iteration. Results in high convergence (and thus few iterations) but each iteration is very time consuming.
2. Modified Newton-Raphson: Stiffness is updated in each load step. Results in lower convergence (and thus more iterations) but each iteration is much less time consuming.
3. Initial Stiffness Newton-Raphson: The stiffness is never updated, ie. the initial stiffness is used all the way through. Results in low convergence (and thus many iterations) but each iteration is even less time consuming.

In PLAXIS, the Full or Modified schemes are used depending on the properties of the constitutive matrix (or material stiffness matrix, as it is named in PLAXIS)  $\overline{\overline{D}}_{ep}$ . Considering table E.1,  $iStrDep = 1$  determines that the material stiffness matrix is stress-dependent and thus must be decomposed in each load step considering the current stress state. This is utilized in the Modified Newton-Raphson scheme.  $iTang = 1$  determines that the material stiffness matrix is a tangent stiffness matrix to be used in a Full Newton-Raphson scheme [Brinkgreve et al., 2012].

#### E.4.2.1 Arc-length control

A way of improving the iteration within a Newton-Raphson scheme is to utilize an arc-length method. The arc-length method is applied as default in PLAXIS. The way arc-length control works is to constrain the residual force in the force-displacement space by a circular arc. This constraint enables the scheme to converge towards equilibrium much faster. The principle is shown in figure E.2.

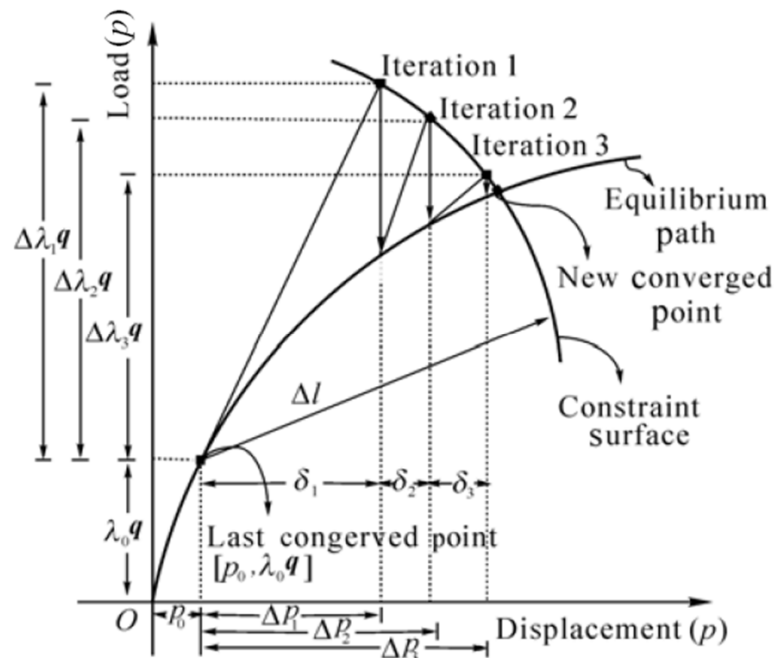
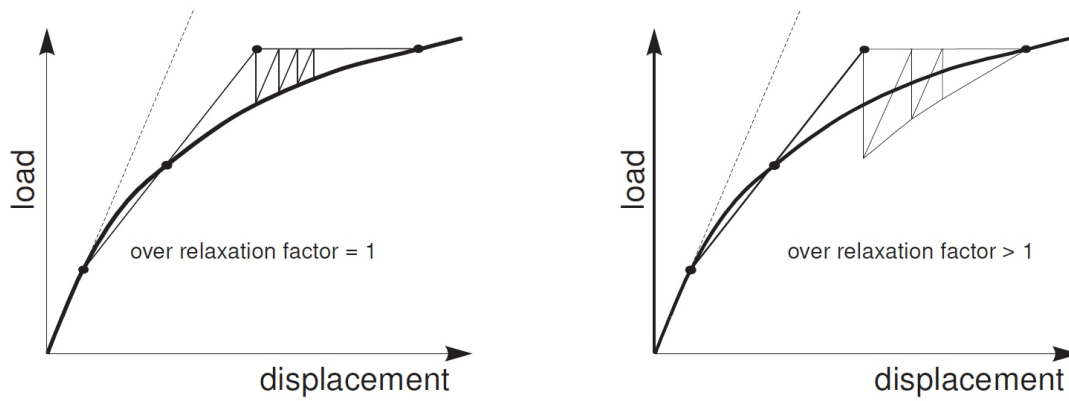


Figure E.2. The principle of arc-length control.

#### E.4.2.2 Over-relaxation

At each iteration the equilibrium error of the system of equations is used to calculate the load/displacement of the next iteration. By applying the error in each iteration, the system slowly converges to the exact solution. Over-relaxation is an overestimation of the equilibrium error, with the purpose of faster reaching the correct load/displacement. The over-relaxation is controlled by the over-relaxation factor, which is by default set to 1.2. The concept of the over-relaxation method can be seen in figure E.3. [Brinkgreve et al., 2012]



*Figure E.3.* A normal iteration procedure on the left and the iteration procedure with over-relaxation used on the right. [Brinkgreve et al., 2012]

#### E.4.2.3 Line-search

The line search algorithm can be seen as a further development of the over-relaxation method. The exact algorithm is not thoroughly explained in the PLAXIS documentation, however the concept is that the correction used in the next iteration is a scaled version of the equilibrium error, such that the system converges faster. The scaling is however not constant, as in the over-relaxation method.

The method is recommended in Brinkgreve et al. [2012] to be used only in problems without severe non-linearities. The method has with success been applied in all models of this project.

# F Source Code for UDSM

---

This appendix contains the source code for the PLAXIS 3D implementation of the user defined soil model. The code contains only the subroutine *User\_mod*, and not the entire source code used in the material model. The inclusion of the source code is meant as a help for future projects involving a UDSM implementation in PLAXIS 3D.

```
1 subroutine User_Mod(IDTask, iMod, IsUndr, iStep, iTer, iEl, Int, X, Y, Z,
   Time0, dTime, Props, Sig0, Swp0, StVar0, dEps, D, BulkW, Sig, Swp,
   StVar, ipl, nStat, NonSym, iStrsDep, iTimeDep, iTang, iPrjDir,
   iPrjLen, iAbort)
2 !
3 ! Mohr-Coulomb curved criterion linear-elastic-perfectly-plastic user
   defined soil model for PLAXIS 3D
4 ! Material-model written by Johan Clausen and ported to PLAXIS
5 ! by Martin Underlin Østergaard and Bjørn Staghøj Knudsen as a part of a
   Master Thesis
6 ! Aalborg University Civil and Structural Engineering 2013
7 !
8 ! Depending on IDTask, 1 : Initialize state variables
9 ! 2 : Calculate stresses,
10 ! 3 : Calculate material stiffness matrix
11 ! 4 : Return number of state variables
12 ! 5 : Inquire matrix properties return, switch for
   non-symmetric D-matrix, stress/time dependent matrix
13 ! 6 : Calculate elastic material stiffness matrix
14 ! Arguments:
15 ! I/O Type
16 ! IDTask I I : see above
17 ! iMod I I : model number (1..10)
18 ! IsUndr I I : =1 for undrained, 0 otherwise
19 ! iStep I I : Global step number
20 ! iter I I : Global iteration number
21 ! iel I I : Global element number
22 ! Int I I : Global integration point number
23 ! X I R : X-Position of integration point
24 ! Y I R : Y-Position of integration point
25 ! Z I R : Z-Position of integration point
26 ! Time0 I R : Time at start of step
27 ! dTime I R : Time increment
28 ! Props I R() : List with model parameters, defined in useradddf.f90
29 ! Sig0 I R() : Stresses at start of step
30 ! Swp0 I R : Excess pore pressure start of step
31 ! StVar0 I R() : State variable at start of step
32 ! dEps I R() : Strain increment
33 ! D I/O R(,) : Material stiffness matrix
34 ! BulkW I/O R : Bulkmodulus for water (undrained only)
35 ! Sig 0 R() : Resulting stresses
36 ! Swp 0 R : Resulting excess pore pressure
```

```

37 ! StVar 0 R() : Resulting values state variables
38 ! iPl 0 I : Plasticity indicator
39 ! nStat 0 I : Number of state variables
40 ! NonSym 0 I : Non-Symmetric D-matrix ?
41 ! iStrsDep 0 I : =1 for stress dependent D-matrix
42 ! iTimeDep 0 I : =1 for time dependent D-matrix
43 ! iAbort 0 I : =1 to force stopping of calculation
44 ! iPrjDir I I : Input from PLAXIS, not used
45 ! iPrjLen I I : Input from PLAXIS, not used
46
47 implicit none
48 ! Defining variables
49 ! Arrays
50 real(8) :: Props(8), Sig0(20), dEps(12) ! Input
51 real(8) :: StVar0(1) ! In/Output depending on value of IDTask
52 real(8) :: D(6,6), Sig(6), StVar(1), Depc(6,6) ! Out
53 ! Integers / Reals
54 integer :: iMod, IDTask, istep, iter, iel, isundr, Int, iPrjLen, iPrjDir
    ! Input
55 integer :: iPl, nstat, nonsym, istrsdep, itang, itimedep, iAbort ! Output
56 real(8) :: x, y, z, time0, dtime, swp0 ! Input
57 real(8) :: bulkw, swp ! Output
58 ! Local variables
59 real(8) :: E, nu, nu_U, fac, dEpsV, dSwp, c0, k0, m0, a1, b1, apex, g
60 real(8), parameter :: pi = 3.1415926535897932_8
61 real(8) :: Dinv(6,6), Sig_p(6), De(6,6), PlasPar(6)
62 integer :: i, j, nsigma, region, npar
63 character*8 PlasType
64
65 ! Debug variables
66 integer :: debug, IsOpen, ios
67 character*255 :: fName, filename
68 ! Logical IsOpen
69 Data IsOpen / 0 /
70 Save IsOpen
71
72 ! DLL Export declaration
73 !DEC$ ATTRIBUTES DLLEXPORT, STDCALL, REFERENCE :: User_Mod
74
75 !---- Explicit interfaces -----
76 interface
77 subroutine
    CurvMCStressReturn(Sigma,nsigma,nu,PlasPar,D,Dinv,Sigma_up,Depc,region)
78 integer(4), intent(in) :: nsigma
79 real(8), intent(in) :: Sigma(nsigma), PlasPar(6),
    nu
80 real(8), intent(in) :: D(nsigma,nsigma),
    Dinv(nsigma,nsigma)

```

```

81
82         real(8), intent(out)    :: Sigma_up(nsigma),
           Depc(nsigma,nsigma)
83         integer(4), intent(out) :: region
84     end subroutine CurvMCStressReturn
85         !---
86     subroutine DlinElas(E,nu,nsigma,D,Dinv)
87         integer(4), intent(in)  :: nsigma
88         real(8), intent(in)     :: E, nu
89
90         real(8), intent(out)    :: D(nsigma,nsigma)
91         real(8), intent(out), optional :: Dinv(nsigma,nsigma)
92     end subroutine DlinElas
93 end interface
94 !-----
95
96 iAbort = 0 ! Do not abort
97 nsigma = 6 ! 3D stress state
98
99 ! Defining material parameters
100 ! The Curved Mohr-Coulomb criterion is defined by
101 !

$$f = k_0 \cdot \text{sigP}(1) - \text{sigP}(3) - c_0 \cdot (1 - \exp(a_1 \cdot (\text{sigP}(1) - \text{apex}) / c_0)) - \text{apex} \cdot (k_0 - 1) = 0$$

102 ! and the corresponding plastic potential
103 !

$$g = m_0 \cdot \text{sigP}(1) - \text{sigP}(3) - c_0 \cdot (1 - \exp(b_1 \cdot (\text{sigP}(1) - \text{apex}) / c_0))$$

104
105 E = Props(1) ! Modulus of elasticity
106 nu = Props(2) ! Poissons ratio
107 k0 = Props(3) ! Friction parameter
108 c0 = Props(4) ! Cohesive parameter
109 a1 = Props(5) ! Curvature parameter
110 apex = Props(6) ! Apex position, apex = 0 for non-cohesive material
111 m0 = Props(7) ! Friction parameter in plastic potential
112 b1 = Props(8) ! Curvature parameter in plastic potential
113
114 PlasPar = [k0, c0, a1, apex, m0, b1]
115
116 Select Case (iMod) ! Selecting Material model
117 Case (1) ! MC
118
119 ! Following procedure from PLAXIS manual
120 If (IDTask == 1) Then ! Initialize state variables
121     ! Nothing to do here *flies away*
122 End If ! IDTask = 1
123
124 If (IDTask == 2) Then ! Calculate stresses based on elastic predictor
           and the stress-update
125     ! Building stiffness matrices

```

```

126  call DlinElas(E,nu,nsigma,De,Dinv)
127
128  ! Elastic stress predictor
129  Do j = 1,6
130      Sig_p(j)=Sig0(j)
131      Do i = 1,6
132          Sig_p(j) = Sig_p(j) + De(j,i)*dEps(i)
133      end do
134  end Do
135  ! Calling stress return algorithm using elastic predictor
136  call
137      CurvMCStressReturn(Sig_p,nsigma,nu,PlasPar,De,Dinv,Sig,Depc,region)
138
139  ! Plasticity indicator iPl
140  if (region == 0) then
141      ipl = 0
142  else
143      ipl = 1
144  end if
145
146  If (IsUndr == 1) Then ! If undrained, a large bulk modulus of water
147      is calculated to find excess pore pressure
148      g = E/(2*(1+nu)) ! Shear modulus
149      Nu_U = 0.495 ! Undrained Poissons' ratio
150      Fac = (1+Nu_U)/(1-2*Nu_U) - (1+nu)/(1-2*nu)
151      Fac = 2*g/3 * Fac
152      BulkW = Fac
153      dEpsV = dEps(1) + dEps(2) + dEps(3) ! Volumetric strain increment
154      dSwp = BulkW * dEpsV
155      Swp = Swp0 + dSwp
156
157  Else
158      BulkW = 0 ! If drained, bulk modulus is zero
159      Swp = Swp0 ! And no change in pore pressure
160  end if
161
162  End If ! IDTask = 2; get stresses
163
164  If (IDTask == 3) Then ! Calculate effective stiffness matrix
165      ! The effective matrix can be either the elastic or the full
166      elastoplastic matrix. Here the elastic is used
167      call DlinElas(E,nu,nsigma,D,Dinv)
168
169  If (IsUndr == 1) Then ! If undrained, a large bulk modulus of water
170      is calculated to find excess pore pressure
171      g = E/(2*(1+nu)) ! Shear modulus
172      Nu_U = 0.495 ! Undrained Poissons' ratio
173      Fac = (1+Nu_U)/(1-2*Nu_U) - (1+nu)/(1-2*nu)
174      Fac = 2*g/3 * Fac
175      BulkW = Fac

```

```

170     Else
171         BulkW = 0 ! If drained, bulk modulus is zero
172     end if
173
174 End If ! IDTask = 3; get D^ep and BulkW
175
176 If (IDTask == 4) Then ! Number of state parameters
177     nStat = 0 ! No state parameters are used in the LE-model
178 End If ! IDTask = 4
179
180 If (IDTask == 5) Then ! Matrix attributes
181     NonSym = 0 ! 1 for non-symmetric D-matrix
182     iStrsDep = 0 ! 1 for stress dependent D-matrix
183     iTang = 0 ! 1 for tangent D-matrix
184     iTimeDep = 0 ! 1 for time dependent D-matrix
185 End If ! IDTask = 5
186
187 If (IDTask == 6) Then ! Elastic stiffness matrix
188     call DlinElas(E,nu,nsigma,D,Dinv)
189 End If ! IDTask = 6
190
191 End Select ! End selection of material model
192
193 End Subroutine ! End subroutine

```



# G Laboratory Details

In this appendix various subjects regarding the laboratory work will be presented.

## G.1 Laboratory setup

In this section the laboratory setup will be explained in detail.

### G.1.1 Model Bucket

The model bucket used in the tests is shown with dimensions in figure G.1.

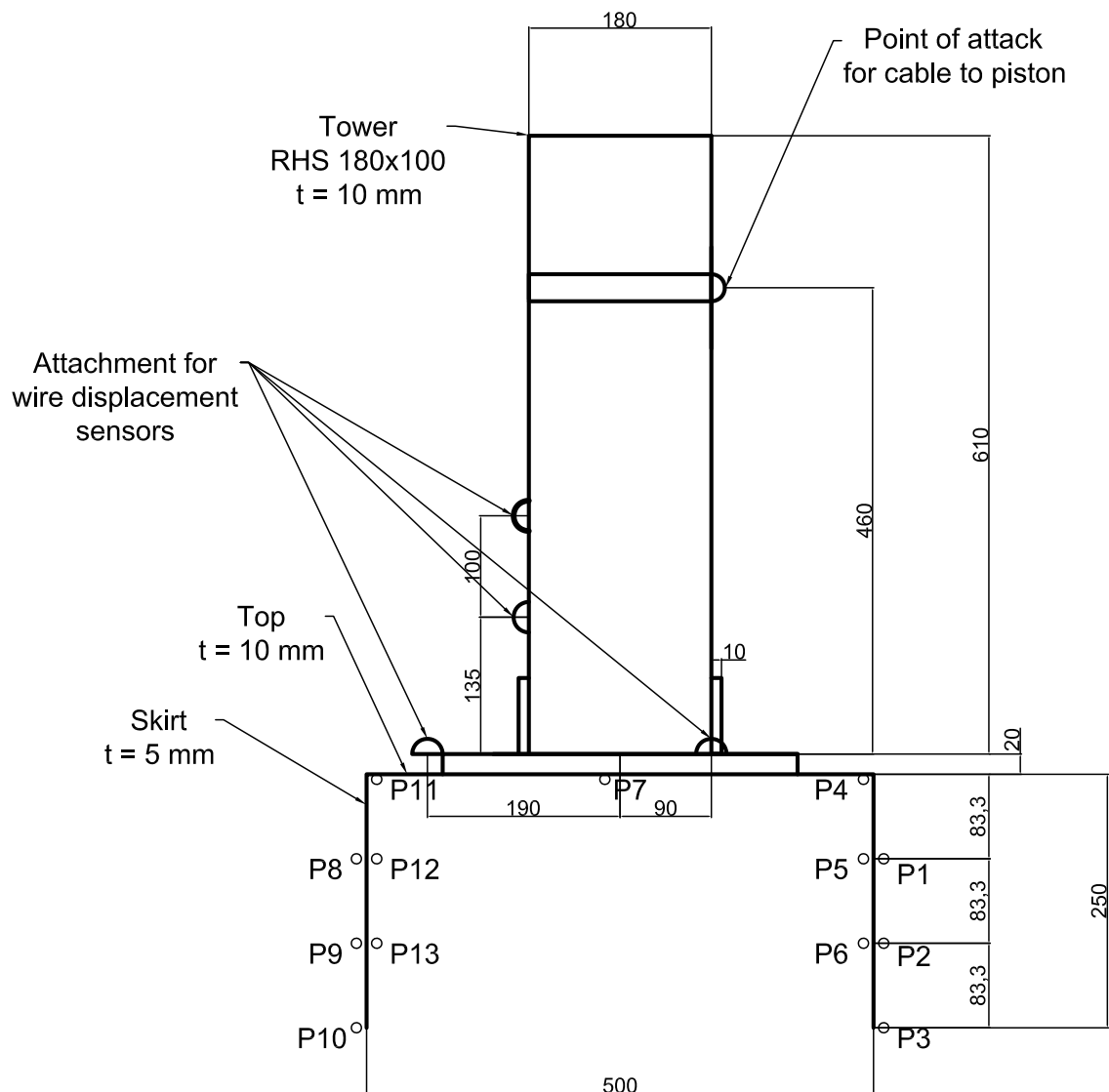


Figure G.1. Sketch of the bucket used in the tests, shown with dimensions.

The bucket is a further development of an original model, where the steel thickness proved to be too small to withstand the pore pressures during a fast loading sequence causing the bucket skirt to deform heavily. From the earlier experiences two model buckets were produced with a diameter of 500 mm and a skirt length of respectively

250 and 500 mm. The latter is not used in the test in this project due to shortage of time in the laboratory.

The tower is designed to be able to withstand a force of 100 kN at an eccentricity of 500 mm, i.e. a moment of 50 kNm. A 180x100 mm RHS profile is used for the tower. At the bottom the flanges are reinforced by an extra plate of 10 mm thickness welded to the short side of the profile. The bottom of the tower is a 40 mm round steel plate with 8 holes for bolts used to attach the tower to the bucket itself.

The lid of the bucket is a 10 mm thick steel plate and the skirt is of 5 mm thickness. On the bucket 13 pore pressure gauges are installed at different relevant positions. The pressure gauges are from HBM and have a range of either  $\pm 5$  or  $\pm 10$  bar. 6 gauges are placed on the outside of the skirt on the plane of attack for the force. Three are placed on the side closest to and three are placed farthest from to the point of attack for the force. The outside gauges are placed at respectively 83.3 mm, 166.7 mm and 250 mm depth from the lid. Inside the bucket 7 gauges are placed at respectively 0 mm, 83.3 mm and 166.7 mm from the lid. The last gauge is placed directly beneath the middle of the tower. Refer to figure G.1 for the positions. A picture of the bucket with the tower installed is seen in figure G.2.

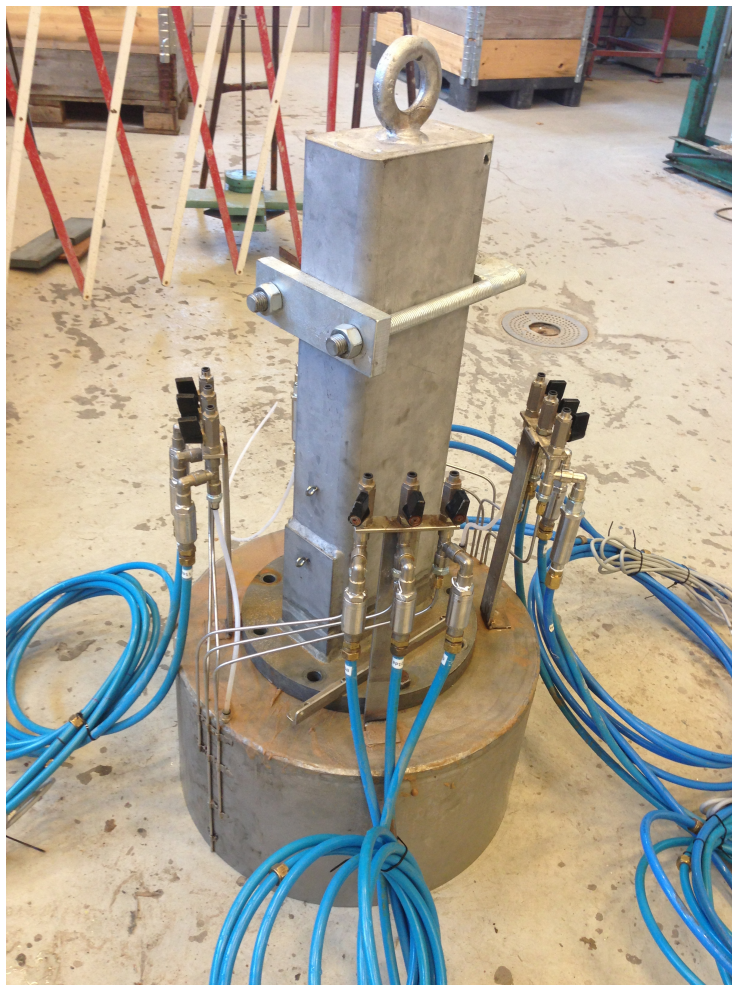


*Figure G.2.* The model bucket with the tower installed.

## G.1.2 Schematic overview

Figure G.3 contains an overview of the entire test setup.

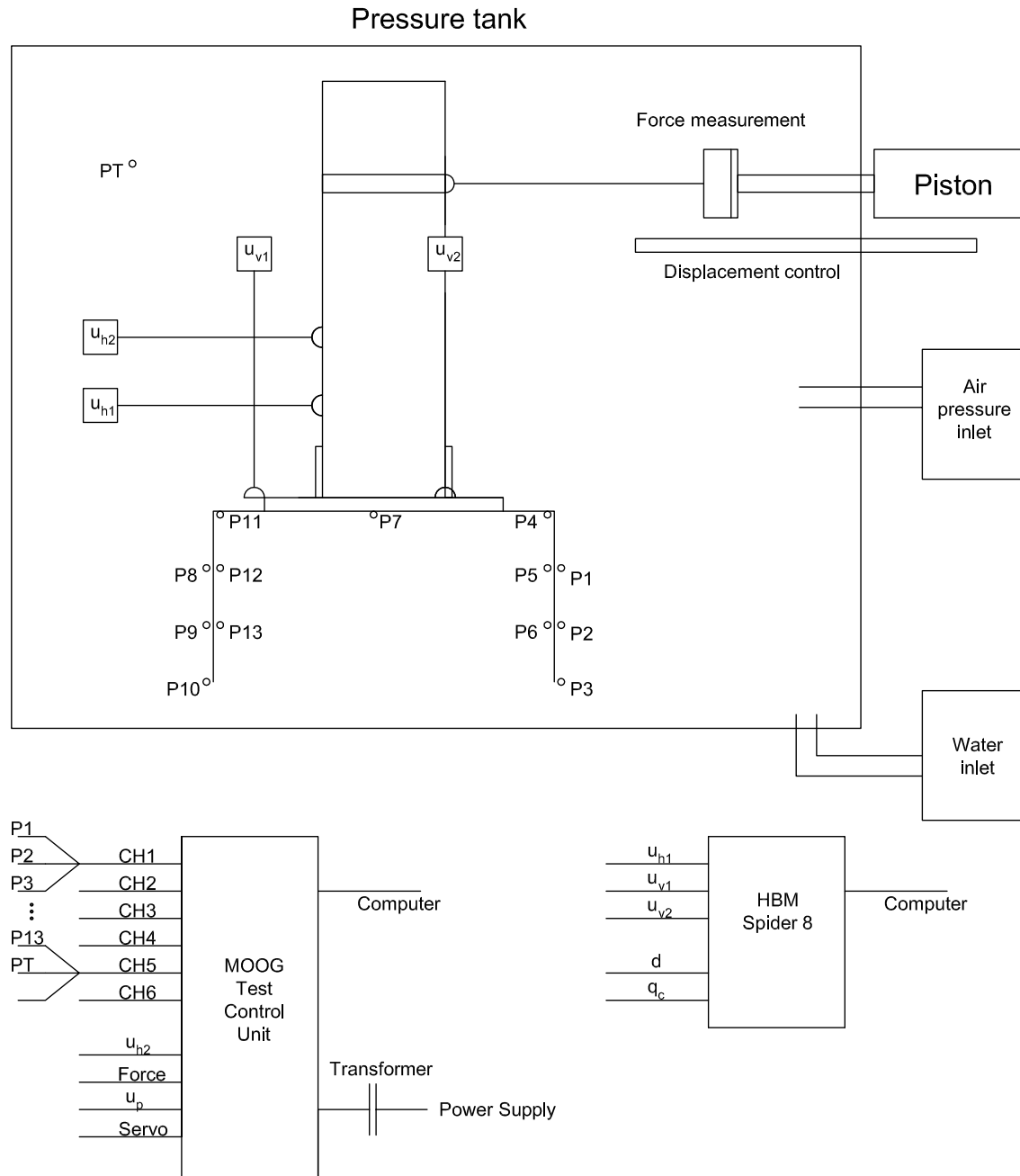


Figure G.3. Overview of the test setup.

The setup is controlled by a computer connected with a Test Control Unit (TCU) from MOOG. The TCU controls the hydraulics in the piston through either displacement  $u_p$  or via force  $F_p$ . In the used setup, only displacement control is used. The piston is connected to the tower of the bucket with a removable steel cable.

A total of 14 pressure gauges are used in the setup, these are named PP01-PP13 and PT and are all connected to the TCU, which is also used to sample data. The first 13 pressure gauges are placed on different places on the bucket and are used to measure the pore pressure in the sand. The PT gauge measures the air pressure inside the pressure tank,

and is used to confirm the absolute air pressure applied via the compressor. Besides the force measurement, displacement of the piston and the 14 pressure gauges an additional horizontal displacement sensor  $u_{h2}$  is connected to the TCU. This measurement is used to synchronize the time step between the TCU and the HBM Spider.

The three remaining displacements  $u_{h1}$ ,  $u_{v1}$  and  $u_{v2}$  are all connected to a HBM Spider data acquiring box also connected to a computer. It was not possible to do data acquiring of all signals with the TCU, which is why the HBM Spider was used as a secondary unit. Furthermore the HBM Spider is also used when performing the mini-CPT tests to measure the depth  $d$  and the cone resistance  $q_c$ . A total list of measured entities are shown in table G.1.

Pressure gauges [kPa]	Displacement sensors [mm]	Forces [N]
PT	$u_{h1}$	$F_p$
PP01	$u_{h2}$	$q_c$
PP02	$u_{v1}$	
PP03	$u_{v2}$	
PP04	$u_p$	
PP05	$d$	
PP06		
PP07		
PP08		
PP09		
PP10		
PP11		
PP12		
PP13		

*Table G.1.* Table of measured signals in the setup

The air pressure inlet is controlled via two gauges placed next to a small buffer tank. The first gauge is set to 200 kPa (2.0 bar) and the compressor builds up the pressure in the buffer tank. From the buffer tank another gauge controls the pressure let into the pressure tank, this gauge is also set to 200 kPa but is adjusted using the TP measurement. The build up takes approximately 1 hour in which the pressure is constantly monitored by the PT measurement. Due to the large amount of tubes with signal wires connected through small holes in the tank, the setup is not completely hermetic and small volumes of air is able to escape the tank. After a while an equilibrium is formed and the pressure in the tank is stable. The pressure is left in the tank over night, for a completely homogeneous pressure state in the sand volume to be obtained.

The water inlet is used to loosen the sand after a test before compacting it again with the vibrator. The water inlet is connected to a large water tank placed approximately 1.5 meters higher than the sand surface in the tank. The height difference makes it possible to produce a flow through the bottom of the tank with a certain gradient, adjusted by opening a valve until the needed gradient is obtained. The gradient used

when loosening the sand is  $i = 0.9$  based on experience from earlier tests.

$$i = \frac{\Delta h}{d_{\text{sand}}}. \quad (\text{G.1})$$

$i$	Gradient of water flow [-]
$\Delta h$	Difference in pressure height [m]
$d_{\text{sand}}$	Greatness of sand layer = 0.60 m

$\Delta h$  is measured by a vertical tube at the inlet to the tank, and should from equation (G.1) be equal to 0.55 m. The loosening is done over a period of 5 minutes.

## G.2 Model laws - Scaling parameters

When performing model tests, some considerations need to be done regarding the scaling effects, as it is often not possible to do testing on full-size models. In order to do correct scaling of physical phenomena, three basic rules must be obeyed,

1. Geometric similarity
2. Kinematic similarity
3. Dynamic similarity

These three rules will be explained and using general physical considerations, the scaling factors are derived in the following. Generally a scaling factor is on the form shown in equation (G.2).

$$X_N = \lambda_X X_M. \quad (\text{G.2})$$

$X_N$	Physical entity in the nature
$X_M$	Scaled physical entity in the model
$\lambda_X$	Scaling factor of entity X

### G.2.1 Geometric similarity

Geometric similarity means direct similarity between every geometric quantity in the model and in nature. This can be expressed as,

$$L_N = \lambda_L L_M. \quad (\text{G.3})$$

$L_N$	Lengths in the nature [m]
$L_M$	Scaled lengths in the model [m]
$\lambda_X$	Length scale [-]

From this the area scale and the volume scale can be directly derived as  $\lambda_L^2$  and  $\lambda_L^3$  respectively. For every geometric entity, this scaling factor must be the same for the similarity rule to be valid. In the model the bucket foundation has a diameter of 0.5

meter, which compared to a nature-size foundation of 15 m gives a scaling factor of  $\lambda_L = 30$ .

In principle the geometric similarity applies for all geometric entities, and as such the grain size should also be scaled properly for the principle to be valid.

### G.2.2 Kinematic Similarity

The kinematic similarity requires similarity between the velocity vectors of the model and the nature phenomenon. This applies both to the magnitude and the directionality of the velocity. All velocity vectors at similar points between the model and nature should as a consequence be parallel. The velocity scale can be defined analogous to the length scale as,

$$\vec{v}_N = \lambda_V \vec{v}_M. \quad (G.4)$$

$\vec{v}_N$	Velocity in the nature [m/s]
$\vec{v}_M$	Scaled velocity in the model [m/s]
$\lambda_V$	Velocity scale [-]

By using both geometric and kinematic similarity, the time scale can be defined including the definition of velocity as,

$$\lambda_T = \frac{t_N}{t_M}, \quad (G.5)$$

$$\vec{v} = \frac{d\vec{x}}{dt} \Rightarrow \frac{d\vec{x}_N}{dt_N} = \lambda_V \frac{d\vec{x}_M}{dt_M}, \quad (G.6)$$

$$\Rightarrow d\vec{x}_N = \lambda_L d\vec{x}_M \Rightarrow \frac{\lambda_L d\vec{x}_M}{dt_N} = \lambda_V \frac{d\vec{x}_M}{dt_M}, \quad (G.7)$$

$$\Rightarrow \frac{dt_N}{dt_M} = \frac{\lambda_L}{\lambda_V} = \lambda_T. \quad (G.8)$$

$t_N$	Time period in the nature [s]
$t_M$	Scaled time period in the model [s]
$\lambda_T$	Time scale [-]

### G.2.3 Dynamic similarity

Dynamic similarity is the principle of similar scaling of all forces. A particle subjected to a force at a certain in the model and in nature should thus be scaled similar between all particles. As the other scales, the force scale is defined as,

$$\lambda_F = \frac{F_N}{F_M}. \quad (G.9)$$

$F_N$	Force in the nature [N]
$F_M$	Scaled force in the model [N]
$\lambda_F$	Force scale [-]

## G.2.4 Scaling considerations

In scaling a geotechnical experiment, both the soil and the water in the pores of the soil volume should be considered. The soil can be considered as being a continuum in which motion takes places, and is thus subject to obey Newtons 2nd law. The water in the pore is a flow problem, where the permeability and the viscosity of the fluid needs to be investigated. For the soil continuum, the scaling factors of the forces and stresses can be found via the Cauchy's Stress equations. The following formulation can be derived by taking equilibrium of a continuum element and applying Newtons 2nd law,

$$\frac{\partial \sigma_{ij}}{\partial x_j} + \rho g_i - \rho \frac{\partial^2 u_i}{\partial t^2} = 0. \quad (G.10)$$

Equation (G.10) can be formulated both in the model and in nature,

$$\frac{\partial \sigma_{ij,N}}{\partial x_{j,N}} + \rho_N g_{i,N} - \rho_N \frac{\partial^2 u_{i,N}}{\partial t_N^2} = 0, \quad (G.11)$$

$$\frac{\partial \sigma_{ij,M}}{\partial x_{j,M}} + \rho_M g_{i,M} - \rho_M \frac{\partial^2 u_{i,M}}{\partial t_M^2} = 0. \quad (G.12)$$

Introducing the stress scale  $\lambda_\sigma$ , the gravity scale  $\lambda_g$  and the density scale  $\lambda_\rho$  analogous to the other scales equation (G.11) is rewritten to,

$$\frac{\partial \sigma_{ij,M}}{\partial x_{j,M}} \frac{\lambda_\sigma}{\lambda_L} + \rho_N \lambda_\rho g_{i,M} \lambda_g - \rho_N \lambda_\rho \frac{\partial^2 u_{i,M}}{\partial t_M^2} \frac{\lambda_L^2}{\lambda_T^2} = 0, \quad (G.13)$$

$$\Rightarrow \frac{\partial \sigma_{ij,M}}{\partial x_{j,M}} + \frac{\lambda_L}{\lambda_\sigma} \lambda_\rho \lambda_g \rho_N g_{i,M} - \frac{\lambda_L}{\lambda_\sigma} \lambda_\rho \frac{\lambda_L}{\lambda_T^2} \rho_N \frac{\partial^2 u_{i,M}}{\partial t_M^2} = 0. \quad (G.14)$$

Comparing equations (G.12) and (G.14), a relation between the scaling factors can be made,

$$\frac{\lambda_L}{\lambda_\sigma} \lambda_\rho \lambda_g = \lambda_\rho \frac{\lambda_L}{\lambda_\sigma} \frac{\lambda_L}{\lambda_T^2} = 1. \quad (G.15)$$

From equation (G.15) the stress scale and thereby the force scale can be derived as,

$$\lambda_\sigma = \lambda_\rho \lambda_g \lambda_L \Rightarrow \lambda_F = \lambda_\sigma \lambda_L^2 = \lambda_\rho \lambda_g \lambda_L^3. \quad (G.16)$$

The earlier defined time and velocity scale in equation (G.8) can be further expanded by using equation (G.15),

$$\frac{\lambda_L}{\lambda_\sigma} \lambda_\rho \lambda_g = \lambda_\rho \frac{\lambda_L}{\lambda_\sigma} \frac{\lambda_L}{\lambda_T^2} \Rightarrow \lambda_T = \lambda_g^{-\frac{1}{2}} \lambda_L^{\frac{1}{2}}, \quad (G.17)$$

$$\lambda_V = \frac{\lambda_L}{\lambda_T} = \lambda_g^{\frac{1}{2}} \lambda_L^{-\frac{1}{2}}. \quad (G.18)$$

All the scaling factors derived from assuming the soil is a continuum is summarized in table G.2.

The dissipation of pore water in the sand is a flow problem, and is thus characterized by the permability of the soil and the viscosity of the fluid. Water flow through a medium is described by Darcy's law [Ovesen et al., 2009],

$$v = k i. \quad (G.19)$$

$v$	Velocity of water flow [m/s]
$k$	Hydraulic conductivity [m/s]
$i$	Gradient of flow [-]

The hydraulic conductivity is a measure of the ability of certain fluid at a certain temperature to flow through the soil with a certain permeability. The hydraulic conductivity is a function of the geometric parameters of the soil and the viscosity of the fluid,

$$k = K \frac{\gamma_w}{\eta} \quad , \quad \eta = \frac{\mu_v \gamma_w}{g} \quad \Rightarrow \quad k = K \frac{g}{\mu_v}. \quad (\text{G.20})$$

$K$	Permeability of soil [m <sup>2</sup> ]
$\gamma_w$	Unit weight of water [kN/m <sup>2</sup> ]
$\mu_v$	Kinematic viscosity of water [N s/m <sup>2</sup> ]
$g$	Acceleration of gravity [m/s <sup>2</sup> ]

The relation in equation (G.20) is valid as the flow in the soil is assumed to be laminar, which causes the flow resistance to be proportional with the kinematic viscosity. The kinematic viscosity of water is highly dependent of the temperature, and since laboratory tests are often conducted at approximately 20°C, whereas the groundwater in nature is typically 7-10°C, the difference in the viscosity of around 40% should be considered. From equation (G.20) Darcy's law can be written both for the nature and the model,

$$v_N = K_N \frac{g_N}{\mu_{v,N}}, \quad (\text{G.21})$$

$$v_M = K_M \frac{g_M}{\mu_{v,M}}. \quad (\text{G.22})$$

Introducing the velocity scale for the water flow  $\lambda_{v,f}$  and the definition of the time scale from equation (G.8),

$$v_N = \lambda_{v,f} v_M \quad \Rightarrow \quad \lambda_{v,f} = \frac{\lambda_K \lambda_g}{\lambda_{\mu_v}}, \quad (\text{G.23})$$

$$\lambda_{T,f} = \frac{\lambda_L}{\lambda_{v,f}} = \frac{\lambda_{\mu_v} \lambda_L}{\lambda_K \lambda_g}. \quad (\text{G.24})$$

The summary of all the derived scaling parameters are shown in table G.2.

Parameter	Derived scaling	Used scaling
Length	$\lambda_L$	$\lambda_L$
Time	$\lambda_g^{-\frac{1}{2}} \lambda_L^{\frac{1}{2}}$	$\lambda_L^{\frac{1}{2}}$
Velocity	$\lambda_g^{\frac{1}{2}} \lambda_L^{-\frac{1}{2}}$	$\lambda_L^{-\frac{1}{2}}$
Force	$\lambda_\rho \lambda_g \lambda_L^3$	$\lambda_L^3$
Stress/pressure	$\lambda_\rho \lambda_g \lambda_L$	$\lambda_L$
Time (flow)	$\frac{\lambda_{\mu_v} \lambda_L}{\lambda_K \lambda_g}$	$\lambda_L$
Velocity (flow)	$\frac{\lambda_K \lambda_g}{\lambda_{\mu_v}}$	1

*Table G.2.* Scaling parameters for the soil continuum and the pore water flow.

In table G.2 the derived scaling parameters and the actually used scaling parameters differ from each other. In order to do a correct scaling of the results, it should be possible to scale the acceleration of gravity, which is only possible in a centrifuge. Furthermore the viscosity of the water and the grain size distribution and density of the sand is not scaled correctly, which causes the scaling parameters of these to be neglected. The consequence of the incorrect scaling is that the results from the lab tests can not be directly extrapolated from the model to nature. This is however acceptable, since the primary object of the tests is to investigate the pore pressure development and load bearing capacity as a function of the loading velocity and not the numerical values of either the pressure or the load capacity.



# H Step-wise Description of Laboratory Work

This chapter contains a step-wise description of the laboratory work. The aim of the chapter is to make it easy to re-create the tests later on. The chapter will contain both descriptions and pictures of the phases in conducting the experiment.

## H.1 Preparation of the sand volume

### H.1.1 Applying a gradient

The first step of the test setup is to prepare the sand in the tank. To get the sand back to a zero-state an upwards gradient of 0.9 is applied by letting water flow from a tank situated above the water surface in the tank. The gradient is controlled with a nozzle as shown in figure H.1.

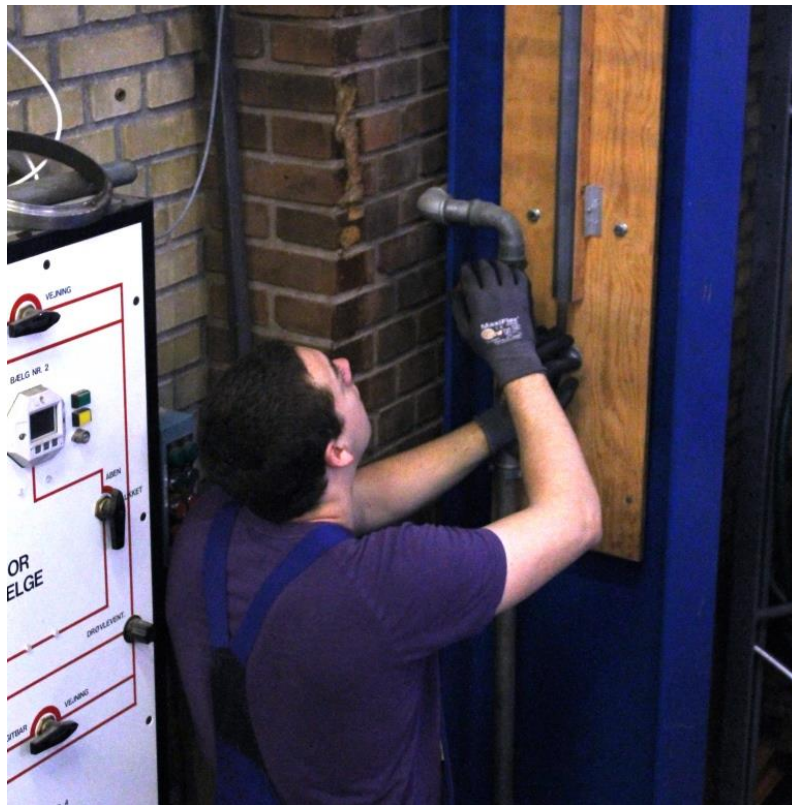


*Figure H.1.* Controlling the gradient via a nozzle.

Since the sand layer has a thickness of approximately 600 mm a gradient of 0.9 equals a pressure height of 0.55 m. At the nozzle a ruler is placed to measure this pressure height. The measurement is relative to the actual water level in the tank, which is shown when the nozzle is closed. To let water into the tank, the three nozzles in the bottom of the tank needs to be opened as well. After the loosening of the sand the water level in the tank should be approximately 60-70 mm above the sand. The water level can be adjusted by either letting water flow out with the bottom valves or letting water in through the side of the tank above the sand surface. When the water is let in above the

surface of the sand a metal plate is placed on top of the sand to avoid washing away sand at the inlet.

### H.1.2 Vibration of the sand

The goal of the vibration procedure is to create a sand volume that is densely packed, i.e. a relative density at around  $I_D = 0.85$ . This is achieved by vibrating the sand in a pattern previously determined by tests. 4 wooden plates are inserted into the tank, these plates have circular holes numbered 1 and 2. Firstly all number 1 holes are vibrated, secondly the number 2 holes. See figure H.2.



*Figure H.2.* The wooden plates used to control the vibration pattern.

The vibration is done with a vibration rod that is inserted slowly into the sand until a depth marked on the cable of the vibration rod. The rod is then slowly pulled up from the sand again. It is important that this is done slowly, in order to avoid pockets of air in the sand. See figure H.3.



*Figure H.3.* Vibrating the sand.

The gradient and vibration procedure may need to be redone twice, to thoroughly prepare the sand. In this project it was found that applying a gradient, then vibrating the 13 holes closest to the center, applying a gradient again and then vibrating all holes showed good results.

### H.1.3 CPT testing

After the vibration procedure 5 CPT tests are conducted. These tests are done both to ensure the sand is vibrated properly both also to obtain the material parameters. From the tests the soil parameters can be calculated as explained in Knudsen et al. [2013a]. The main parameter varying in the test is the relative density. The difference between this should be between all five CPTs not be greater than 0.10 and between 0.82 and 0.92. If this is not the case, another gradient and vibration procedure must be carried out.



*Figure H.4.* The piston used for CPT and installation of the bucket.

The CPT is done using a piston mounted to the top of the tank, cf. figure H.4. The piston is driven by a movable hydraulic compressor, cf. figure H.5. On the shaft of the piston a rotatable girder is mounted, making it possible to conduct CPTs everywhere in the sand volume. The first four CPTs are done in four positions at  $90^\circ$  intervals at a radial distance of approximately 40 cm from the center. The last CPT is done in the center of the tank. When conducting the CPT great care needs to be taken in order to ensure that the CPT probe penetrates the soil completely vertical. In the test the position

of the probe, i.e. the penetration depth, and the cone resistance is measured using the Spider data acquisition box and the HBM Catman software.

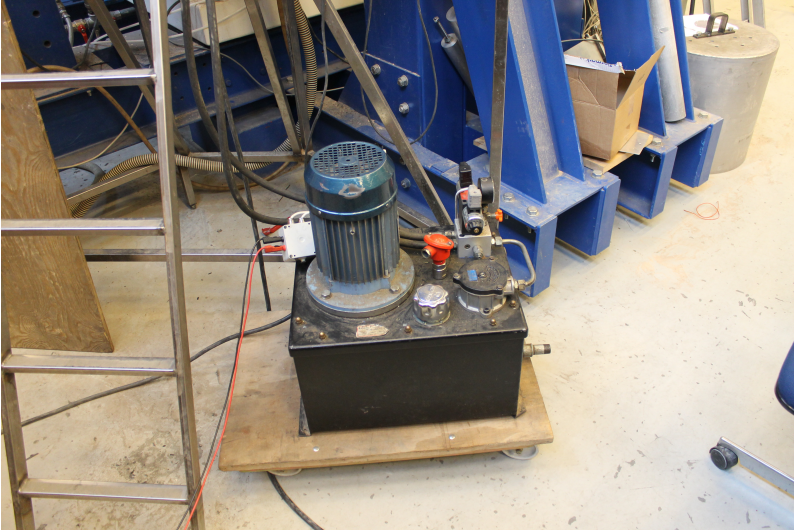


*Figure H.5.* The hydraulic compressor.

The CPT probe mounted inside the tank is seen in figure H.6



*Figure H.6.* The CPT equipment mounted and ready for test in the center of the tank.

#### H.1.4 Installation of the bucket

After the sand preparation is approved, the next step is to install the bucket and connect all the transducers to the data acquisitions boxes. Firstly the bucket is lowered onto a aluminum plate placed on top of the sand, this plate serves to distribute the weight of the bucket and ensure no penetration happens. All the cables from the pore pressure transducers are then lead through the holes off the tank, cf. figure H.7 and H.8. The cables are tightened both inside and outside the tank with an o-ring and a bolt to ensure the connections are hermetically sealed.



*Figure H.7.* The bucket placed on the aluminum plate, cables ready to be lead out of the tank.



*Figure H.8.* The holes in the tank for signal cables seen from the outside.

Once all the cables are tightened, the bucket is installed in the soil. This is done using the same piston used to do the CPTs. Firstly the bucket is lifted off the aluminum plate,

which is then removed, and then slowly step-wise installed into the sand. It is important that the direction is adjusted, to make sure the direction of the tower is aligned with the direction of attack of the actuator. The last few centimeters of the installation is crucial, as the whole bucket is below the water surface. To avoid a large overpressure in the pore water, the installation is done approximately one centimeter at the time. When the installation is done, the tower is mounted as seen in figure H.9.



*Figure H.9.* Mounting the tower on the installed bucket.

When the tower installation is complete, the four displacement transducers are mounted and connected to the Spider and the MOOG box. The bucket fully installed and instrumented is shown in figure H.10.



*Figure H.10.* The installed bucket with the displacement transducers visible.

### **H.1.5 Closing the tank and applying pressure**

The last step of the setup is to seal off the tank and apply the 200 kPa of pressure. Both hatches are attached with a rubber membrane, to ensure they are pressure proof. The pressure is applied via a buffer tank, in which the pressure can be controlled. The pressure in the tank is monitored until stable at approximately 200 kPa. The pressure is then kept overnight, before the test can be conducted.

## **H.2 Test procedure**

All the tests are conducted in the same manner, which is explained in the following enumeration.

1. The actuator is in position +100 mm from the installation procedure.
2. The actuator is moved to position +50, for the wire to be tensioned and ready to apply the forced displacement.
3. Dependent on test number, the forced displacement is applied at a certain velocity with a total displacement of 150 mm. This leaves the actuator in position -100 mm.
4. The actuator is kept in position -100 mm for 5 minutes while the pore pressures dissipate.

5. After the 5 minutes, the actuator is moved forward to position -70 mm to release the tension in the wire. The test is hereby concluded.

During the whole process all the signals are recorded with both the HBM Spider and the MOOG TCU.

# I Correction of Displacements

This section explains the calculations used to find the horizontal  $H$ , vertical  $V$  and rotational displacement  $\theta$  of the bucket from the three measured displacements  $v_1$ ,  $v_2$  and  $h_1$ .

The movement of the bucket is assumed to be divided into three independent components, namely a vertical, a horizontal and a rotational displacement. All the three displacements will have a contribution on the measurements  $v_1$ ,  $v_2$  and  $h_1$ . The contributions are divided into the components to describe the geometric influence. This will be explained in the following. In all the calculations the origin is positioned at  $O$ , which is also the reference point of the displacements. The definition of sign is such that an upwards vertical, a right-wise horizontal and a clockwise rotational displacement is positive.

## I.1 Influence with regards to rotation

The contributions to  $v_1$ ,  $v_2$  and  $h_1$  from rotation are explained using figure I.1. The corrections are all found using vector algebra and simple trigonometry.

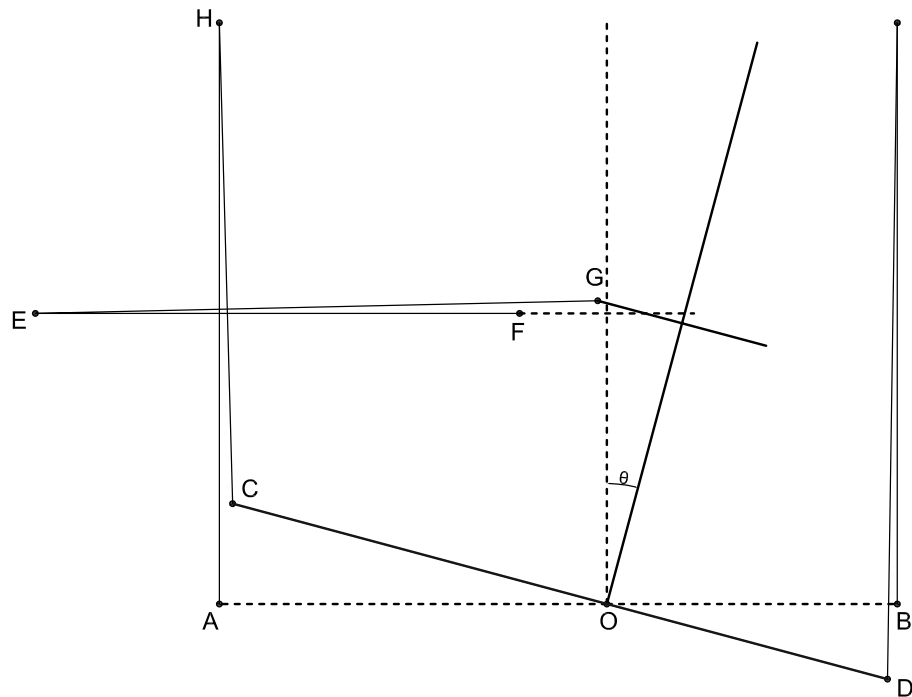


Figure I.1. Contribution from rotation only.

The front-most vertical measurement  $v_1$  in the initial state is the length of the line  $IB$ . After the rotation  $\theta$  the length increases to the length of  $ID$ . The length increment is a part of the measurement from the transducer. The coordinates of  $B$  and  $I$  are known, so the only unknown is the coordinates of  $D$ . As the length of  $OB$  is equal to  $OD$ , the position of  $D$  can be found as,

$$D_x = |OB| \cos(\theta), \quad (I.1)$$

$$D_y = -|OB| \sin(\theta). \quad (I.2)$$

The elongation  $v_{1,\theta}$  equal to  $|IB| - |ID|$  is found as,

$$v_{1,\theta} = |IB| - \sqrt{(I_x - D_x)^2 + (I_y - D_y)^2}. \quad (\text{I.3})$$

The same principle is used for  $v_2$ . The position of the new point C is found as,

$$C_x = -|OA| \cos(\theta), \quad (\text{I.4})$$

$$C_y = |OA| \sin(\theta). \quad (\text{I.5})$$

The elongation  $v_{2,\theta}$  equal to  $|HA| - |HC|$  is found as,

$$v_{2,\theta} = |HA| - \sqrt{(H_x - C_x)^2 + (H_y - C_y)^2}. \quad (\text{I.6})$$

The calculation of the horizontal contribution is a bit more complicated. The point  $F$  moves to  $G$  under the rotation  $\theta$ . The movement has a vertical and a horizontal component, which is found by inserting a coordinate system  $(x',y')$  where  $|OF|$  is coincident with the  $y'$ -axis. The system  $(x',y')$  is a rotated version of  $(x,y)$  around the origo with the angle  $\alpha$ ,

$$\alpha = \arctan\left(\frac{|F_x|}{F_y}\right). \quad (\text{I.7})$$

The absolute value is used, since the value of  $F_x$  is negative. The line  $OG$  has the same length as  $OF$ , and the coordinates in the new system can thus be calculated using the rotation of the bucket,

$$G_{x'} = |OF| \sin(\theta), \quad (\text{I.8})$$

$$G_{y'} = |OF| \cos(\theta). \quad (\text{I.9})$$

To get the coordinates in the  $(x,y)$  system a rotation formula is used,

$$G_x = \cos(\alpha) G_{x'} - \sin(\alpha) G_{y'}, \quad (\text{I.10})$$

$$G_y = \sin(\alpha) G_{x'} + \cos(\alpha) G_{y'}. \quad (\text{I.11})$$

The points  $E$ ,  $F$  and  $G$  are now known. With the coordinates found the elongation  $h_{1,\theta}$  equal to  $|EG| - |EF|$  is found as,

$$h_{1,\theta} = \sqrt{(E_x - G_x)^2 + (E_y - G_y)^2} - |EF|. \quad (\text{I.12})$$

## I.2 Influence with regards to vertical displacement

The influence is found using figure I.2.



The vertical measurements are affected by an elongation analog to the horizontal displacement in the previous case. The lengths  $|HM|$  and  $|IN|$  and the influences  $v_{1,H}$  and  $v_{2,H}$  is found as,

$$|HM| = \sqrt{|HA|^2 + H^2} \Rightarrow v_{1,H} = \sqrt{|HA|^2 + H^2} - |HA|, \quad (\text{I.14})$$

$$|IN| = \sqrt{|IB|^2 + H^2} \Rightarrow v_{2,H} = \sqrt{|IB|^2 + H^2} - |IB|. \quad (\text{I.15})$$

$$(\text{I.16})$$

## I.4 Summary of displacements

The derived expressions in the previous sections are put together to form a set of equations that can be used to find  $H$ ,  $V$  and  $\theta$ .

$$h_1 = H + h_{1,\theta} + h_{1,V} \quad (\text{I.17})$$

$$v_1 = V + v_{1,\theta} + v_{1,H} \quad (\text{I.18})$$

$$v_2 = V + v_{2,\theta} + v_{2,H} \quad (\text{I.19})$$

The system involves three unknowns, namely the displacements  $H$ ,  $V$  and  $\theta$ . All the equations are dependent on each other and are therefore solved by iteration. The procedure is,

1. Establish a starting point of the displacements  $H_0$ ,  $V_0$ , and  $\theta_0$ . Here they are set to 0.
2. Calculate updated displacements based on the initial values.
3. Evaluate the change in the values of  $H$ ,  $V$  and  $\theta$ . If change is below  $10^{-3}$ , the iteration is done, otherwise repeat point 2.

The iteration used approximately 10-15 steps for each measurement.

The assumption that the corrections can be done component wise is in fact not entirely accurate. As an example the horizontal wire transducer can be used. When a vertical displacement has taken place, the wire is no longer completely horizontal and a change in  $H$  will not directly give the same change in  $h_1$ . The problematics is assumed to give an error of approximately 1-2 %, which is deemed acceptable.

# J Additional Laboratory Results

This appendix will contain additional results compared to the ones showed in Knudsen et al. [2013a]. The results are meant to supplement the findings in the article, and will as such not be commented upon.

## J.1 All Pressure Gauges for all Tests

The results are grouped in the inside and outside pore pressure gauges, with two plots per tests.

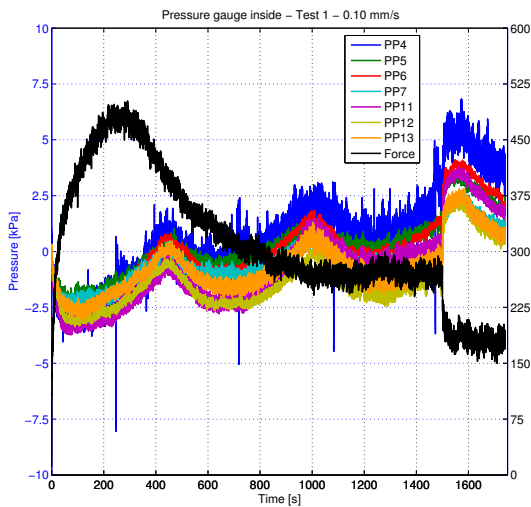


Figure J.1. Inside gauges test 1.

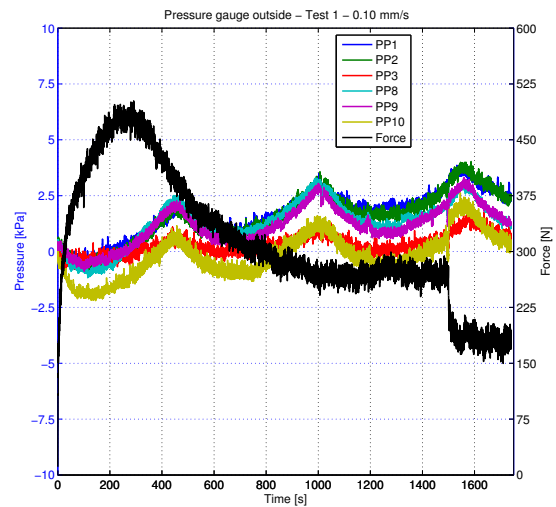


Figure J.2. Outside gauges test 1.

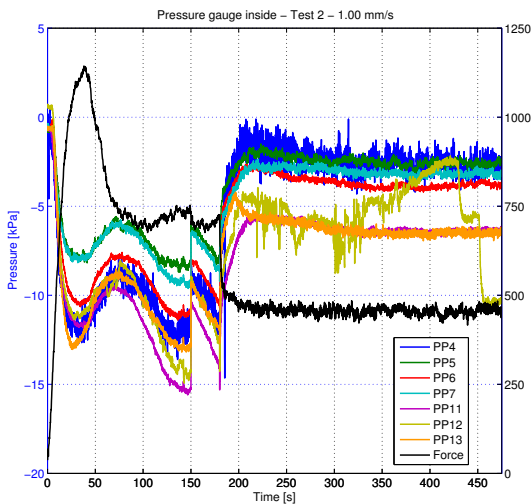


Figure J.3. Inside gauges test 2.

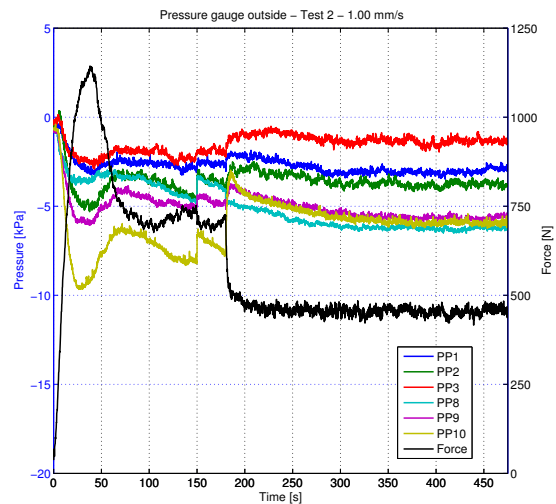


Figure J.4. Outside gauges test 2.

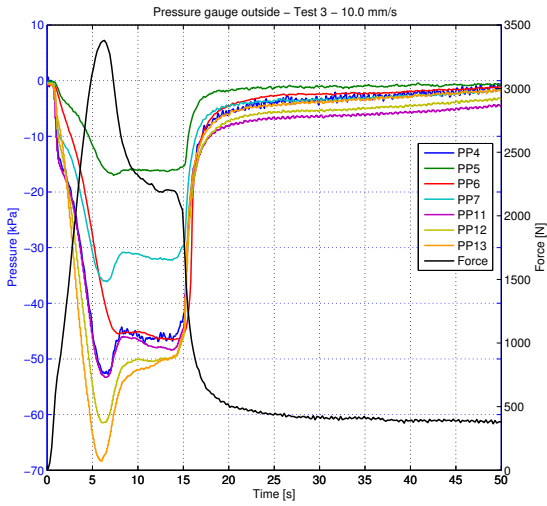


Figure J.5. Inside gauges test 3.

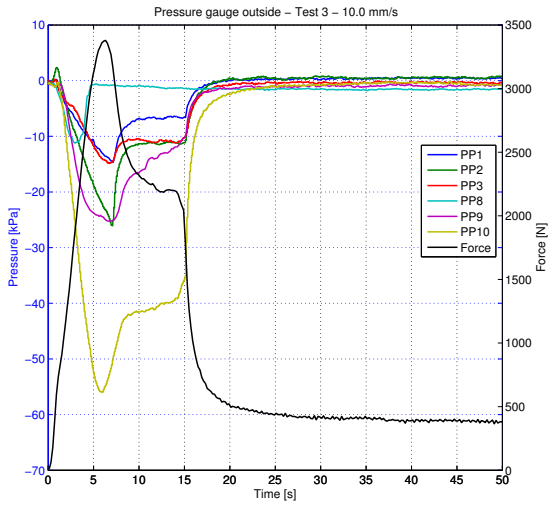


Figure J.6. Outside gauges test 3.

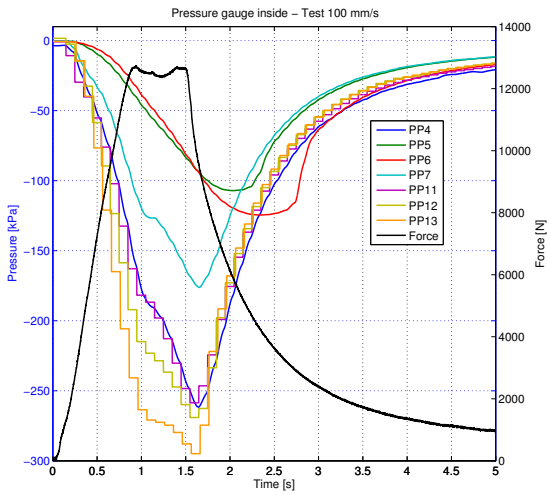


Figure J.7. Inside gauges test 4.

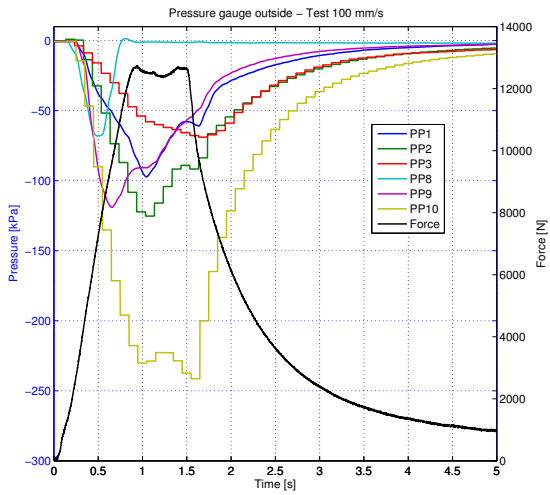


Figure J.8. Outside gauges test 4.